EXCITON POLARITON CONDENSATION IN TWO DIMENSIONAL PERIODIC LATTICE POTENTIALS

２次元周期格子ポテンシャル中のエキシトンポラリトン凝縮

BY

Kenichiro Kusudo

A DOCTORAL DISSERTATION

SUBMITTED TO THE GRADUATE SCHOOL OF
THE UNIVERSITY OF TOKYO

東京大学
THE UNIVERSITY OF TOKYO

IN PARTIAL FULFILLMENT OF THE REQUIREMENTS
FOR THE DEGREE OF
DOCTOR OF INFORMATION SCIENCE AND TECHNOLOGY

DECEMBER 2010

Committee:

Jun Adachi (Chair)
Makoto Gonokami
Kazuhiko Hirakawa
Kenjiro Taura
Toshihiko Yamasaki

Supervisor:

Yoshihisa Yamamoto

ABSTRACT

Bose-Einstein condensation (BEC) was first predicted by Bose and Einstein, and originally defined as a macroscopic occupation of bosonic particles in the ground state. After first demonstration of a nearly ideal Bose-Einstein condensate in 1995 with ultra cold atoms, a great amount of research has been done, such as Bose-Einstein condensates in two-dimensional system, and the observation of a quantised vortex.

Exciton polaritons (EPs) are quasi-particles resulting from the strong coupling between (cavity) photons and (quantum well) excitons, and have been considered as a candidate for BEC in solids. Because of their photonic component, their mass is much lighter than that of atoms or excitons, which leads to a much higher critical temperature for BEC in EP systems. The observation of BEC in EP systems has been reported by several groups. Because EPs have a short lifetime of the order of ~ps they may decay from the system before reaching the thermal equilibrium. Continuous pumping replenishes EPs in the system, and as aresult phase coherence for a time longer than their lifetime. Therefore the system has been considered to undergo dynamic condensation of EPs.

In atomic systems, another research direction that has attracted a large amount of attention in recent years is quantum simulation. The aim of quantum simulation is to give another way to investigating difficult quantum many-body problems by simulating quantum models experimentally on other quantum devices. This is advantageous because it is often easier to control the model parameters in the artificially fabricated device, rather than the original system being examined. Currently, most researchers working on quantum simulation have been working with cold atom systems and ion trap systems. To perform the quantum simulation, how to implement the desired model is an important question. In cold atom systems, optical lattices provide a suitable way to create periodic lattice potentials. On the other hand, in EP systems, several ways to create potentials have been suggested and demonstrated. Currently weak one dimensional lattice potentials have been demonstrated experimentally.

In this thesis, we implemented several two dimensional lattice potentials in EP systems. The dynamic nature of EPs gives us rich physics, especially due to metastable condensation. The EP systems have the advantage over atomic system in that it is easier for excited state condensations to be formed.

The periodic lattice potentials are implemented by depositing patterned thin metals. The metal changes the boundary condition of photons and make the cavity resonance higher in energy, which leads to the potential barriers for EPs of the order of $\sim 200\mu eV$. In two dimensional square lattice potentials, we have observed d-orbital wave con-

densates at M-points. The order parameter of this meta-stable condensation has 2D atomic *d*-orbital symmetry, and two-fold rotational symmetry against the trap center. We detect this *d*-orbital wave through the momentum space distribution, and the real field distribution. In two dimensional triangular lattice potentials, we observed several results indicating the formation of vortex-antivortex lattices, which originates from the single particle wave function of the meta-stable state at M-points.

Acknowledgements

First of all, I would like to express my sincere gratitude and appreciation to my supervisor, Prof. Yoshihisa Yamamoto, not only for his expert guidance and mentorship, but also for his encouragement and support at all levels. His brilliant insight, experiences, courage, uninterrupted interest in physics, earnest mentorship, patience...always encourages and motivates me. He is always an example of a great scientist and a great educator. Without him, I would never have been able to complete this dissertation.

I would like to thank my oral defense committee: Professor Jun Adachi, Makoto Gonokami, Kazuhiko Hirakawa, Kenjiro Taura, and Toshihiko Yamasaki. I thank them for their time and interest, and for the interesting and important questions they asked.

I would like to thank Professor Toshimasa Fujisawa from Tokyo Institute of Technology, who was a division head of NTT Basic Research Laboratory, NTT cooperation,. He kindly gave me the oppotunity of learning the device fabrication in a world leading company of basic research, with the cooperation of distinguished researchers in an environment of excellent facilities.

I am grateful to Dr. Na Young Kim, research associate in Sanford Yamamoto group. She has been not only a collaborator but also a good mentor for me. Her kindness always helps me and her sincerity to science motivates me a lot. She instructed me in optics and her careful advice regarding my research were a significant help to me, and I would like to thank her.

I wish to express my deepest gratitude to my mentors in NII Yamamoto group, Dr. Tim Byrnes ,Dr. Michael Fraser and Dr. Shoko Utsunomiya. Tim Byrnes gave me deep physical insights from a theoretical point of view. Michael Fraser gave me many advices and comments on my research and instructed me in optics. Shoko Utsunomiya also gave me many advices and comments on my research. They also made my lab life rich as good mentors, good colleagues and good friends, and I would like to thank them.

I would like to thank our collaborator Dr. Norio Kumada from NTT Basic Research Laboratory, NTT cooperation. He always takes care of our group members and helps and teaches techniques used in the lab.

I would like to thank Mineo Ueki from NTT AT. He grew our photomask despite our request. His suggestions and instructions in the clean room were most helpful and important.

I would like to thank Dr. Satoshi Sasaki from NTT who trained me in electron-beam lithography and gave me useful discussion of device fabrication. I would like to thank all the other members of Quantum Solid State Physics Research group.

I would like to thank other members of Yamamoto group: Naoyuki Masumoto, Natsuko Ishida, Kai Yan, Nobuyuki Takahashi, Kenta Takata and Tomoya Matsukawa in Japan, Qiang Zhang, Tomoyuki Horikiri, Kaoru Sanaka in Stanford. Tomoyuki Horikiri especially gave me a lot of his great knowledge with optics and helped me with my Stanford life. I would like to thank the secretaries of our group: Yukiko Sato, Yoko Shioda, Yurika Peterman and Rieko Sasaki. I would like to thank our collaborators who generously provided the samples for this thesis: A. Loeffler, S. Hoefling and.A. Forchel from Wuerzburg university.

I would like to thank my friends who are also working as students in their Ph.D years, Hisashi Kurasawa, Takahiro Matsuda, Akihisa Miyazoe and Yutaka Shikano. They motivated me a lot through discussion, conversation, and friendship.

Last but not least, I would like to thank my amazing family, parents, brother and grandmothers, for their constant support and encouragement.

December 2010

Contents

List of Figures

List of Tables

Chapter 1

Introduction

Bose-Einstein condensation was first predicted by Bose [2] and Einstein [3], and originally defined as a macroscopic occupation of bosonic particles in the ground state. Though superfluidity of He^4 is now considered to be related to BEC, the first demonstration of a nearly ideal BEC was reported in 1995. Wieman and Cornell's group demonstrated a BEC of a Rb^{87} gas [4], and a few months later Ketterle's group achieved the same with sodium atoms [5]. After observation of BEC in ultra cold atoms, much further research has been done, such as BEC in two-dimensional systems, and the observation of a quantised vortex [6].

Exciton polaritons (EPs) are quasi-particles resulting from the strong coupling between (cavity) photons and (quantum well) excitons [7], and have been considered as a candidate for BEC in solids [8]. Because of the photonic component, their mass is much lighter than that of atoms or excitons, which leads to a much higher critical temperature for BEC in EP systems. The observation of BEC in EP systems has been reported by several groups [9] [10] [11] [12]. Because EPs have short lifetime (~ps), they may decay from the system before reaching thermal equilibrium. Although the continuous pump replenishes EPs in the system, they keep phase coherence for a time longer than their lifetime. Therefore they have been considered to form a dynamical condensate of EPs (though there are a few papers reporting thermal equilibrium [13]). In other systems, there are also reports of BEC, such as a BEC of magnons [14] [15] and photons [16].

In atomic systems, another research direction that has attracted a large amount of attention in recent years, is quantum simulation [17]. The aim of quantum simulation

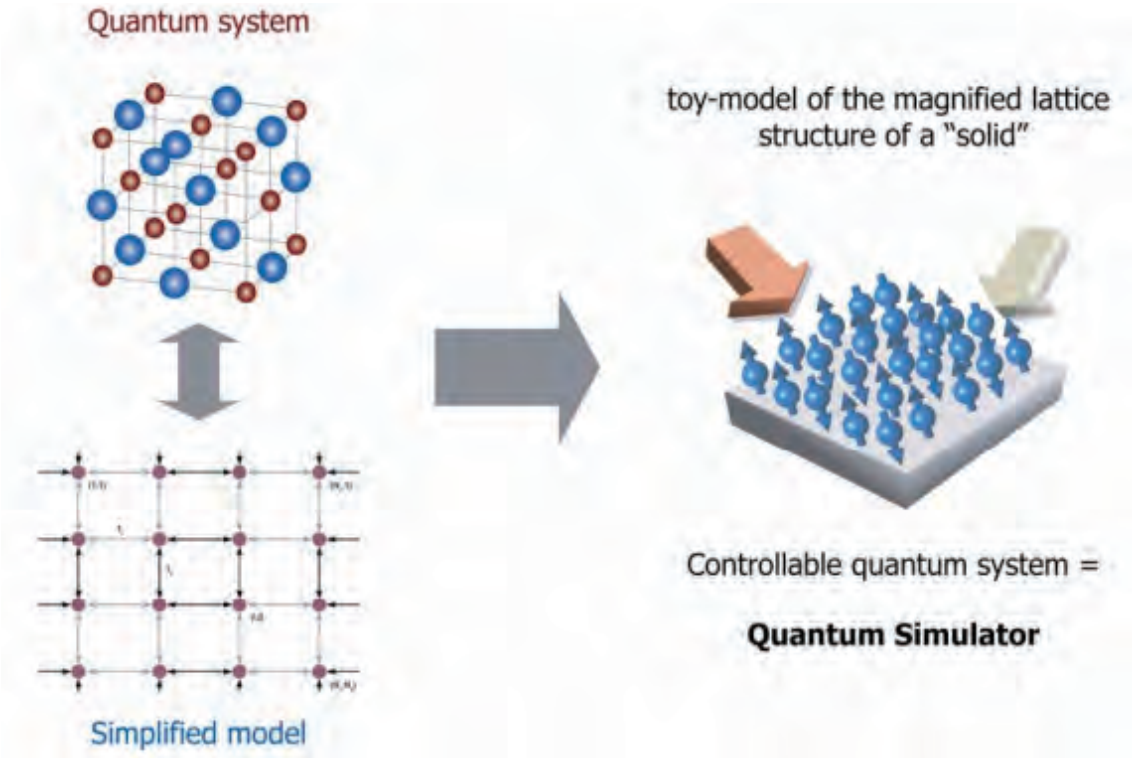

Figure 1.1: A schematic of quantum simulator from [1].

is to give another way to investigating difficult quantum many-body problems by simulating quantum models experimentally on other quantum devices (fig. 1.1) [18]. This is advantageous because it is often easier to control the model parameters in the artificially fabricated device, rather than the original system being examined.

The Hubbard model is one of the most famous models which describe strongly correlated many-body systems. The Hubbard model has taken a great amount of interests, not only because this model describes the quantum phase transition due to the many-body interaction [19] [20] but also because it has been suggested that this model explained the mechanism of the high-T_c superconductivity [21].

The Hubbard model is defined with interacting particles in lattice sites under two assumptions. One is that particles can tunnel only to nearest neighbor sites. The other is that particles interact only with themselves in the same site. Therefore the Hamiltonian

of the Hubbard models for Bose and Fermi particles have the form respectively:

$$H_{Bose} = -t \sum_{<i,j>} \hat{a}_i^\dagger \hat{a}_j + \frac{1}{2} U \sum_i \hat{n}_i(\hat{n}_i - 1) \tag{1.1}$$

$$H_{Fermi} = -t \sum_{<i,j>} \hat{c}_{i\sigma}^\dagger \hat{c}_{j\sigma} + \frac{1}{2} U \sum_i \left(\hat{n}_{i\uparrow} - \frac{1}{2}\right)\left(\hat{n}_{i\downarrow} - \frac{1}{2}\right). \tag{1.2}$$

$\hat{a}(\hat{c})$ is the annihilation operator, and $\hat{a}^\dagger(\hat{c}^\dagger)$ is the creation operator for Bose (Fermi) particles. $\hat{n}_i = \hat{a}_i^\dagger \hat{a}(\hat{c}_i^\dagger \hat{c})$ is the number operator. t denotes the hopping matrix element between nearest neighbor sites, and U denotes the strength of the interaction. Here we ignore the chemical potential terms. Assuming a zero temperature, when $U/t \ll 1$ the system described by the Bose (Fermi) Hubbard model undergoes to superfluid (metal) states. In this case, the hopping terms (the first terms in eq. 1.2) dominates in the Hamiltonian. Therefore, in order to minimize the hopping energy, particles stay in the states whose wavefunctions spread over the whole system. This results that particles can freely move over the whole system. On the other hand, when $U/t \gg 1$, the interaction term dominates the system. Considering repulsive interaction, particles try to avoid overlapping with each other. Therefore the tunneling to nearest neighbor sites is suppressed if there are particles in the nearest neighbor sites, and the system behaves as a insulators. These insulator states due to the repulsive interaction are called as Mott insulators. Between these two extreme regions, there is the second order quantum phase transition [22]. The Hubbard models are many-body problems, so that they are difficult to solve analytically and numerical.

The quantum simulation for the Bose-Hubbard model was first demonstrated in 2002 with ^{87}Rb atoms [23]. They first prepared a BEC of ^{87}Rb atoms, and adiabatically introduced optical lattices to implement the lattice structure. By changing the intensity of the lasers which create optical lattices, the depth of the lattice potentials can be controlled. Because U/t increases with the amplitude of the potential, they can sweep U/t from a superfluid regime to a Mott insulator regime. They observed the phase transition through the lost of coherent interference patterns in momentum space. In the superfluid regime, the system has phase coherence over many sites because particles can move around. In contrast, in the Mott insulator regime, phase coherence is lost because particles are localized. The value of U/t where the phase transition occurs, experimentally measured, was consistent with the theoretical estimation.

Quantum simulation of many-body physics gives us not only deep insights of physics, but also a possibility for applications of many-body phenomena. Recently the

phase transition from metal to Mott insulator described by the Fermi-Hubbard models (which, we note again, has been suggested to explain the physics underlying the high-T_c superconductivity.) has been demonstrated [24] [25]. Quantum simulation for many-body physics with cold atoms has been growing more and more. We also note that using Josephson junction (JJ) arrays of superconducting materials the Hubbard model physics has been also explored [26].

In 2009, a different kind of quantum simulation was demonstrated using ions. That is quantum simulation of Dirac equation [27] which is one particle equations for relativistic fermi particles. This quantum simulation is a kind of demonstration of difficult phenomena to experimentally detect. Using $^{40}Ca^{\dagger}$, they implement Dirac equations and observed "Zitterbewegung", which originates from the interference between spinors. They also demonstrated "quantum walk" which is the quantum version of random walk problems [28]. This type of quantum simulation will give us a chance to observe new phenomena which rarely exist in the nature.

As is seen above, quantum simulation in several systems has taken great success, we review the characteristics of each system. A cold atom system is the most major system for quantum simulation, because this system is quite pure and highly controllable. Up to now experiments have basically treated the ground state of the system in equilibrium. Ion systems, where we can control ions in one particle level, are also pure systems. But there is a difficulty to do with many particles. Regarding JJ arrays of superconductors, the biggest problem is the impurity potentials which can destroy the implemented model in the system.

EP systems are more directly linked to the application than atoms and ions, due to the technology for semiconductors. And they are more robust against impurities than superconductors, due to EP's very light mass. Most attractively, EP systems are dynamical and in non-equilibrium. In this thesis, we explore new physics due to such EP' s characteristics in two-dimensional lattice potentials. Especially we focus on the property, such as an orbital order, of meta-stable condensation in excited band states.

The outline of this thesis is as follows. In chapter 2, we introduce exciton-polaritons, and we review Bose-Einstein condensation in chapter 3. Chapter 4 shows the set up for experiments. In chapter 5, the observation of *d*-orbital superfluids in square lattice potentials is described. In chapter 6, we show the formation of vortex-antivortex lattice structure in triangular lattice potentials. Chapter 7 is for the meta-stable condensation in honey-comb lattice potentials. And we conclude this thesis in chapter 8.

Chapter 2

Exciton-Polaritons

Exciton-polaritons (EPs) are quasi-particles resulting from the strong coupling between quantum well (QW) excitons and cavity photons. In this chapter, the basic concept of EPs is introduced.

2.1 Excitons

If an energy is applied to a low temperature semiconductors via a photonic excitation, an electron is excited into the conduction band leaving a hole in the valence band. Because of the attractive Coulomb interaction between electrons and holes, they form a bound state known as an exciton. Such pair states are the energetically lowest excitation in weakly excited semiconductors. Excitons whose wave functions spread over many unit cells are called Wannier excitons, usually seen in semiconductors with a small electron or hole effective mass and a large dielectric constant. They have a large dipole moment so that they strongly couple to the photon field. Here we discuss the exciton, especially the Wannier exciton.

2.1.1 Exciton as bosons

Following [29] we review excitons as excitations in semiconductor systems and as bosonic quasi-particles. We consider a simple model of a direct two-band semiconductor with isotropic effective mass with spinless electrons. We start with the following

Hamiltonian

$$H = \int d^3\mathbf{x}\, \hat{\psi}^\dagger(\mathbf{x})\, \hat{H}_0(\mathbf{x})\, \hat{\psi}(\mathbf{x}) \; + \frac{1}{2} \int d^3\mathbf{x}\, d^3\mathbf{y}\, \hat{\psi}^\dagger(\mathbf{x})\, \hat{\psi}^\dagger(\mathbf{y})\, \hat{V}(\mathbf{x}-\mathbf{y})\, \hat{\psi}(\mathbf{y})\, \hat{\psi}(\mathbf{x})\,, \tag{2.1}$$

where $\hat{H}_0(\mathbf{x}) = -\frac{\hbar^2}{2m}\nabla^2 + U(\mathbf{x})$ is the single electron Hamiltonian which includes the kinetic energy $-\frac{\hbar^2}{2m}\nabla^2$ and the crystal potentials $U(\mathbf{x})$ and $\hat{V}(\mathbf{x}-\mathbf{y}) = \frac{e^2}{\epsilon|\mathbf{x}-\mathbf{y}|}$ is the two-body Coulomb interaction (We use c.g.s. throughout). e is the elementary charge of electrons, ϵ is the dielectric constant of the semiconductor and $\hbar$ is the reduced Planck constant. Using the eigenfunctions of $\hat{H}_0$, we rewrite the Fermi-field operator as

$$\hat{\psi}(\mathbf{x}) = \sum_{j=c,v} a_{\mathbf{k}j}\, \hat{\psi}_{\mathbf{k}j}(\mathbf{x}). \tag{2.2}$$

$\psi_{\mathbf{k}j}(\mathbf{x}) = u_{\mathbf{k}j}(\mathbf{x}) \exp(i\mathbf{k}\mathbf{x})/\sqrt{N}$ are the Bloch eigenfunctions of $\hat{H}_0$ for an electron with a wave vector $\mathbf{k}$ in the band j due to the crystal lattice. c and v denote a conduction band and a valence band respectively. $\hat{a}_{\mathbf{k}j}$ and $\hat{a}^\dagger_{\mathbf{k}j}$ are the Fermi annihilation and creation operators, which obey the commutation relations $\left[\hat{a}_{\mathbf{k}i}, \hat{a}_{\mathbf{l}j}\right] = 0$ and $\left[\hat{a}_{\mathbf{k}i}, \hat{a}^\dagger_{\mathbf{l}j}\right] = \delta_{\mathbf{k},\mathbf{l}}\delta_{i,j}$. Inserting (2.2) into (2.1), we get

$$\begin{aligned}
H \;=\; & \sum_{\mathbf{k}} E^0_j(k)\hat{a}^\dagger_{\mathbf{k}j}\hat{a}_{\mathbf{k}j} \;+\; \frac{1}{2}\sum_{\mathbf{k}} V(c,c,c,c,\mathbf{k_1},\mathbf{k_2},\mathbf{k_3},\mathbf{k_4})\hat{a}^\dagger_{\mathbf{k}_1c}\hat{a}^\dagger_{\mathbf{k}_2c}\hat{a}_{\mathbf{k}_3c}\hat{a}_{\mathbf{k}_4c} \\
+ \; & \frac{1}{2}\sum_{\mathbf{k}} V(v,v,v,v,\mathbf{k_1},\mathbf{k_2},\mathbf{k_3},\mathbf{k_4})\hat{a}^\dagger_{\mathbf{k}_1v}\hat{a}^\dagger_{\mathbf{k}_2v}\hat{a}_{\mathbf{k}_3v}\hat{a}_{\mathbf{k}_4v} \\
+ \; & \sum_{\mathbf{k}} V(c,v,v,c,\mathbf{k_1},\mathbf{k_2},\mathbf{k_3},\mathbf{k_4})\hat{a}^\dagger_{\mathbf{k}_1c}\hat{a}^\dagger_{\mathbf{k}_2v}\hat{a}_{\mathbf{k}_3v}\hat{a}_{\mathbf{k}_4c} \\
+ \; & \sum_{\mathbf{k}} V(c,v,c,v,\mathbf{k_1},\mathbf{k_2},\mathbf{k_3},\mathbf{k_4})\hat{a}^\dagger_{\mathbf{k}_1c}\hat{a}^\dagger_{\mathbf{k}_2v}\hat{a}_{\mathbf{k}_3c}\hat{a}_{\mathbf{k}_4v},
\end{aligned} \tag{2.3}$$

where $V(i,j,l,m,\mathbf{k_1},\mathbf{k_2},\mathbf{k_3},\mathbf{k_4}) = \langle \mathbf{k_1}i, \mathbf{k_2}j|\hat{V}|\mathbf{k_3}l, \mathbf{k_4}m\rangle$. In (2.3), we neglect terms which do not conserve the number of total excitations such as $\hat{a}^\dagger_{\mathbf{k}_1c}\hat{a}^\dagger_{\mathbf{k}_2c}\hat{a}_{\mathbf{k}_3c}\hat{a}_{\mathbf{k}_4v}$. Here we introduce the concept of a hole in the valence band. When we excite one electron from the valence band to the conduction band, we say one electron is annihilated in the valence band and one is created in the conduction band. Instead of saying one electron is annihilated in a valence band, we consider the creation of a hole which compensates for the conservation rule. Namely, a hole should have observables such as the energy and the momentum and the charge whose absolute value is same as the annihilated electron but sign is opposite. Formally the annihilation operator of a hole

can be introduced by a time reversal transformation $\mathbf{K}$,

$$\hat{a}_{\mathbf{k}v} = \mathbf{K}^{\dagger}\hat{b}_{\mathbf{k}}\mathbf{K} = \hat{b}^{\dagger}_{-\mathbf{k}}. \tag{2.4}$$

Therefore, in the following, we drop the index of "c" on the conduction band operator : $\hat{a}_{\mathbf{k}c} = \hat{a}_{\mathbf{k}}$. Then our Hamiltonian is now in the following form,

$$\begin{aligned} H &= \sum E_e(k)\hat{a}^{\dagger}_{\mathbf{k}}\hat{a}_{\mathbf{k}} + \sum E_h(k)\hat{b}^{\dagger}_{\mathbf{k}}\hat{b}_{\mathbf{k}} \\ &+ \frac{1}{2}\sum V(c,c,c,c,\mathbf{k_1},\mathbf{k_2},\mathbf{k_3},\mathbf{k_4})\hat{a}^{\dagger}_{\mathbf{k_1}}\hat{a}^{\dagger}_{\mathbf{k_2}}\hat{a}_{\mathbf{k_3}}\hat{a}_{\mathbf{k_4}} \\ &+ \frac{1}{2}\sum V(v,v,v,v,-\mathbf{k_1},-\mathbf{k_2},-\mathbf{k_3},-\mathbf{k_4})\hat{b}^{\dagger}_{\mathbf{k_1}}\hat{b}^{\dagger}_{\mathbf{k_2}}\hat{b}_{\mathbf{k_3}}\hat{b}_{\mathbf{k_4}} \\ &- \sum \left(V(c,v,v,c,\mathbf{k_1},\mathbf{k_3},\mathbf{k_2},\mathbf{k_4}) - V(c,v,c,v,\mathbf{k_1},\mathbf{k_3},\mathbf{k_4},\mathbf{k_2})\right)\hat{a}^{\dagger}_{\mathbf{k_1}}\hat{b}^{\dagger}_{\mathbf{k_2}}\hat{b}_{\mathbf{k_3}}\hat{a}_{\mathbf{k_4}}. \end{aligned} \tag{2.5}$$

We here ignore the constant term. With the effective mass approximation,

$$E_e(k) = E_g + \frac{\hbar^2 k^2}{2m_e} \tag{2.6}$$

$$E_h(k) = \frac{\hbar^2 k^2}{2m_h}, \tag{2.7}$$

where m_e and m_h are the effective electron and hole mass and E_g is the band gap.

Here we consider the wave function of the most general electron-hole state,

$$|\mathrm{p}\rangle = \sum C_{\mathbf{kk'}}\hat{a}^{\dagger}_{\mathbf{k}}\hat{b}^{\dagger}_{\mathbf{k'}}|0\rangle \tag{2.8}$$

where $|0\rangle$ is the crystal ground state. We get the following equation for the amplitude $C_{\mathbf{kk'}}$,

$$\begin{aligned} [E_e(k) &+ E_h(k') - E]C_{\mathbf{kk'}} \\ &- \sum_{\mathbf{l},\mathbf{l'}} \left[V(c,v,v,c,\mathbf{k},-\mathbf{l'},-\mathbf{k'},\mathbf{l}) - V(c,v,c,v,\mathbf{k},-\mathbf{l'},\mathbf{l},-\mathbf{k'})\right] C_{\mathbf{ll'}} = 0. \end{aligned} \tag{2.9}$$

For Wannier excitons, where the momenta of the relative motion is small and the separation between the electron and the hole is large compared to the lattice period, we can treat the plane wave factor and the Coulomb potential as slowly varying functions, which change little in one unit cell. We notice that integrating the volume of one unit cell v_0

$$\int_{v_0} d^3\mathbf{x}\, u^*_{\mathbf{k}\simeq 0,c}(\mathbf{x})u_{\mathbf{k}\simeq 0,c}(\mathbf{x}) \simeq 1\ , \quad \int_{v_0} d^3\mathbf{x}\, u^*_{\mathbf{k}\simeq 0,v}(\mathbf{x})u_{\mathbf{k}\simeq 0,v}(\mathbf{x}) \simeq 1$$

$$\int_{v_0} d^3\mathbf{x}\, u^*_{\mathbf{k}\simeq 0,c}(\mathbf{x})u_{\mathbf{k}\simeq 0,v}(\mathbf{x}) \simeq 0 \tag{2.10}$$

Then the exchange integral $V(c,v,c,v,\mathbf{k},-\mathbf{l}',\mathbf{l},-\mathbf{k}')$ in (2.9) vanishes and the direct Coulomb term has the form

$$V(c,v,v,c,\mathbf{k},-\mathbf{l}',-\mathbf{k}',\mathbf{l}) = \frac{1}{V^2}\int d^3\mathbf{x}d^3\mathbf{y}\exp\left[i(\mathbf{l}-\mathbf{k})\cdot\mathbf{x}+i(\mathbf{l}'-\mathbf{k}')\cdot\mathbf{y}\right]\frac{e^2}{\epsilon\mid\mathbf{x}-\mathbf{y}\mid}, \quad (2.11)$$

where the volume of the system is V. We finally have the Wannier equation for an exciton

$$\left[-\frac{\hbar^2}{2m_e}\nabla_e^2-\frac{\hbar^2}{2m_h}\nabla_h^2+E_g-\frac{e^2}{\epsilon\mid\mathbf{x}-\mathbf{y}\mid}\right]\phi(\mathbf{x_e},\mathbf{x_h}) \;=\; E\phi(\mathbf{x_e},\mathbf{x_h}) \quad (2.12)$$

where

$$\phi(\mathbf{x_e},\mathbf{x_h}) = \sum C_{\mathbf{kk}'}\exp\left[i\mathbf{k}\cdot\mathbf{x_e}+i\mathbf{k}'\cdot\mathbf{x_h}\right] \quad (2.13)$$

By introducing the relative coordinate $\mathbf{r}$ and the center of mass coordinate $\mathbf{R}$

$$\mathbf{r} = \mathbf{x_e}-\mathbf{x_h}\ ,\ \ \mathbf{R} = \beta\mathbf{x_e}+\alpha\mathbf{x_h} \quad (2.14)$$

with $\alpha = m_h/M$ and $\beta = m_e/M$ and $M = m_e + M_h$, the center of mass motion can be separated

$$\phi(\mathbf{x_e},\mathbf{x_h}) = \varphi(\mathbf{r})\exp(i\mathbf{K}\cdot\mathbf{R})/\sqrt{V} \quad (2.15)$$

The resulting equation of the relative motion is

$$\left(-\frac{\hbar^2}{2m_r}\nabla_r^2-\frac{e^2}{\epsilon r}+E_n\right)\varphi_n(\mathbf{r}) = 0, \quad (2.16)$$

where $m_r = \frac{m_e m_h}{M}$. The ground state solution of (2.16) has a binding energy

$$E_b = \frac{e^2}{2\epsilon a_0} \quad (2.17)$$

and the Bohr radius

$$a_0 = \frac{\hbar^2\epsilon}{e^2 m_r}. \quad (2.18)$$

Now we can introduce the exciton operator

$$\hat{C}^\dagger_{\mathbf{K}n} = \sum_{\mathbf{k},\mathbf{k}'}\delta_{\mathbf{K},\mathbf{k}+\mathbf{k}'}\varphi_n(\mathbf{l})\hat{a}^\dagger_{\mathbf{k}}\hat{b}^\dagger_{\mathbf{k}'}, \quad (2.19)$$

with $\mathbf{l} = \alpha\mathbf{k} - \beta\mathbf{k}'$ and $\varphi_n(\mathbf{l})$ is the Fourier transform of $\varphi_n(\mathbf{x})$. After some algebra we get the commutation relation of exciton operators,

$$[\hat{C}_{\mathbf{K}n}, \hat{C}_{\mathbf{K}'n'}] = 0\,, \quad [\hat{C}^{\dagger}_{\mathbf{K}n}, \hat{C}^{\dagger}_{\mathbf{K}'n'}] = 0 \tag{2.20}$$

and

$$[\hat{C}_{\mathbf{K}n}, \hat{C}^{\dagger}_{\mathbf{K}'n'}] = \delta_{\mathbf{K},\mathbf{K}'}\delta_{n,n'} + O(na_0^3). \tag{2.21}$$

Eq. (2.21) says that excitons can be described as bosonic quasi-particles when the mean distance between the excitons is much larger than their Bohr radius.

2.1.2 Quantum well excitons

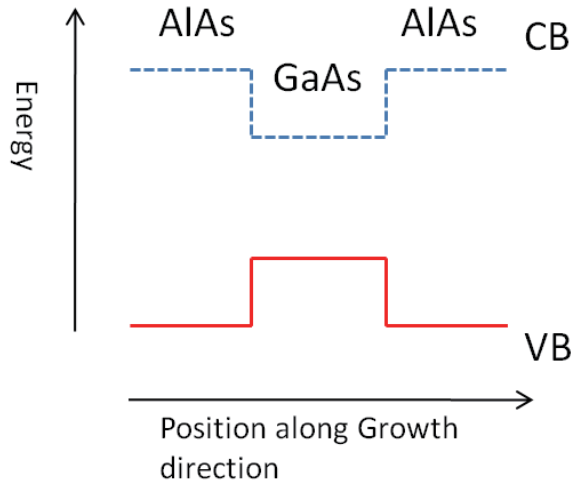

Figure 2.1: A typical energy structure of a quantum well along the growth axis. Dotted lines indicate the bottom of the conduction band, the solid lines indicate the top of the valence band. GaAs, having the smaller band gap, is sandwiched by AlAs, which has the bigger band gap.

In the previous section, we have introduced the concept of an excitons in a three dimensional system. We now consider excitons in quantum wells, namely in a quasi two dimensional system. An example of a quantum well structure is shown in fig. 2.1. Both electrons and holes are confined in the GaAs layer, resulting in excitons also

being confined there. Therefore the translational symmetry along z-axis (the growth axis) is broken, and the freedom along z-axis is frozen, giving a quasi two-dimensional system. The difference of the dimensionality first appears for the one-particle state for an electron in a conduction and valence band, which in two dimensions is given by,

$$\psi_{\mathbf{k}_{\parallel},j,n_j} = \frac{1}{\sqrt{S}} \exp\left(i\mathbf{k}_{\parallel} \cdot \rho\right) c_{j,n_j}(z) u_j(\rho, z), \tag{2.22}$$

where S represents the normalization surface. $c_{j,n_j}(z)$ denotes the wave function along the z-axis due to the QW confinement, while $u_j(\rho, z)$ denotes the Bloch wave function due to the crystal lattice. Here $\mathbf{k}_{\parallel}$ is the two dimensional wave vector of the exciton center-of-mass motion along the plane of the structure. ρ is the two dimensional relative coordinate in the quantum well plane and z is the coordinate along the growth direction. New indices n_j appear in eq.(2.22) and label the quantum well subbands which originate from the confinement of electrons and holes along the growth direction. The degree of freedom in the growth direction can be integrated independently to the other two. Then the resulting two dimensional Schrödinger equation of the relative motion of a electron-hole pair is

$$\left(-\frac{\hbar^2}{2m_r}\nabla_{\rho}^2 - \tilde{U}(\rho) + E_n\right)\varphi_n(\rho) = 0. \tag{2.23}$$

$\tilde{U}(\rho)$ is the effective Coulomb interaction integrated in the growth axis, and has a form of

$$\tilde{U}(\rho) = \int dz_1 dz_2 \frac{e^2}{\epsilon \mid \mathbf{r_1} - \mathbf{r_2} \mid} \mid c_c(z_1) \mid^2 \mid c_v(z_2) \mid^2. \tag{2.24}$$

In the strong confinement limit, we can replace the$\mid c_c(z_1) \mid^2$ and $\mid^2 \mid c_v(z_2) \mid^2$ by the delta function. Then we get the form of the effective Coulomb interaction as

$$\tilde{U}(\rho) = \frac{e^2}{\epsilon \mid \rho \mid}. \tag{2.25}$$

In this case, for the lowest energy bound state, we get a binding energy four times larger than 3D case, and a Bohr radius two times larger.

2.2 Microcavity

We have said about that EPs are quasi-particles resulting from the strong coupling between quantum well excitons and cavity photons, resulting from placing the

quantum well inside a microcavity. Here we give an overview of semiconducter microcavities.

2.2.1 A Fabry-Pérot cavity

We first explain what a 'cavity' is, which confines typical light modes. Fig. (2.2)

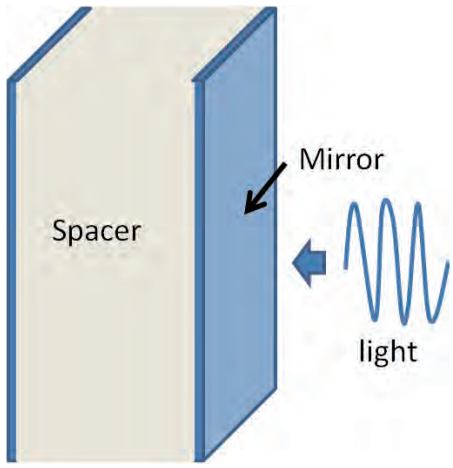

Figure 2.2: A schematic picture of a Fabry-Pérot cavity. A spacer is sandwiched by two mirrors.

shows a simple cavity, called a Fabry-Pérot cavity. If the reflectivity of the mirrors are 1, only lights which constructively interfere with each other can exist inside the cavity. So it is required that the phase change in a round trip inside the Fabry-Pérot cavity equals N times 2π (N is a integer):

$$k_z^{cav} L_c = N \cdot \pi, \tag{2.26}$$

where k_z^{cav} is the wave number of the light inside the cavity, and L_c is the cavity length. While the wave number inside k^{cav} and outside k^0 has the relation $\mid \mathbf{k}^{cav} \mid = n \mid \mathbf{k}^0 \mid$, the wave number components along the cavity plane can take any value since no mirrors are present (n is the reflective index of the material inside.) So we have

$$k_z^{cav} = \sqrt{k^{cav2} - k_{\parallel}^2} = \left(\frac{\omega^2 n^2}{c^2} - k_{\parallel}^2 \right)^{\frac{1}{2}} \tag{2.27}$$

and then eq. (2.26) becomes

$$\left(\frac{\omega^2 n^2}{c^2} - k_{\|}^2\right)^{\frac{1}{2}} L_c = N \cdot \pi \tag{2.28}$$

where ω is the angular frequency of light, and c is the speed of light in a vacuum. Those relation means that a Fabry-Pérot cavity quantises k_z inside the cavity, while $k_{\|}$ is still free.

We consider a more general case, a Fabry-Pérot cavity with mirrors having a complex reflectivity $R = r(w)e^{i\phi_r}$. Consider a propagating plane wave : $E_0(w,z) = E_0 \exp(ik_z z)$ coming from outside the cavity. Inside the cavity, the electric field can be written in the form as,

$$E(w,z) = E_0 \left(A(w)\exp(ik_z z) + B(w)\exp(-ik_z z)\right). \tag{2.29}$$

Considering the boundary conditions at two mirrors, we get

$$A(w) = E_0 \frac{\sqrt{1 - r(w)^2}}{1 - r(w)^2 \exp(2ik_z L_c + 2\phi_r)} \tag{2.30}$$

and

$$B(w) = E_0 \frac{r(w)\exp(2ik_z L_c + \phi_r)\sqrt{1 - r(w)^2}}{1 - r^2 \exp(2ik_z L_c + 2\phi_r)} \tag{2.31}$$

The field strength at the center of the cavity is obtained by taking the square modulus of the electric field :

$$E(w) = |\, A(w)\exp(\frac{ik_z L}{2}) + B(w)\exp(\frac{-ik_z L}{2})\,|^2 \tag{2.32}$$

$$= E_0^2 \frac{1 - r(w)^2}{(1 - r(w))^2 + 4r(w)\sin^2\left(\frac{k_z L_c + \phi_r}{2}\right)} \tag{2.33}$$

For the simplest case, $\phi_r = 0$ and $r(w) = r$, then

$$E(w) = E_0^2 \frac{1 - r^2}{(1 - r)^2 + 4r\sin^2\left(\frac{k_z L_c}{2}\right)} \tag{2.34}$$

Near the resonance condition, eq.(2.34) can be written as

$$E(w) \propto \frac{1}{(w - w_c)^2 + \gamma_c}, \tag{2.35}$$

where $w_c = \frac{\pi c}{n_{cav} L_c}$ is the resonant wave length and $\gamma_c = \frac{1-r}{2r}\frac{c}{n_{cav} L_c}$ describes the line-width of the cavity. n_{cav} is the dielectric constant of the material which consists of the cavity.

2.2.2 Distributed Bragg Reflectors

In our semiconductor sample, microcavities consist of so-called Distributed Bragg Reflectors (DBRs), which are stacks of semiconductor layers with two different refractive indices. Fig. (2.3) shows a schematic of the sample. We have quantum wells

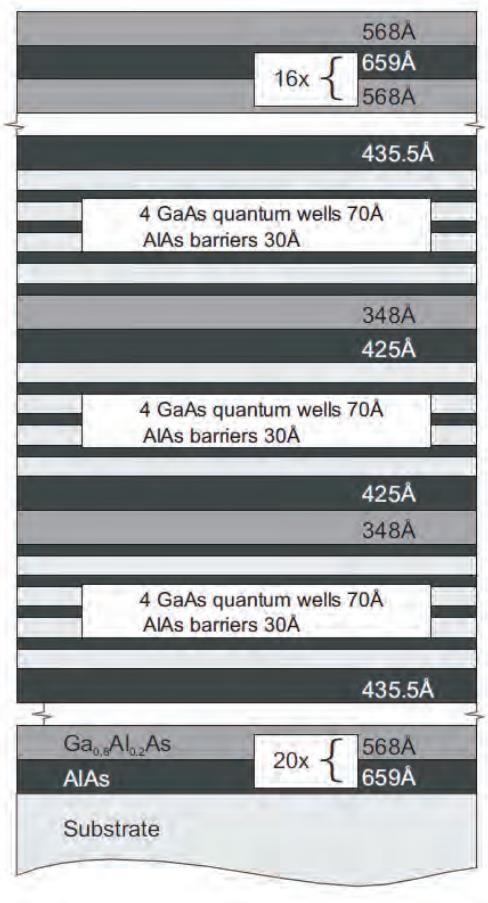

Figure 2.3: A sketch of our sample structure

sandwiched by top and bottom DBRs. Each layer has thickness of $\frac{\lambda}{4}$, where λ is the resonant wave length of the cavity. A typical signature of DBRs is the 'Stop-Band',where the reflectivity is almost 1 and the phase of the reflection coefficient changes linearly as a function of the frequency. We assume the top and bottom DBRs have the same

number of layers below for simplicity. Inside the stop band with N DBR layers [30],

$$r^2 = 1 - 4\frac{n_{ext}}{n_{cav}}\left(\frac{n_1}{n_2}\right)^2 N \quad (n_1 < n_2), \tag{2.36}$$

and

$$\theta_R(w) = \frac{n_{cav}L_{DBR}}{c}(\omega - \omega_m), \tag{2.37}$$

where n_1 and n_2 are the dielectric constants of materials which consist of DBRs, and n_{ext} is the dielectric constant of the surrounding, usually air. ω_m is the center wave length of the stop band and L_{DBR} represents the mirror penetration depth:

$$L_{DBR} = \frac{\lambda}{2}\frac{n_1 n_2}{n_{cav}(n_2 - n_1)} \quad (n_1 < n_2). \tag{2.38}$$

The line-width of the total system is

$$\gamma_c = \frac{1-r}{2r}\frac{c}{n_{cav}(L_c + L_D BR)}. \tag{2.39}$$

2.3 Exciton polaritons

Finally we deduce exciton-polaritons as the new eigenstates of the system due to strong coupling between QW excitons and cavity photons.

2.3.1 Optical properties of quantum well excitons

In this section, we examine the electric dipole coupling between QW excitons and photon fields. According to the principle of the minimal coupling(for example [54]), when a radiation field (described by the vector potential **A**) exists with QW excitons we have additional terms in the Hamiltonian [30]:

$$\mathcal{H}_I = -\frac{e}{mc}\sum_i \mathbf{A}(\mathbf{x_i}) \cdot \mathbf{p_i} + \frac{e^2}{2mc}\sum_i \mathbf{A}^2(\mathbf{x_i}), \tag{2.40}$$

where the index i runs over the all electrons of the system. e is the charge of the electrons, m is the electron mass. The first term describes the interaction between electrons and

radiative fields, and governs the optical property of QW excitons. With the relation of $\frac{\mathbf{p_i}}{m} = \mathbf{v_i}$, the first term can be written as

$$\mathcal{H}_I^{(1)} = -\frac{e}{c}\sum_i \mathbf{A}(\mathbf{x_i}) \cdot \mathbf{v_i}. \tag{2.41}$$

We notice here the Heisenberg equation of motion,

$$\mathbf{v_i} = \frac{1}{i\hbar}[\mathbf{x_i}, \mathcal{H}_{exc}]. \tag{2.42}$$

Here $\mathcal{H}_{exc}$ is the exciton Hamiltonian described in eq. 2.1. We consider the transition matrix element, $\langle 0|\mathcal{H}_I|\mathrm{Ex}\rangle$, where $|0\rangle$ is the crystal ground state and $|\mathrm{Ex}\rangle$ is one exciton state. To calculate the transition matrix, we describe the wave function of $|0\rangle$ and $|\mathrm{Ex}\rangle$ using the Slater determinant of the one particle wave function for valence and conduction band electrons. We also use eq. (2.42) and then we get

$$\langle 0|\mathcal{H}_I|\mathrm{Ex}\rangle = -E_{ex}\frac{e}{c}\int d\mathbf{x_i}\psi_c^*(\mathbf{x_i})\mathbf{A}(\mathbf{x_i}) \cdot \mathbf{x_i}\psi_v(\mathbf{x_i}), \tag{2.43}$$

here ψ_v and ψ_c represent the one particle wave function of the valence band and conduction band electrons. Here E_{ex} is the energy of one exciton state, which is defined as $\mathcal{H}_{exc}|\mathrm{Ex}\rangle = E_{ex}|\mathrm{Ex}\rangle$ (we set the energy of the crystal ground state to be 0). If the wave length of radiation fields can be assumed to be large compared to the atomic periodicity in the semiconductor crystal, we can use the dipole approximation. Applying the dipole approximation to eq.(2.43), we have the transition matrix element:

$$\langle 0|\mathcal{H}_I|\mathrm{Ex}\rangle = -E_{ex}\frac{1}{V}\frac{e}{c}\int d\mathbf{x_i}\psi_c^*(\mathbf{x_i})\epsilon_\mathbf{i} \cdot \mathbf{x_i}\psi_v(\mathbf{x_i}). \tag{2.44}$$

ϵ_i is the polarization vector of the radiation field. For the one particle wave functions, we use the expression as

$$\psi_{c(v)}(\mathbf{x}) = \frac{1}{\sqrt{V}}\sum_i u_{c(v)}(z)\exp(i\mathbf{k}_\parallel^{c(v)} \cdot \mathbf{R_i})v_{c(v)}(\rho), \tag{2.45}$$

where V is the normalization factor, z is the coordinate along the growth direction, $u_{c(v)}$ is the z-axis component of the one particle wave function. $\mathbf{R}_i$ indicates the coordinate for the crystal, ρ is the coordinate in the QW plane, $\mathbf{k}_\parallel^{c(v)}$ is the QW plane momentum of electrons and finally $v_{c(v)}$ is the Bloch wave function. Substituting eq. (2.45) into eq.

(2.44), we have

$$\begin{aligned}\langle 0|\mathcal{H}_I|\mathrm{Ex}\rangle = & - E_{ex}\frac{1}{V}\frac{e}{c}\int dz u_c^*(z)u_v(z) \\ & \times \sum_{R_i}\int_S d\rho \exp(i(\mathbf{k_v}-\mathbf{k_c})\cdot\mathbf{R_i})[(\mathbf{R_i}+\rho)\cdot\epsilon_\mathbf{i}]v_c^*(\rho)v_v(\rho). \end{aligned} \tag{2.46}$$

The last integral in eq. (2.46) is taken over the unit cell S. In the first term of eq. (2.46), the summation $\sum_{R_i}\exp(i(\mathbf{k_v}-\mathbf{k_c})\cdot\mathbf{R_i})\mathbf{R_i}\cdot\epsilon_\mathbf{i}$ is 0, because if $\mathbf{k_v}-\mathbf{k_c}$ is not 0 this term is oscillating and if $\mathbf{k_v}-\mathbf{k_c}$ is 0 the summation of $\mathbf{R_i}\cdot\epsilon_\mathbf{i}$ is 0. Therefore we need to consider only the second term, which can be separated into three parts:

$$\begin{aligned}\langle 0|\mathcal{H}_I|\mathrm{Ex}\rangle = & - \frac{1}{V}\frac{e}{c}\int dz u_c^*(z)u_v(z) \\ & \times \sum_{R_i}\exp(i(\mathbf{k_v}-\mathbf{k_c})\cdot\mathbf{R_i})\int_S d\rho[\rho\cdot\epsilon_\mathbf{i}]v_c^*(\rho)v_v(\rho). \end{aligned} \tag{2.47}$$

Regarding the first integral, we assume $u_c(z)$ and $u_v(z)$ are the same delta function because of the strong confinement due to the QW. The summation part requires that $\mathbf{k_v}-\mathbf{k_c}=0$. The last integral part contains selection rules due to the conservation of the angular momentum. In our GaAs system, the Bloch wave function u_c has 2D s-like symmetry (which means it is symmetric along any direction in 2D), while the Bloch wave function u_v has 2D p-like symmetry (which means it is symmetric along one direction but antisymmetric in another perpendicular direction in 2D). We consider only heavy hole excitons, whose total angular momentum is $J_z=\frac{3}{2}$ with an orbital angular momentum ±1 and spin angular momentum $\pm\frac{1}{2}$. Writing the spin state explicitly, we can write the Bloch wave function for valence band electrons:

$$u_v^{\frac{3}{2}}(\rho)=t_v^+(\rho)\otimes|\uparrow\rangle \quad u_v^{-\frac{3}{2}}(\rho)=t_v^-(\rho)\otimes|\downarrow\rangle. \tag{2.48}$$

Here $t_v^\pm(\rho)=\frac{1}{\sqrt{2}}(t_v^{px}(\rho)\pm it_v^{py}(\rho))$, and $t_v^{px(py)}(\rho)$ is the spatial 'p-like' wave function which is antisymmetric along x(y)-axis. On the other hand, conduction electrons have only spin angular momentum $J_z=\frac{1}{2}$ and then

$$u_c^{\frac{1}{2}}(\rho)=t_c(\rho)\otimes|\uparrow\rangle \quad u_v^{\frac{-1}{2}}(\rho)=t_c(\rho)\otimes|\downarrow\rangle, \tag{2.49}$$

where $t_c(\rho)$ is the spatial 's-like' wave function which is symmetric along every direction in 2D. Therefore the third integral can be written as

$$\int d\rho t_c^*(\rho)[\epsilon\cdot\rho]t_v(\rho)\otimes\langle S_c|S_v\rangle, \tag{2.50}$$

where $|S_{v(c)}\rangle$ represents the spin state of valence (conduction) band electrons, and $\langle S_c|S_v\rangle = \delta_{S_c,S_v}$. For $\int d\rho t_c^*(\rho)[\epsilon \cdot \rho]t_v(\rho)$ to be non zero, the polarization ϵ has to be $\frac{1}{2}(\ 1,\ i\ )$ for the integral with $t_v(\rho) = t_v^{-1}(\rho)$, while $\epsilon = \frac{1}{2}(\ 1,\ -i\ )$ for the integral with $t_v(\rho) = t_v^{1}(\rho)$. This condition is nothing but the conservation low of the total angular momentum(Fig. 2.4).

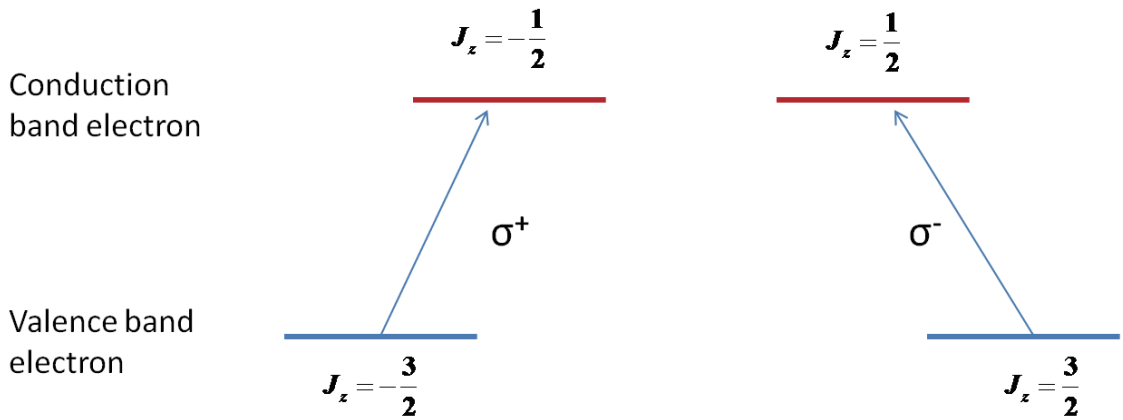

Figure 2.4: A schematic of optical transition of excitons

2.3.2 Exciton Polaritons

In the previous section, we saw the optical property of excitons. Here we consider the case of the strong coupling between excitons and cavity photons, and derive new eigenstates, called lower and upper polaritons. We start with the following second-quantized Hamiltonian [55],

$$\mathcal{H} = \hbar\omega_{ex}\hat{a}^\dagger_{ex,\mathbf{k}}\hat{a}_{ex,\mathbf{k}} + \hbar\omega_c\hat{c}^\dagger_{\mathbf{k}}\hat{c}_{\mathbf{k}} + \hbar\mathcal{G}(\hat{a}^\dagger_{ex,\mathbf{k}}\hat{c}_{\mathbf{k}} + \hat{c}^\dagger_{\mathbf{k}}\hat{a}_{ex,\mathbf{k}}), \tag{2.51}$$

where $\hat{a}_{ex,\mathbf{k}}(\hat{a}^\dagger_{ex,\mathbf{k}})$ and $\hat{c}_{\mathbf{k}}(\hat{c}^\dagger_{\mathbf{k}})$ are the annihilation (creation) operators of QW excitons and cavity photons with momentum $\mathbf{k}$ respectively. $\mathcal{G}$ is the coupling constant between QW excitons and cavity photons, and is proportional to the transition matrix element $\langle 0|\mathcal{H}_I|\mathrm{Ex}\rangle$ (eq.(2.43)). We define here two new modes:

$$\hat{a}_{LP,\mathbf{k}} = X\hat{a}_{ex,\mathbf{k}} + C\hat{c}_{\mathbf{k}} \tag{2.52}$$

$$\hat{a}_{UP,\mathbf{k}} = C\hat{a}_{ex,\mathbf{k}} - X\hat{c}_{\mathbf{k}}. \tag{2.53}$$

With these new modes, we can diagonalize the Hamiltonian of eq.(2.51),

$$\mathcal{H} = \hbar w_{LP,\mathbf{k}} \hat{a}^{\dagger}_{LP,\mathbf{k}} \hat{a}_{LP,\mathbf{k}} + \hbar w_{UP,\mathbf{k}} \hat{a}^{\dagger}_{UP,\mathbf{k}} \hat{a}_{UP,}. \tag{2.54}$$

These two eigenmodes are called 'upper and lower exciton polaritons'. The coefficients X and C denote the amplitudes of excitonic and photonic components for lower polaritons (opposite for upper polaritons).

We consider a simple coupled harmonic oscillator model to discuss the condition for strong or weak coupling. Then the Hamiltonian for exciton modes and cavity photon modes is,

$$\mathcal{H} = \begin{pmatrix} E_{ph} & \hbar\mathcal{G} \\ \hbar\mathcal{G} & E_{ex} \end{pmatrix}, \tag{2.55}$$

where $E_{ph} = \hbar w_{ph} + i\hbar\gamma_{ph}$ and $E_{ex} = \hbar w_{ex} + i\hbar\gamma_{ex}$ are the energy of cavity photons and excitons including their finite line-width. The solution of the eq.(2.55) is

$$E = \hbar \frac{w_{ex} + w_{ph} + i(\gamma_{ex} + \gamma_{ph})}{2} \pm \hbar \left[\mathcal{G}^2 + \frac{1}{4} \left(w_{ex} - w_{ph} + i \left(\gamma_{ex} - \gamma_{ph} \right) \right) \right]^{\frac{1}{2}}. \tag{2.56}$$

When $w_{ex} - w_{ph} = 0$, which is the resonance condition, for $4\mathcal{G}^2 > (\gamma_{ex} - \gamma_{ph})^2$ the value under the square root is positive and the two polariton modes have different energies and same broadening which is given by $\frac{\gamma_{ex}+\gamma_{ph}}{2}$. This condition is called 'strong coupling'. The energy splitting between two polariton modes is

$$2\hbar\Omega = 2\hbar \sqrt{\mathcal{G}^2 - \frac{1}{4}(\gamma_{ex} - \gamma_{ph})^2}, \tag{2.57}$$

which is called 'Rabi splitting'. For $4\mathcal{G}^2 < (\gamma_{ex} - \gamma_{ph})^2$, the two solutions in eq.(2.56) have the same real part, which corresponds to the energy level, and new eigen modes do not appear. This condition is called 'weak coupling'. Next let us restrict to the case of $\gamma_{ex} = 0, \gamma_{ph} = 0$ and define the detuning parameter $\Delta = E_{ph}(k_{\|} = 0) - E_{ex}(k_{\|} = 0)$. The energy of UP and LP is

$$E(k_{\|}) = \frac{E_{ex}(k_{\|}) + E_{ph}(k_{\|})}{2} \pm \left[\hbar^2\mathcal{G}^2 + \frac{1}{4}(E_{ex}(k_{\|}) - E_{ph}(k_{\|}))^2 \right]^{\frac{1}{2}}, \tag{2.58}$$

and the Hopfield coefficient is

$$| X(k_{\|}) |^2 = \frac{1}{2} \left(1 + \frac{E_{ec}(k_{\|}) - E_{ph}(k_{\|})}{\sqrt{(E_{ec}(k_{\|}) - E_{ph}(k_{\|}))^2 + \hbar^2\mathcal{G}^2}} \right) \tag{2.59}$$

$$| C(k_{\|}) |^2 = \frac{1}{2} \left(1 - \frac{E_{ec}(k_{\|}) - E_{ph}(k_{\|})}{\sqrt{(E_{ec}(k_{\|}) - E_{ph}(k_{\|}))^2 + \hbar^2\mathcal{G}^2}} \right). \tag{2.60}$$

Fig. 2.5 shows the detuning dependence of the UP and LP energy at $k_{\|} = 0$ with the energy of cavity photons and QW excitons shown as references. Increasing the detuning

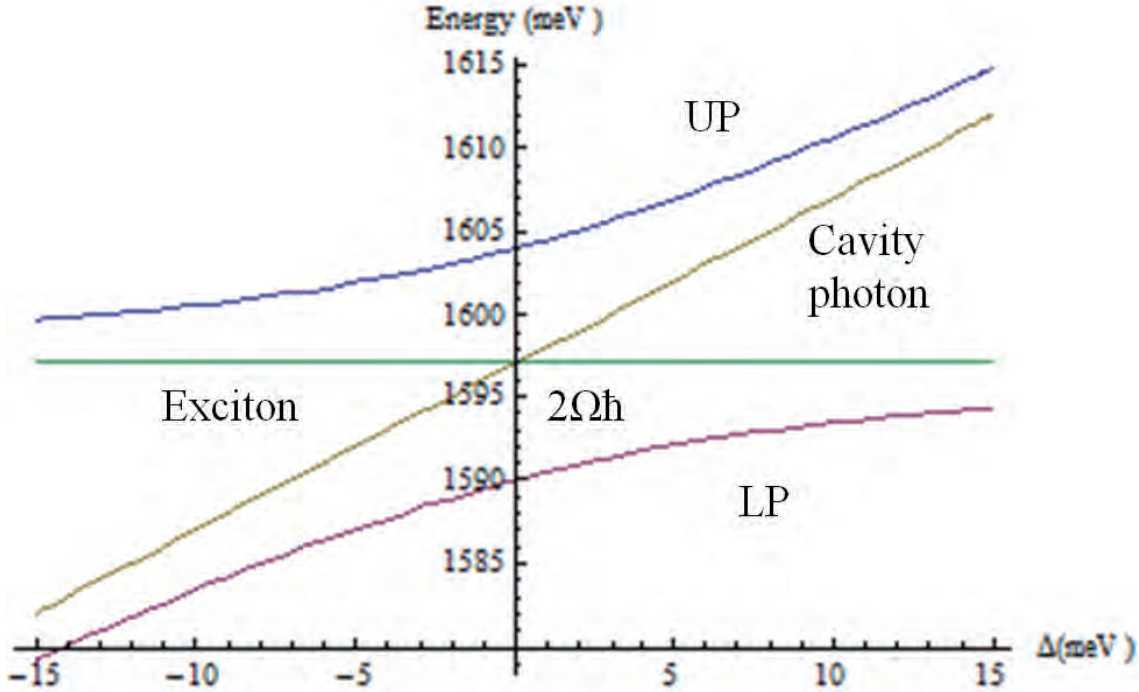

Figure 2.5: Anti-crossing of LP and UP modes. We use the Rabi-splitting $2\Omega\mathcal{G} = 14meV$

from a negative value, a LP mode transitions from photon-like to exciton-like. At $\Delta = 0$, LPs and UPs are half photon and half exciton. Fig. 2.6 shows the dispersion of LP and UP for excitons and photons with $\Delta = -7, 0, 7$ (meV) detuning. In a blue detuning regime (Δ positive), LPs are more exciton-like than that on the resonance ($\Delta = 0$), while LPs are more photon-like in a red detuning regime (Δ negative). We can therefore control the ratio of photon and exciton components through the detuning which can in turn be controlled through the thickness of the cavity and DBRs. This means that we can control the LP (UP) effective mass, which is given in the following form:

$$\frac{1}{m_{LP}} = \frac{|X|^2}{m_{ex}} + \frac{|C|^2}{m_{ph}} \tag{2.61}$$

$$\frac{1}{m_{UP}} = \frac{|C|^2}{m_{ex}} + \frac{|X|^2}{m_{ph}}. \tag{2.62}$$

Here m_{ex} is the exciton mass and m_{ph} is the photon mass.

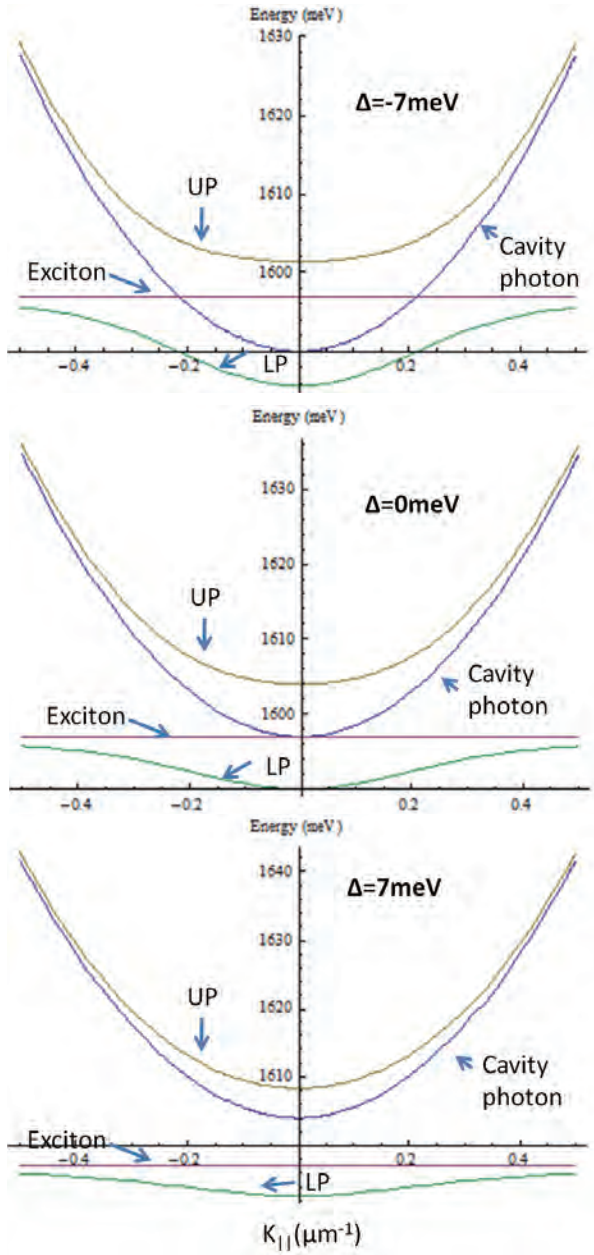

Figure 2.6: UP and LP dispersion at several detuning points. We use the following parameters. $2\Omega\mathcal{G} = 14meV$, the effective photon mass:$m_p h = 10^{-5} m_e$, m_e is the electron mass.

Chapter 3

Bose-Einstein Condensation

In this chapter, we introduce another important concept for this thesis : Bose-Einstein condensation (BEC). We start with the original argument as proposed by Einstein, consisting of a BEC of non-interacting bosons, and then discuss weakly interacting bosons. Finally we review and discuss dynamic condensation of exciton-polaritons.

3.1 An ideal Bose gas

At a temperature T, Bose particles follow the Bose-Einstein distribution [44]:

$$f(\epsilon) = \frac{1}{\exp(\frac{1}{k_B T}(\epsilon - \mu)) - 1}. \tag{3.1}$$

When the system has the density of states $\rho(\epsilon)$, the total number of bosonic particles in the system is,

$$N = \int d\epsilon \rho(\epsilon) f(\epsilon). \tag{3.2}$$

Here we consider Bose particles in a 3D system with its system size L. The density of states in a 3D system is given by

$$\rho_3(\epsilon) = 4\pi(\frac{L}{2\pi})^3 \frac{1}{2}(\frac{2m}{\hbar^2})^{\frac{3}{2}} \epsilon^{\frac{1}{2}}. \tag{3.3}$$

In this case, the integral in eq. (3.2) has the maximum value N_{max} and the corresponding density n_{max} is

$$n_{max} = \frac{N_{max}}{L^3} \simeq 2.612\left(\frac{2\pi m k_B T}{\hbar^3}\right)^{\frac{3}{2}}. \tag{3.4}$$

When we put more than N_{max} particles in this system, in order to follow the Bose-Einstein distribution, the remaining particles can only occupy the ground state. Therefore the number of particles which occupy the ground state becomes macroscopic, which is the phenomena originally termed Bose-Einstein Condensation (BEC). The total density n is written in the form: $n = n_0 + \frac{1}{L^3}\int d\epsilon \rho(\epsilon) f(\epsilon)$. For ideal Bose gases, BEC in 1D and 2D systems confined in a size L or L^2 respectively cannot occur. This is easily seen when we consider the integral for the total particle number. The density of states in 1D and 2D is

$$\begin{aligned} \rho_1(\epsilon) &= \frac{L}{2\pi}\frac{1}{2}(\frac{2m}{\hbar^2})^{\frac{1}{2}}\epsilon^{-\frac{1}{2}} \\ \rho_2(\epsilon) &= \pi(\frac{L}{2\pi})^2\frac{1}{2}(\frac{2m}{\hbar^2}), \end{aligned} \tag{3.5}$$

so that the integrals for the total particle number do not have a finite maximum number. Therefore Bose-Einstein condensation in 1D and 2D infinite system cannot occur. This originates from the fact that the density of states in 1D and 2D do not go to 0 at $\epsilon = 0$ (fig. 3.1). We note that even in 1D and 2D, with a trap potential BEC can occur, because the density of states is modulated. For a 3D system, eq. (3.4) can be considered as the threshold relation between the density and the temperature of the system for BEC. In this relation, the mass takes an important role. With a fixed density, particles with lighter mass have a higher critical temperature. This is valid for BEC in 1D and 2D with a trap potential. Because polaritons have a much lighter mass, which is four orders of magnitude of lighter than excitons and eight orders of magnitude of lighter than hydrogen atoms, the critical temperature for BEC of a polariton system is much higher than in other systems.

BEC is also understood phenomenologically in the following manner. A particle has a typical length which characterise the region where the particle wavefunciton occupies. This characteristic length is called "thermal de Broglie wave length" and defined as follows Consider a particle with a temperature T, and an energy of $k_B T$ (k_B is the Boltzmann constant). The particle has the energy of the vibration mode, which is $\frac{\hbar^2}{2m}\frac{2\pi^2}{\lambda_T^2}$ (m is the mass of the particle, and λ_T is the thermal de Broglie wave length). So

that the thermal de Broglie wave length is defined as

$$\lambda_T \sim \sqrt{\frac{2\pi^2\hbar^2}{mk_BT}} \tag{3.6}$$

Thus thermal de Broglie wave length is inversely proportional to the square root of the temperature. With decreasing temperature (or increasing density), the thermal de Broglie wave length approache the inter-particle distance. When the thermal de Broglie wave length becomes comparable to the inter-particle distance, the particle waves interfere with each other. Phase coherence is then formed in the system, and condensation occurs.

3.2 Weakly interacting Bose gas

Next we consider Bose particles with weakly repulsive interaction. In this case, condensation still occurs [44]. We introduce the order parameter, and Gross-Pitaevskii equation which describe the motion of the order parameter. And then we discuss superfluidity and quantized vortices.

3.2.1 Order parameter and Gross-Pitaevskii equation

First we assume three conditions for weakly interacting Bose gas:

1. weakly interacting
2. cold gas condition
3. dilute gas condition

1: We assume the range of the inter-particle force r_c is much smaller than the inter-particle distance d:

$$r_c \ll d(= n^{-\frac{1}{3}}), \tag{3.7}$$

which allow us to consider only two-body collisions.

2: We assume the kinetic energy of particles is enough low that we can consider only s-wave scattering. This condition can be written

$$p \sim \sqrt{2mk_BT} \ll \frac{\hbar}{r_c}, \tag{3.8}$$

where p is the momentum of particles.

3: We assume the Bose gas is dilute enough that the following condition

$$n|a|^3 \ll 1 \tag{3.9}$$

is satisfied, where a is the s-wave scattering length.

We now introduce the 'order parameter'. The field operator of Bose particles can be written as

$$\hat{\Psi}(r) = \sum_i \psi_i(r)\hat{a}_i, \tag{3.10}$$

where $\psi_i(r)$ is the single particle wave function of the ith state and $\hat{a}_i$ is the annihilation operator of the i the state. When BEC is formed, we can separate the ground state contribution:

$$\hat{\Psi}(r) = \psi_0(r)\hat{a}_0 + \sum_{i\neq 0} \psi_i(r)\hat{a}_i. \tag{3.11}$$

Here the commutator of $\hat{a}_0$ and $\hat{a}_0{}^\dagger$, which is 1, is much smaller than the operator $\hat{a}_0$ and $\hat{a}_0{}^\dagger$ themselves which are order of $\sqrt{N_0}$. Therefore we can approximate the operators to be complex number $\sqrt{N_0}$, then we get

$$\hat{\Psi}(r) = \Psi_0(r) + \delta\hat{\Psi}(r), \tag{3.12}$$

where $\Psi_0(r) = \sqrt{N_0}exp(i\Theta(r))$ and $\delta\hat{\Psi}(r) = \sum_{i\neq 0} \psi_i(r)\hat{a}_i$. At the zero-th order, we ignore $\delta\hat{\Psi}(r)$ and $\Psi_0(r)$ is called 'order parameter'. The order parameter is the expectation value of the field operator $\langle\hat{\Psi}(r)\rangle$. If the state is a number state, the expectation value is zero. Theoretically the condensed state is close to the coherent state

$$|\alpha\rangle = \sum_n \frac{\exp(-\frac{|\alpha|^2}{2})}{\sqrt{n!}}\alpha^n|n\rangle, \tag{3.13}$$

which is the eigen state of the annihilation operator.

The equation of motion for the order parameter, 'Gross-Pitaevskii (GP) equation' can be deduced from the general Hamiltonian with two-body collisions:

$$\begin{aligned}\hat{\mathcal{H}} &= -\int d\mathbf{x}\hat{\Psi}^\dagger(\mathbf{x},t)\left(\frac{\hbar^2}{2m}\nabla^2 + V(\mathbf{x})\right)\hat{\Psi}(\mathbf{x},t) \\ &+ \int d\mathbf{x}d\mathbf{x}'\hat{\Psi}^\dagger(\mathbf{x}',t)\hat{\Psi}^\dagger(\mathbf{x},t)\hat{U}(\mathbf{x}-\mathbf{x}')\hat{\Psi}(\mathbf{x},t)\hat{\Psi}(\mathbf{x}',t).\end{aligned} \tag{3.14}$$

The field operator $\hat{\Psi}(\mathbf{x})$ obeys the Heisenberg equation of motion:

$$\begin{aligned} i\hbar\frac{\partial}{\partial t}\hat{\Psi}(\mathbf{x},t) &= [\hat{\Psi}(\mathbf{x},t),\mathcal{H}] \\ &= \left[-\frac{\hbar^2\nabla^2}{2m} + V(\mathbf{x}) + \int d\mathbf{x}'\hat{\Psi}^\dagger(\mathbf{x}')\hat{U}(\mathbf{x}-\mathbf{x}')\hat{\Psi}(\mathbf{x}')\right]\hat{\Psi}(\mathbf{x}). \end{aligned} \tag{3.15}$$

Replacing the field operator in eq.(3.15) with the order parameter, we get the GP equation:

$$i\hbar\frac{\partial}{\partial t}\Psi_0(\mathbf{x},t) = \left[-\frac{\hbar^2\nabla^2}{2m} + V(\mathbf{x}) + g \mid \Psi_0(\mathbf{x},t) \mid^2\right]\Psi_0(\mathbf{x},t), \tag{3.16}$$

where $g = \frac{4\pi\hbar^2 a}{m}$ is the interaction constant. The energy of the system is written

$$E = \int d\mathbf{r}\left(\frac{\hbar^2}{2m}|\nabla\Psi_0|^2 + V(\mathbf{r}) + \frac{g}{2}|\Psi_0|^2\right). \tag{3.17}$$

Setting the energy of the non-interacting ground state as 0, we have

$$E = \frac{gN^2}{2V_0}, \tag{3.18}$$

where V_0 is the volume of the system and N is the total particle number. The chemical potential is defined as

$$\mu = \frac{\partial E}{\partial N} = gn \tag{3.19}$$

where n is the particle density. The order parameter evolves in time as

$$\Psi_0(\mathbf{r},t) = \exp(-i\frac{\mu}{\hbar}t)\Psi_0(\mathbf{r}). \tag{3.20}$$

Then we have the GP equation for the stationary state $\Psi_0(\mathbf{r})$,

$$\left(-\frac{\hbar^2}{2m}\nabla^2 + V(\mathbf{r}) - \mu + g|\Psi_0(\mathbf{r})|^2\right)\Psi_0(\mathbf{r}) = 0. \tag{3.21}$$

Next we consider the excitation modes of the ground state condensates by a linearization of the GP equation. The order parameter which includes the excitation is written in the form of

$$\Psi(\mathbf{r},t) = \exp(-i\frac{\mu}{\hbar}t)\Psi_0(\mathbf{r})\left(1 + u_k(\mathbf{r})\mathrm{e}^{i(\mathbf{kr}-wt)} + v_k(\mathbf{r})\mathrm{e}^{-i(\mathbf{kr}-wt)})\right). \tag{3.22}$$

We assume the ground state of an uniform gas ($V(\mathbf{r}) = 0$), where $\Psi_0(\mathbf{r}) = \sqrt{n}$, $\mu = gn$, and $u_k(\mathbf{r})\,(v_k(\mathbf{r})) = u_k(v_k)$. By substituting eq. (3.22) into the GP equation (eq. 3.16) and collecting terms which evolve in time like e^{iwt} and e^{-iwt} respectively, we have

$$\begin{aligned} \hbar w u_k &= \left(\frac{\hbar^2 k^2}{2m} + gn\right) u_k + gn v_k \\ \hbar w v_k &= gn u_k + \left(\frac{\hbar^2 k^2}{2m} + gn\right) v_k. \end{aligned} \tag{3.23}$$

To have non-zero solutions for u_k and v_k, we have

$$\begin{aligned} (\hbar w)^2 &= \left(\frac{\hbar^2 k^2}{2m}\right)^2 + \frac{\hbar^2 k^2}{m} gn \\ \therefore \hbar w &= \sqrt{\left(\frac{\hbar^2 k^2}{2m}\right)^2 + \frac{\hbar^2 k^2}{m} gn}. \end{aligned} \tag{3.24}$$

Eq. (3.24) determines the dispersion of the excitation modes, and these modes are called Bogoliubov excitations [45]. We note that in the small k regime the Bogoliubov modes are phonon like $\hbar w \sim \frac{\hbar k}{m} gn$ (linearly proportional to the momentum (wave number)), while in the large k regime they are particle like $\hbar w \sim \frac{\hbar^2 k^2}{2m}$ (fig. 3.2). The transition point is characterised by the relation of

$$\left(\frac{\hbar^2 k_c^2}{2m}\right)^2 \sim \frac{\hbar^2 k_c^2}{m} gn, \tag{3.25}$$

where the characteristic length 'healing length' is defined as

$$\xi = \frac{2\pi}{k_c} = \frac{\hbar}{\sqrt{2mgn}}. \tag{3.26}$$

3.2.2 Superfluidity

Superfluids can flow through capillaries without any dissipation. A BEC of weakly interacting bosons has the property of superfluidity. We here consider Landau's criteria of superfluidity [44], which is based on a Galilean transformation. Consider a fluid with an energy E and momentum P in the reference frame K. In the frame K′ moving at the velocity V respect to the reference frame, the fluid has an energy E' and momentum

P' :

$$\begin{aligned} P' &= P - MV \\ E' &= \frac{P'^2}{2M} \\ &= E - P \cdot V + \frac{1}{2}MV^2, \end{aligned} \tag{3.27}$$

where $E = \frac{p^2}{2m}$ and M is the total mass of the fluid. We consider condensates moving at the velocity v in a capillary. Let a reference frame move at the velocity v. If a single Bogoliubov quasi particle with momentum p is created by the friction with the capillary wall, the total energy E in the frame K is $E_0 + \epsilon(p)$. And then we move to the moving frame K′ at the velocity $-v$ respect to the reference frame in which the capillary is at rest. In the moving frame, the energy and the momentum is

$$\begin{aligned} E' &= E_0 + \epsilon(p) - p \cdot (-v) + \frac{1}{2}M(-v)^2 \\ P' &= p - M(-v). \end{aligned} \tag{3.28}$$

Eq. (3.28) indicates the change in energy and in momentum caused by the creation of Bogoliubov excitation are $\epsilon(p) + pv$ and p respectively. Spontaneous creation of excitation happens if and only if such processes are energetically favorable. Namely it is the case that the energy change $\epsilon(p) + pv$ is negative in the moving frame. If $\epsilon(p) + pv > 0$, excitation does not occur and then there is no dissipation or friction. It is just superfluid. The critical velocity can be defined as

$$v_c E = \min_p \frac{\epsilon(p)}{|p|}. \tag{3.29}$$

Looking at the dispersion of Bogoliubov excitation, they have the minimum value of $\frac{\epsilon(p)}{|p|}$, where $c = \sqrt{\frac{gn}{m}}$ (the sound velocity). Therefore if the condensate flows at a velocity less than c, it behaves as superfluid.

3.2.3 A quantized vortex

A quantized vortex is a stationary solution of the GP equation, which is considered to be linked to superfluidity [46]. One of peculiar properties of quantized vortices is that they have a core region where the density goes to zero, whose size is of the order

of the healing length. Quantized vortex states have non-zero angular momentum. The solutions can be found of the form of

$$\Psi_0(r) = \mathrm{e}^{is\theta(r)}|\Psi_0(r)|, \tag{3.30}$$

where r and θ are cylindrical coordinates. The parameter s should be integer to ensure that the order parameter is single valued, and the state of eq. (3.30) is the eigenstate of the angular momentum $l_z = s\hbar$. (The total angular momentum is $L_z = Nl_z$.) This state is rotating around the core with a velocity of

$$\begin{aligned} v &= \frac{\hbar s}{m}\nabla\theta(\mathbf{r}, t) \\ &= \frac{\hbar}{m}\frac{s}{r} \end{aligned} \tag{3.31}$$

In contrast, the tangential velocity of a rigid rotational field $v = \Omega \times r$ is linearly proportional to $|r|$.

Substituting eq. (3.30) into the GP equation eq. (3.21), we have

$$-\frac{\hbar^2}{2m}\frac{1}{r}\frac{\partial}{\partial r}\left(r\frac{\partial|\psi_0|}{\partial r}\right) + \frac{\hbar^2 s^2}{2mr^2}|\Psi_0| + g|\Psi_0|^2 - \mu|\Psi_0| = 0 \tag{3.32}$$

Fig. (3.3) shows the normalized $|\Psi_0(r)|$. The size of the core region increases with s. The energy of a quantized vortex E_s can be calculated with eq. 3.17, and is linearly proportional to s^2 [44]. In the rotating frame with angular velocity Ω, the Hamiltonian is $H = H_0 - \Omega L_z$, where H_0 is the Hamiltonian in the laboratory frame. Then if Ω is sufficiently large, the vortex solution with angular momentum $L_z = N\hbar(s = 1)$ is energetically favorable with respect to the ground state solution H_0.

3.3 Dynamic condensation of exciton polaritons

Exciton-polaritons have been considered as promising candidates for BEC in solids, and several groups have been reported dynamic condensation of LPs. In this section, we briefly review several properties of LP condensation.

Potential trap

Several methods to implement potential traps for LPs have been demonstrated, such as thin metal traps [31] [32], direct modulation of the cavity layer length [35] [36], etched pillars [37] [38] , surface acoustic waves [34], and imaginary potentials [33]. Here we explain thin metal traps, which we adopt in this thesis.

Thin Ti/Au metal layers deposited on the surface of the semiconductor changes the boundary condition for light. With the presence of a DBR, this changes the resonance condition of the cavity photon to a shorter wave length. Because LPs are superposition states of QW excitons and cavity photons, the energy of LPs is raised. Fig. (3.4) shows the calculated LP energy by the transfer matrix method [40], and fig. (3.5) shows the experimentally measured LP energy modulation. With increasing the thickness of the metal layer, the magnitude of the potential modulation first increases and then saturates. With increasing the thickness of the metal layer, the magnitude of the potential modulation first increases and then saturates. The metal layer absorbs photons, so that there is a limit to the thickness of the metal layers for pumping and detection. Fig. (3.4) shows the case of 3nmTi/20nmAu metal layers, which shows $\sim 100\mu$eV modulations.

Relaxation mechanism

LPs are injected resonantly with large in-plane momentum or non-resonantly (for example on the resonance of UPs). In the former scheme, injected LPs first relax into the lower energy states due to the scattering with phonons. In the region of the bottle-neck region (where the momentum is close to the $k_{\parallel}^{b}$, which is the typical momentum where the LPs changes from exciton-like to photon-like), this cooling mechanism becomes inefficient. Within region $k_{\parallel}^{b}$, the main mechanism of LP cooling is considered to be LP-LP scattering, similar to evaporative cooling for cold atoms. Namely when two LPs in the bottle-neck region collide, one is scattered into the lower energy state which is cooled while the other is excited. Fig. 3.6 shows the schematic of the relaxation mechanism of LPs. For the relaxation due to the LP-LP scattering to occur, a reasonable of LP density is required. When the injected LPs are of insufficient density, LPs leak at the bottleneck region before relaxing into the lower states. Another important mechanism is bosonic stimulated scattering. The rate in which bosons are scattered into the state is proportional to the number of bosons in the state [56]. Therefore when the number of bosons in a state (usually the ground state) exceeds one, the scattering into this state is stimulated.

Lifetime

EPs have a short lifetime due to the leakage of photons from the cavity, which leads to a peculiar effects in LP condensation. As is seen above, LPs relax through the scattering with phonons and themselves. Due to their short lifetime, LPs may leak before reaching thermal equilibrium. Even in such cases, with a enough large LP density and a enough low temperature, LP condensation can occur. But this is not condensation at equilibrium, but rather dynamic condensation.

Open dissipative GP equation

The Gross-Pitaevskii equation can be modified to account for the open-dissipative nature of LPs [39]. Not only are the effects of the finite lifetime of LPs included, but also the effect of the existence of a non-condensed LPs population. Here we only shows the result:

$$\begin{aligned} i\hbar\frac{\partial}{\partial t}\Psi_0(\mathbf{x},t) &= \Big[-\frac{\hbar^2\nabla^2}{2m} + g \mid \Psi_0(\mathbf{x},t) \mid^2 \\ &+ g_R n_R(\mathbf{x},t) - i\hbar\left(\gamma_c - \gamma_s n_R\left(\mathbf{x},t\right)\right)\Big]\Psi_0(\mathbf{x},t) \qquad (3.33) \\ \frac{\partial}{\partial t}n_R(\mathbf{x},t) &= P(\mathbf{x},t) - \gamma_R n_R(\mathbf{x},t) - \gamma_s \mid \psi_0(\mathbf{x},t) \mid^2, \qquad (3.34) \end{aligned}$$

where the GP equation for the order parameter $\Psi_0(\mathbf{x},t)$ is coupled to the rate equation of the reservoir LPs $n_R(\mathbf{x},t)$. γ_c is the decay rate for the condensed LPs, γ_s is the rate of the stimulated scattering from the reservoir to the condensed state, g_R is the interaction constant due to the interaction with LPs in the reservoir, γ_R is the decay rate of the reservoir LPs, and $P(\mathbf{x},t)$ is the pump profile.

3.4 Meta-stable condensation in excited states

Condensation occurs when a sufficient large number of particles exist in one state, therefore condensation in excited states is also possible. In a polariton system, such meta-stable condensation has been observed in 1D periodic potentials [32], while in an atomic system one paper recently appeared [47]. We note that the mechanism to prepare particles in excited states in both system is different [48].

In the polariton system, the short lifetime and relaxation mechanism are the key for the occurence of meta-stable condensation. Consider one excited state. LPs relax into this state (from the higher energy states), and also relax out of this state (into the energy lower states). When the rate of LPs relaxing into the state is more than the rate of LPs relaxing out the state, LPs collect in this state and this state become meta-stable. If LPs have an infinite lifetime, all LPs finally relax into the ground state. But with a finite lifetime, LPs may leak from the system by emitting photons before relaxing into the lower energy state. If the LP number in this state exceeds a critical number, meta-stable condensation in this state occurs and we can detect it through spectroscopy. Excited state condensation has been observed in one dimensional periodic lattice potentials [32]. In this work, periodic potentials are implemented by a series of thin metal traps.

One-dimensional periodic potentials form a band structure (fig. 3.7b). The state in the bottom of the second band becomes meta-stable, because inter-band relaxation is suppressed. Fig. (3.7a) and (3.7c) show the experimentally observed far field (momentum space) image (a) below and (c) above the threshold pump power. In fig. (3.7a) not only the original LP dispersion at the center, but also replicas due to the periodic potentials can be seen. Above the threshold pump power, not only the intensity peak from the condensate in the ground state (indicated C in fig. (3.7c)) but also the intensity peak from the condensate in the excited state (indicated A in fig. (3.7c)) can be seen. We note that this meta-stable state has a wavefunction which is antisymmetric with respect to the trap center and connected in a‘ π ’ phase with the neighboring sites, while the ground state is symmetric and connected with 0 phase (fig. (3.7d)).

This meta-stable condensation can be modelled by a simple set of coupled rate equations as follows.

Assumptions

- The system can be modelled by three states, the pumped reservoir (state ‘ 3 ’) where LPs thermally distributed, the meta-stable ‘ π ’-state (state ‘ 2 ’), and the ground ‘ 0 ’-state (state ‘ 1 ’).
- Pumped LPs in state ‘ 3 ’ can relax into state ‘ 2 ’ or state ‘ 1 ’, or leak from the cavity.
- LPs in state ‘ 2 ’ can relax into state ‘ 1 ’ or leak from the cavity.
- LPs in state ‘ 1 ’ can only leak from the cavity.

With the above settings, the coupled rate equation for the LP density in each state n_1, n_2, n_3 is

$$\frac{dn_3(t)}{dt} = -\Gamma_3 n_3 - \Gamma_{32} n_3(n_2+1) - \Gamma_{31} n_3(n_1+1) \tag{3.35}$$

$$\frac{dn_2(t)}{dt} = -\Gamma_2 n_2 + \Gamma_{32} n_3(n_2+1) - \Gamma_{21} n_2(n_1+1) \tag{3.36}$$

$$\frac{dn_3(t)}{dt} = -\Gamma_1 n_1 + \Gamma_{31} n_3(n_1+1) + \Gamma_{21} n_2(n_1+1), \tag{3.37}$$

where Γ_i is the radiative decay rate of state‘ i ’, and Γ_{ij} is the transition rate from state‘ i ’ to state ‘ j ’ (A schematic of this model is shown in fig. (3.9)). To solve this equation, a few assumptions are needed. First, assuming instantaneous initial pumping, the initial values of n_i are set $[n_1(t=0), n_2(t=0), n_3(t=0)] = [0, 0, n_p]$. Second, the time

integrated LP emission intensity from state ' i ' is proportional to $\in \Gamma_i n_i(t)dt$. Third, because the LPs in state ' 3 ' are exciton-like, Γ_3 is small as compared to Γ_2 and Γ_1. Lastly, because the LP relaxation is considered to proceed gradually from high to low in-plane in-plane momentum, the transition rate Γ_{31} is much smaller than Γ_{32}. After these approximations, the parameters $\Gamma_3 = 300^{-1}$, $\Gamma_1 \sim \Gamma_2 = 10^{-1}$, $\Gamma_{21} = 25^{-1}$, $\Gamma_{32} = 20^{-1}$, $\Gamma_{31} = 100^{-1}(ps^{-1})$ are used in Ref. [32]. Fig. (3.9) shows the experimentally measured and the calculated integrated LP emission of ' 0 '-state and ' π '-state. It is clearly seen that the above model actually follow the qualitative feature of the mode competition.

3.5 Orbital states

As we have seen in the last section, meta-stable condensation occurs at excited states (in the previous example, the order parameter is antisymmetric against the trap center.). Generally excited states have various kinds of symmetry. Here we briefly introduce orbital states in an infinite 2D cylindric well potential. An infinite 2D cylindric potential can be written as

$$\begin{aligned} V(r) &= 0 \ (r \leq a) \\ &= \infty \ (r > a), \end{aligned} \tag{3.38}$$

where $r = \sqrt{x^2 + y^2}$. In this case, the angular momentum along the z-axis is a good quantum number, so that the eigenfunction can be written in the form

$$\psi(r, \theta) = R(r) \exp(il_z\theta) \tag{3.39}$$

where we use the polar coordinates (r, θ).

The radial wavefunctions $R(r)$ are also characterized by a good quantum number represented by b. The lowest energy state $(b, l_z) = (0, 0)$ is plotted in fig. (3.10a). This state is perfectly symmetric around the trap center, and we call this type of state '1s' in analogy to the 3D case. States $(0, 1)$ and $(0, -1)$ are degenerate, and have 2π phase rotation around the trap center. Because these two are degenerate, any superposition has also the same energy. We plot $|(0, 1)\rangle \pm i|(0, 1)\rangle$ state in fig. (3.10b,c), and we call these $2p_x$ and $2p_y$ respectively. p_x-state is symmetric along y-axis which anti-symmetric along x-axis (opposite for p_y). States $(0, 2)$ and $(0, -2)$ are also degenerate, and we call $|(0, 1)\rangle \pm i|(0, 1)\rangle$ $3d_{xy}$ and $3d_{x^2-y^2}$ (fig. (3.10d,e)). Because they originates from states which have 4π rotation, they have two axes of symmetry and of anti-symmetry respectively. Finally we plot $2s$ state $(1, 0)$ (fig. (3.10f)). $2s$ is also perfectly symmetric around the trap center, but they have node.

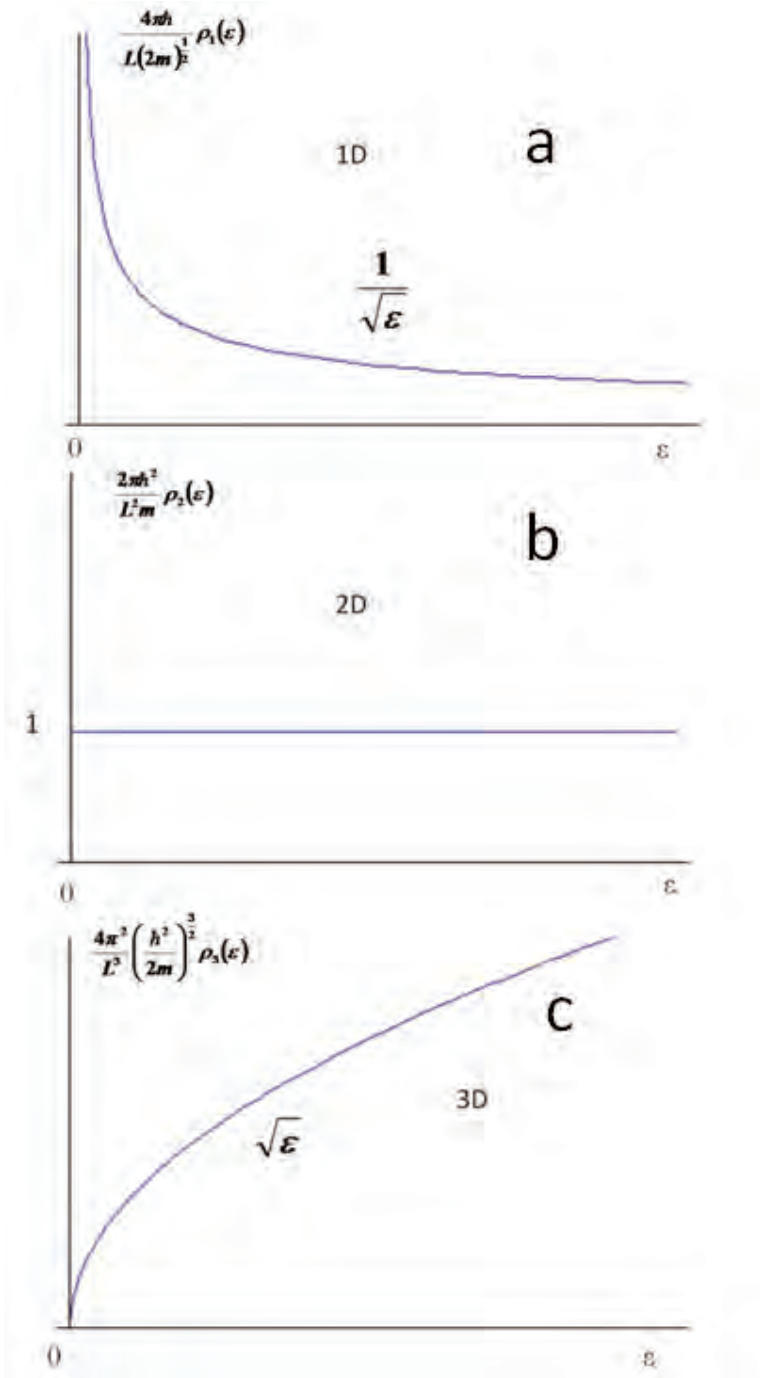

Figure 3.1: The energy dependence of the normalized density of states for (a) 1D, (b) 2D and (c) 3D. The horizontal axis is the energy, and the vertical is the normalized density of states. They are (a) inversely proportional to $\sqrt{\epsilon}$, (b) independent, and (c) proportional to $\sqrt{\epsilon}$ respectively.

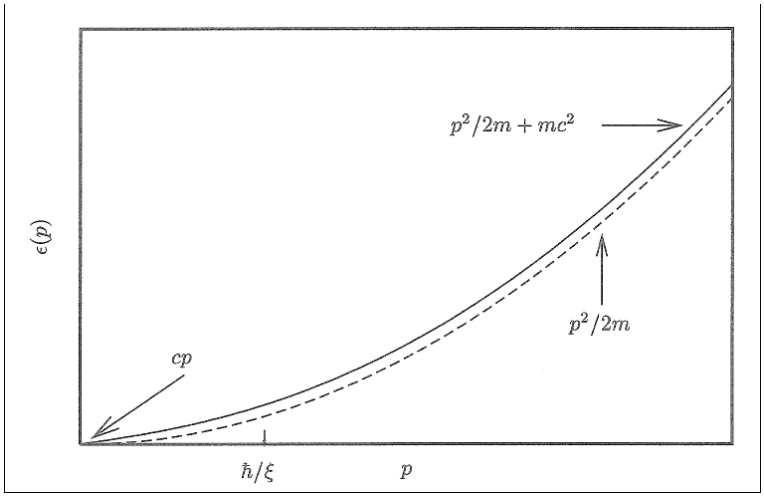

Figure 3.2: Bogoliubov dispersion (solid line). A dashed line is non-interacting particle dispersion for reference. (from ref. [44])

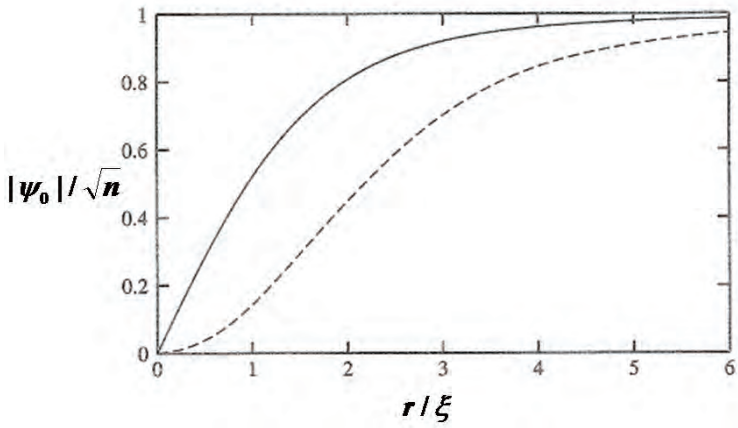

Figure 3.3: The absolute value of of the order parameters of vortex solutions s=1(solid), 2(dashed). (from ref. [44])

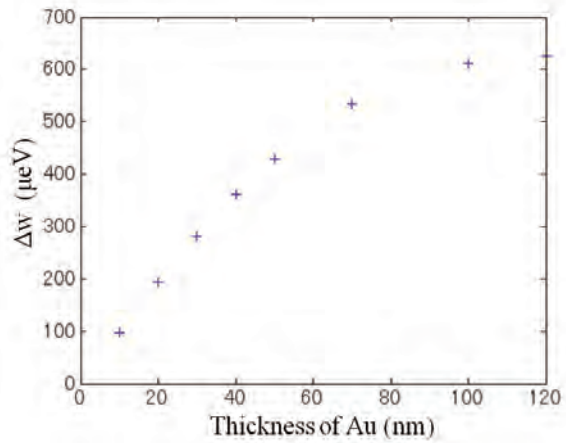

Figure 3.4: Calculated energy shift of the resonant photon field due to the thin Au layer. We set the resonance 770nm and assume only Au layer is present.

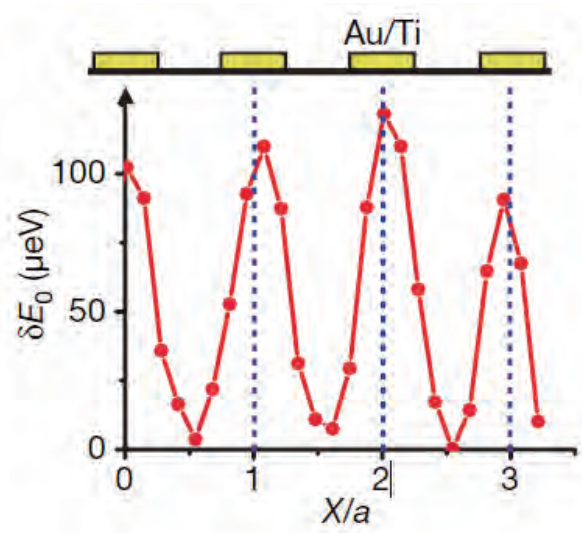

Figure 3.5: Experimentally detected LP energy shift with Ti(3nm)/Au(20nm) from ref. [32].

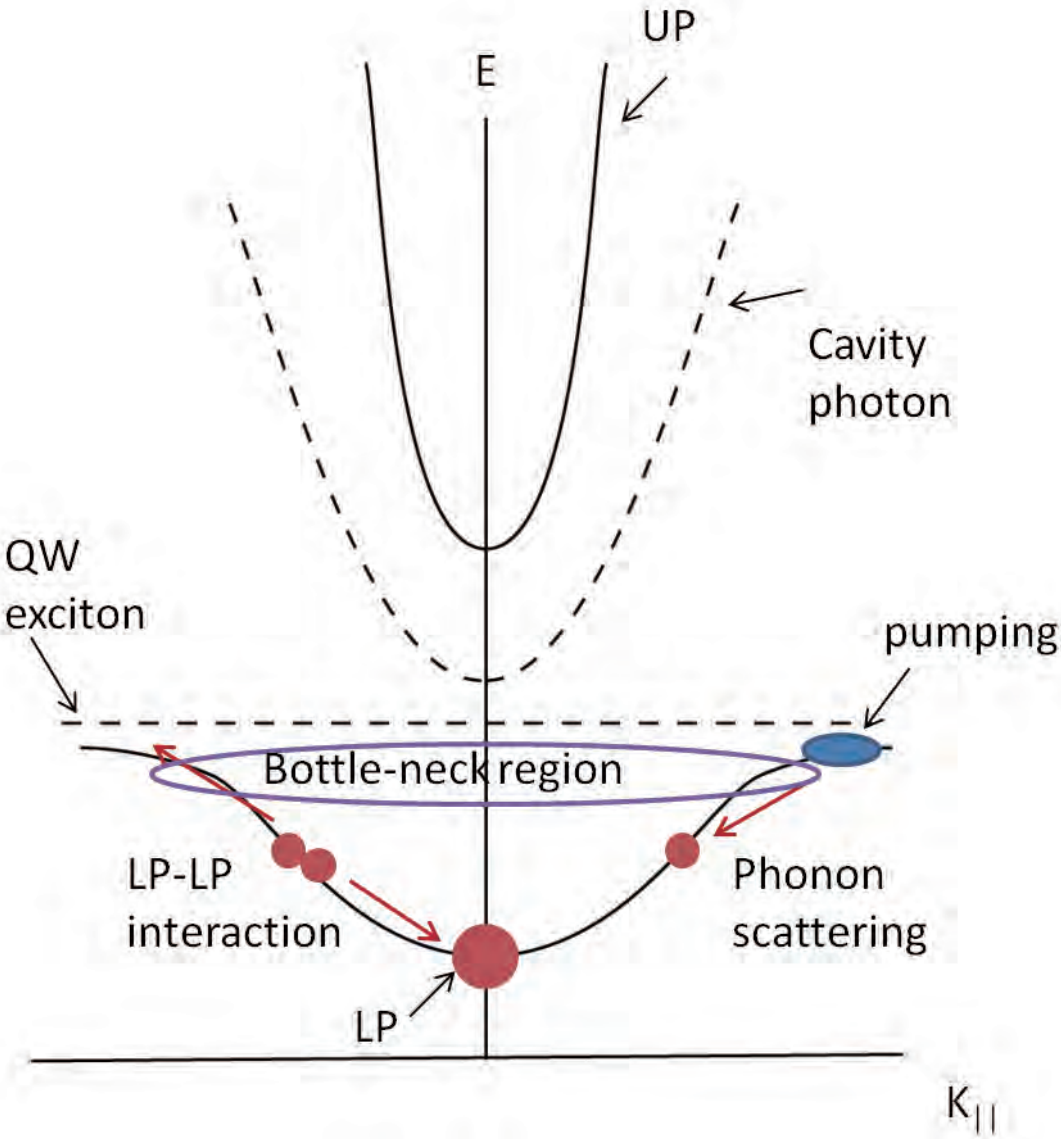

Figure 3.6: A schematic of the LP relaxation mechanism.

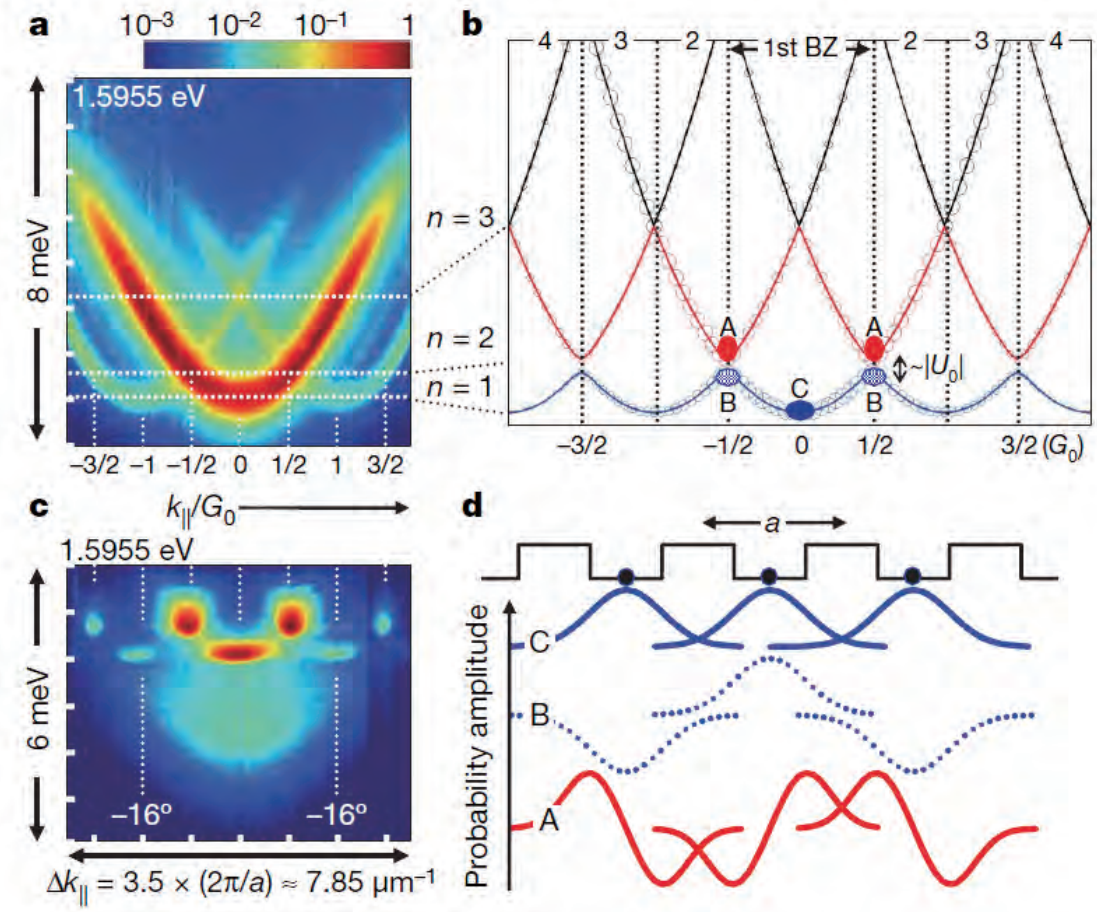

Figure 3.7: From ref. [32]. (a) shows the dispersion below the threshold. (b) shows the band structure of 1D lattice potentials. (c) shows the dispersion above the threshold. (d) shows the near-field wavefunctions at A, B, C in (b)

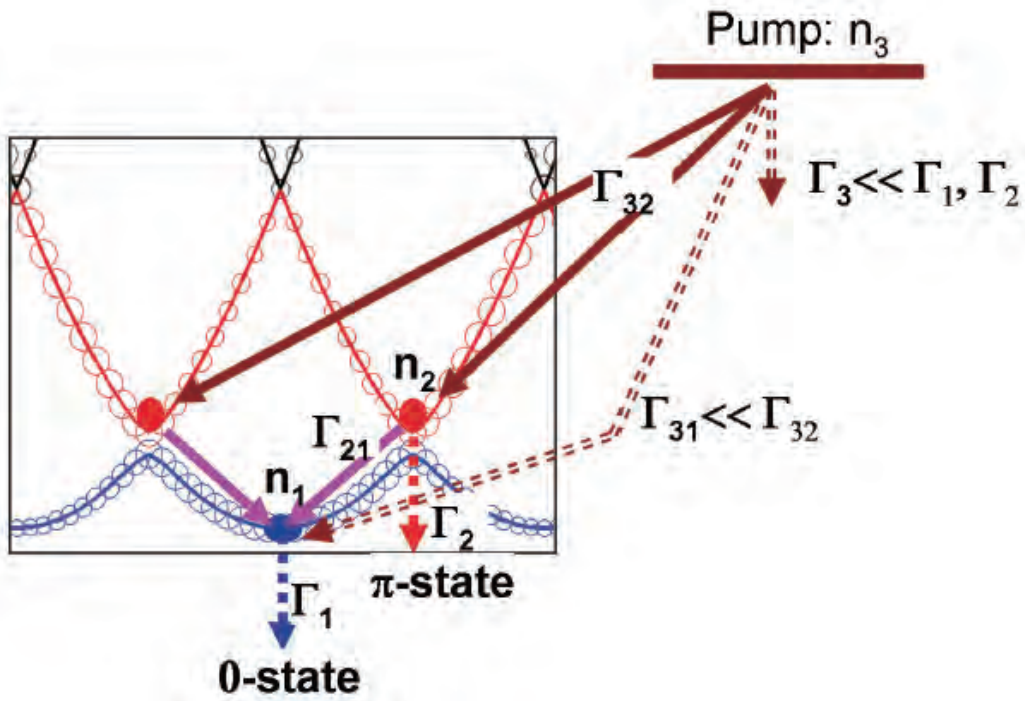

Figure 3.8: Schematic of the relaxation model for the coupled rate equation. from ref. [32].

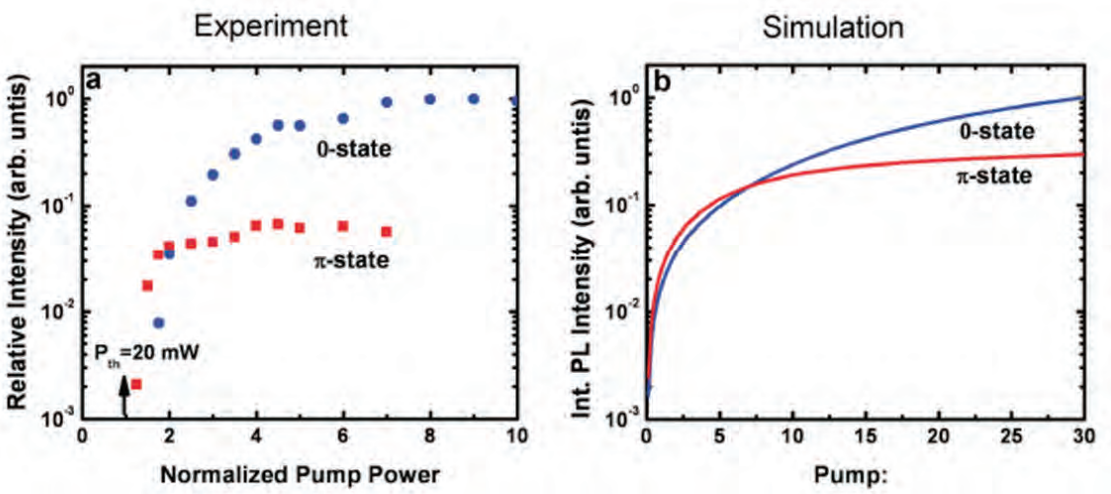

Figure 3.9: Integrated LP emission intensities versus pump power. (a) The experimentally obtained data of the ground state and the meta-stable state. (b) The result of the numerical simulation of the rate equations. from ref. [32].

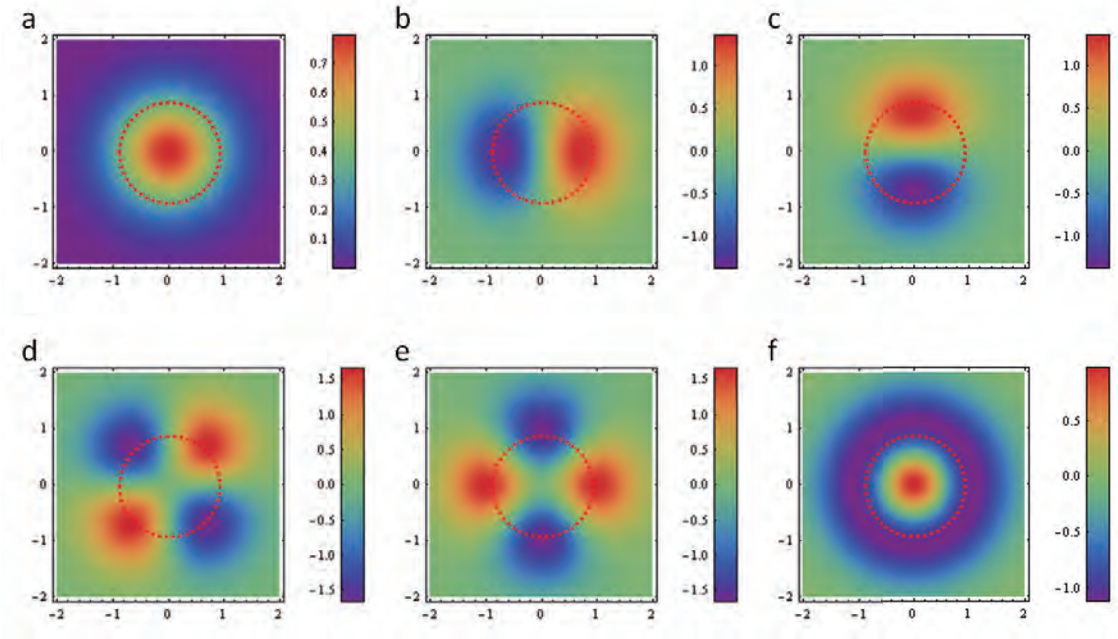

Figure 3.10: The value of the wavefunctions in a cryndrical trap indicated by red dashed lines for (a) $1s$, (b) $2p_x$, (c) $2p_y$, (d) $3d_{xy}$, (e) $3d_{x^2-y^2}$, and (f) $2s$ normalized by arbitrary values.

Chapter 4

Experimental Set-Up

In this chapter, we explain the sample structure, the fabrication, and the set-up of optics.

4.1 Device structure

The microcavity structure consists (fig. 2.3) of a $\lambda/2$ AlAs cavity sandwiched by two distributed Bragg reflectors with alternating GaAlAs/AlAs $\lambda/4$ layers, where λ is the cavity resonance wavelength (varying around the quantum well exciton resonance, ~768nm with tapering). Three stacks of four GaAs quantum wells are positioned at the central three antinodes of the microcavity photon field. The distributed Bragg reflectors (DBR) consist of repeated GaAlAs/AlAs layers. Multiple quantum well layers increase the total polariton density by a factor of $\sqrt{N}$ (N is the number of QW layers). Compared to the single QW layer, this allows us to get the same coupling strength with $1/\sqrt{N}$ density of polaritons per single QW layer. Because the bosonic property of excitons is only ensured at low density (in a QW layer), with multiple QW layers we can get the critical polariton density for condensation keeping the bosonic property of excitons (which also ensures the bosonic property of polaritons).

4.2 Implementation of the periodic potential

We implement the periodic potentials by depositing patterned thin metals on the semiconductor surface. Because the energy of polaritons under the metal is higher, potential walls are formed under the metal while the energy is locally lower where no metal is deposited. Fig. 4.1a shows a picture of the sample where we implement the square lattice, triangular lattice and honey-comb lattice potentials (fig. 4.1b, c, d). The diameter of traps and the distance between traps are kept the same ($a/2$), and

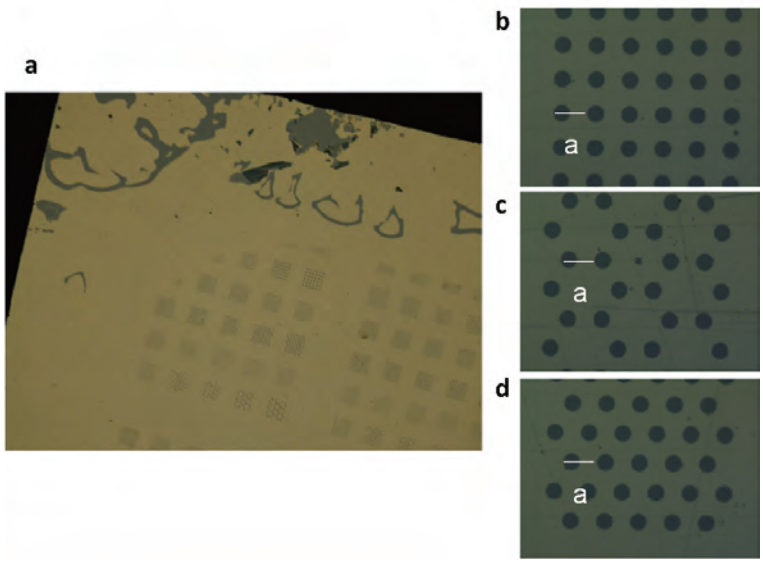

Figure 4.1: Pictures of fabricated sample. Lighter-colored areas correspond to areas where a thin metal is deposited, forming potential traps in the darker areas.

we use $a = 2and4\mu m$ lattice periods. For the fabrication, we use electron-beam (EB) lithography with a negative resist, depositing Ti(3nm)/Au(20nm) metal and perform a lift off procedure.

4.3 Detuning map

The wafer is grown on a rotating mount in a MBE chamber, so that the thickness of each layer varies slightly depending on the location on the wafer. Though this difference does not cause a significant energy shift of the QW excitons, the cavity

resonance is changed. Therefore we get a wide range of the detuning parameters in the wafer. In order to perform experiments, we need to know the detuning parameter for a given position. A detuning map needs to be performed before starting experiments. Fig. (4.2) shows our sample design. The bottom region is close to zero-detuning.

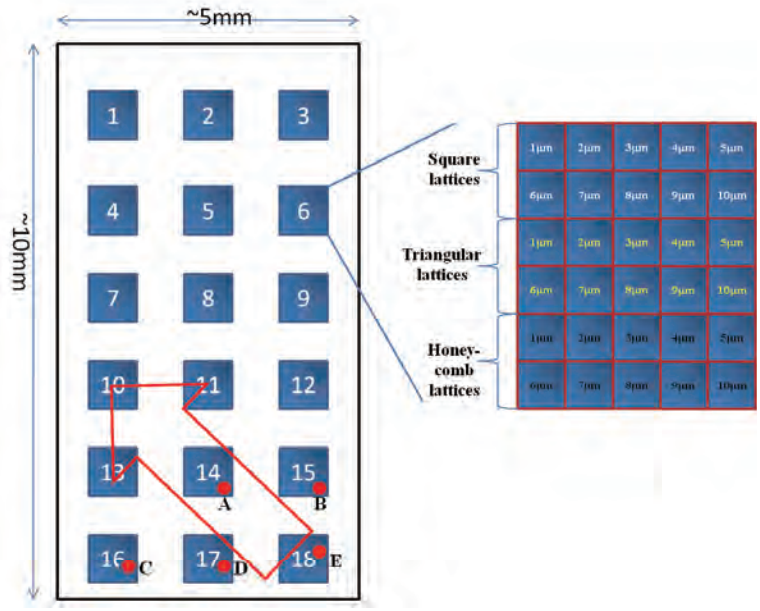

Figure 4.2: On a wafer of size 5mm-by-10mm, we fabricate 18 units of lattices. One unit consists of 30 lattices made of 10 square, 10 triangular and 10 honey-comb lattices. Each of those lattices have a period of 2,4,6...20μm.

To know the detailed detuning, we take the LP dispersion at five points (indicated 'A','B','C','D','E') and estimate the detuning by fitting the dispersion according to the following procedure. As we see in eq. (2.58), LPs have the dispersion relation of

$$E_{LP}(k_{\|}) = \frac{E_{ex} + E_{ph}(k_{\|})}{2} - \left[\hbar^2\mathcal{G}^2 + \frac{1}{4}(E_{ex} - E_{ph}(k_{\|}))^2\right]^{\frac{1}{2}}, \tag{4.1}$$

where we assume the exciton energy is constant because of its much heavier mass than photons. The dispersion relation of cavity photons is

$$E_{ph}(k_{\|}) = \frac{\hbar c}{n_c}\sqrt{k_{\|}^2 + k_z^2}, \tag{4.2}$$

where c is the speed of light, n_c is the refraction index of the cavity material and k_z is the wave number along the growth direction. The detuning is $\Delta = E_{ph}(k_{\|} = 0) - E_{ex}$, so that

$\Delta + E_{ex}(k_{\parallel} = 0) = \frac{\hbar c k_z}{n_c}$. We perform fitting of the LP dispersion with eq. (4.1) using eq. (4.2), where fitting parameters are $\mathcal{G}$, E_{ex} and Δ at each position. Fig. (4.3) shows the

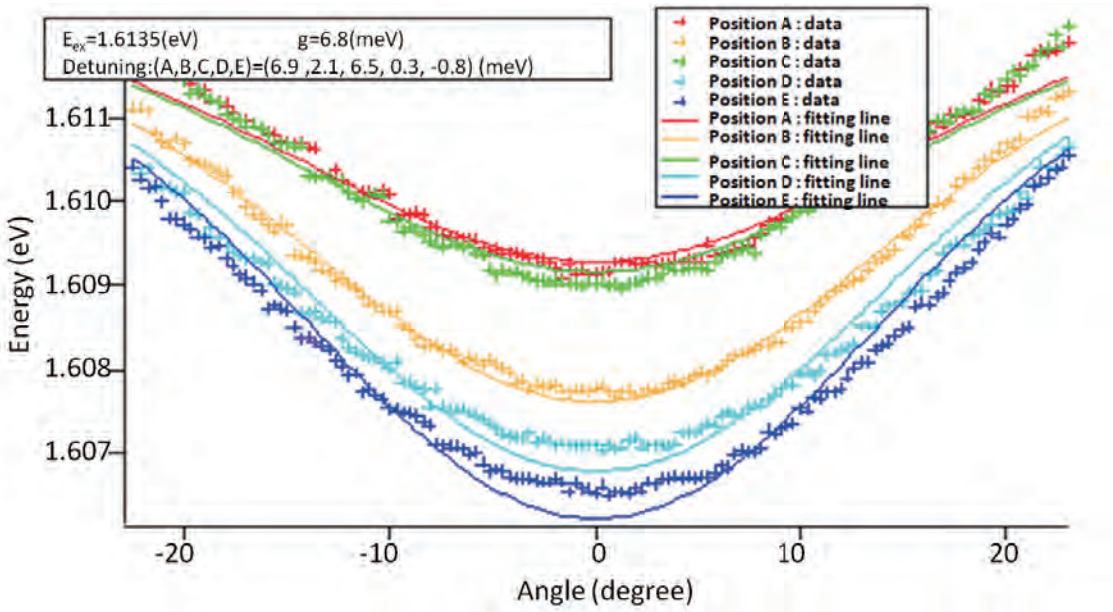

Figure 4.3: Measured LP dispersion at 'A', 'B', 'C', 'D', 'E' and those fitting curves are plotted. The vertical axis is energy, and the horizontal axis is the degree θ(which corresponds to the in-plane momentum). The degree and the in-plane momentum of LPs are connected in the relation of $k_{\parallel} = n_c \frac{2\pi}{\lambda_c} \tan\left(\sin^{-1}\left(\frac{\sin\theta}{n_c}\right)\right)$

LP dispersion at several points ('A'-'E' in fig. (4.2)) and the fitted curves. The deduced fitting parameters are shown in fig. (4.3). According to the result, unit '18' in fig. (4.2) is closest to zero-detuning, and the detuning is increasing along the red arrow.

4.4 Set-up of optics

Our experiments are performed at a temperature of 4K cooled with a liquid He in a cryostat. The emission from the sample is collected through an objective lens with NA$\sim$ 0.55, and transformed into Fourier plane and real plane by lenses so that we can get the polariton distribution in both planes by imaging on a CCD. The spectrometer resolves the energy of polaritons giving us the dispersion relation and the spatial energy information of the polaritons. A Michelson interferometer set up is used to measure

the first order spatial coherence and a coherence between polaritons with different momentum. Using a beam splitter, the emission is splitted into two arms, one of which is reflected by a mirror and the other is reflected by a prism. The two merge again and these are imaged on the CCD. The emission which is reflected in the prism is a slightly tilted and inversed. The angle puts an additional phase gradient on the image reflected by the prism, and makes interference fringes in the image on the CCD. By changing the position of the prism, we can also control the position of the overlap. The microcavity is excited by a mode-locked Ti:Sapphire laser with a ~2.5 ps pulse and a 76MHz repetition rate near the lower polariton resonance at an incident angle of 60°, corresponding to an in-plane wavenumber $k_{\|} < 7 \times 10^4 cm^{-1}$ in air. The large $k_{\|}$ of the pump ensures that the coherence of the pump laser is lost by multiple phonon emissions before the polaritons scatter into $k_{\|} < 0$ states.

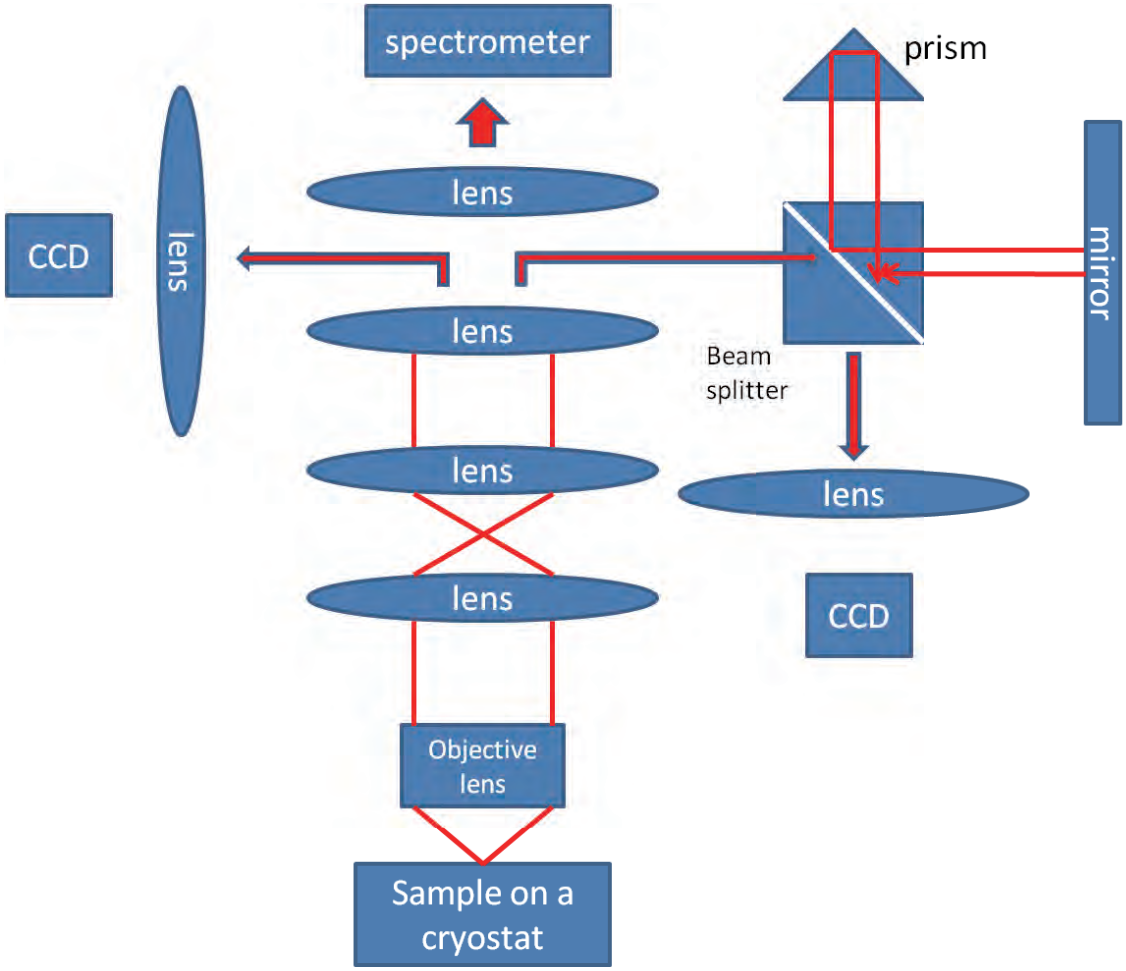

Figure 4.4: Schematic of the optical setup. In the center the main line is formed. The left consists of the imaging line, and the right shows the Michelson interferometer setup.

Chapter 5

Dynamical d-Wave Condensation of Exciton-Polaritons in a 2D Square Lattice Potential

5.1 A square lattice

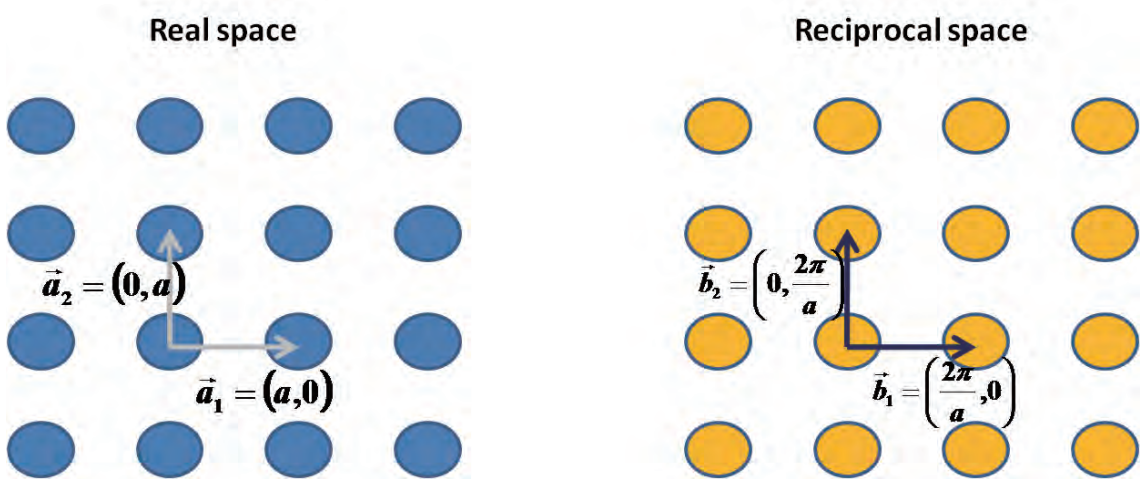

Figure 5.1: Schematic of a square lattice structure and its reciprocal lattice.

Fig. 5.1 shows a square lattice structure, which is one of the simplest two dimen-

sional structures, with the period a and unit vectors $\boldsymbol{a_1}$ and $\boldsymbol{a_2}$. A square lattice has rotational, translational and reflection symmetry. The reciprocal lattice is also a square lattice with period $\frac{2\pi}{a}$ and unit vectors $\boldsymbol{b_1}$ and $\boldsymbol{b_2}$ (fig. 5.1). The resulting BZs have the

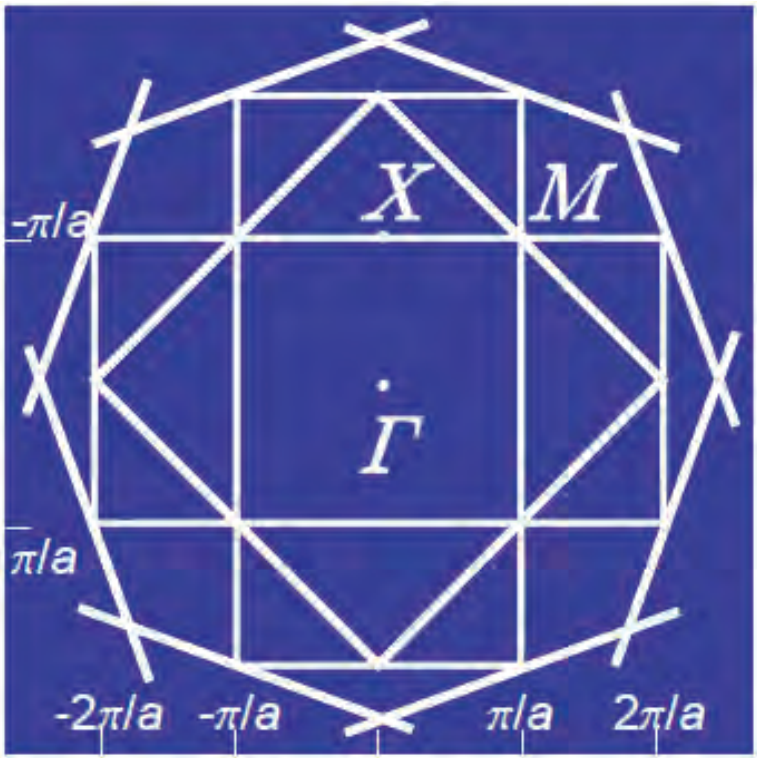

Figure 5.2: Theoretical Brillouin zones (BZs) of the 2D square lattice, displayed up to the fourth BZ.

form shown in fig. 5.2. Inside the first BZ there are three kinds of high symmetric points. The Γ-point lies at the center of the first BZ having four-fold degeneracy, the X-point has two-fold degeneracy, and the M-point has four-fold degeneracy.

5.1.1 Band structure

At the high symmetric points, the eigenstates can be classified according to their symmetry properties of the rotation group. At the Γ point, the lowest energy ground state exhibits non-degenerate 1s-wave symmetry, and the next excited (quartet) states

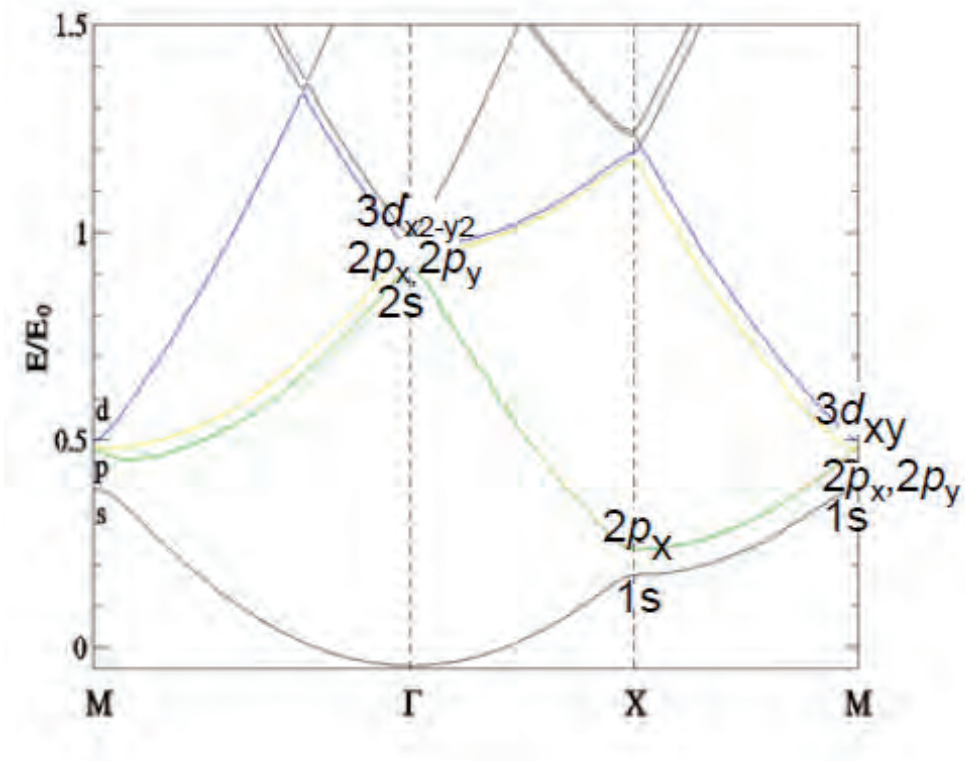

Figure 5.3: Calculated band structure for a square lattice in the non-interacting approximation. Here the potential depth of $U = 0.2E_0$ is used, where E_0 is defined as $E_0 = \frac{\hbar^2}{2m}\left(\frac{2\pi}{a}\right)^2$ with the lattice period a

.

are denoted by $3d_{x^2-y^2}$,$2p_x$,$2p_y$,$2s$-wave symmetries in real space. Equilibrium condensation takes place with a $1s$-wave symmetry at the Γ point. Similarly, the lowest energy (quartet) states at the M point are split into, $2p_x$, $2p_y$, $1s$-states for which the $3d_{xy}$-state is the only metastable state and thus it is expected that the dynamic condensation occurs with the $3d_{xy}$-wave symmetry at the M point. Finally, the lowest energy (doublet) states at the X point are $2p_x$ (or $2p_y$) and 1s- states, for which the $2p_x$ (or $2p_y$) is the only metastable state and a candidate for the dynamic condensation at the X point.

5.2 Dynamical meta-stable condensation in 2D Square Lattice Potentials

5.2.1 Detection of meta-stable condensation in the momentum space

We first show results for the 4μm period device near zero-detuning. Fig. 5.4 shows the observed far-field (FF) images, which means images in momentum $(k_{\parallel}^{x}, k_{\parallel}^{y})$ space, at various optical pump powers. Exciton-polaritons are injected at fixed wavenumber k_p indicated by the blue arrow in Fig. 5.4. Different momentum distributions of exciton-polaritons emerge with increasing injected particle density. Below the condensation threshold pump power ($P < P_{th} \sim 7$ mW), isotropic thermal LPs leak as photons at finite |k| values before they relax to the ground state at $(k_{\parallel}^{x}, k_{\parallel}^{y} \sim 0)$, yielding a donut-like emission pattern (bottleneck effect). Near the condensation threshold pump power $P \sim P_{th}$, the metastable $3d_{xy}$ state at the first M points, $(k_{\parallel}^{x}, k_{\parallel}^{y}) = (\pm\pi/a, \pm\pi/a)$, are selectively occupied in accordance to the expectations as described in section 5.1. The injected exciton-polaritons with much larger momentum than that of measured LPs relax and dynamically condense at M points. With a increasing the pump power, the momentum spread Δk at M point dramatically decreases, which suggests phase order is formed over a macroscopic distance $\sim$ 40 nm. With further increase of the pump power, the condensation in the metastable $2p_x$ (p_y) state at X point and finally condensation in the 1s ground state at Γ point is observed.

5.2.2 Energy spectroscopy

In order to quantify the energy eigenvalues of the three orbital states, we perform a spectroscopic measurement of the energy-momentum dispersion relation by selecting a particular cross-section in momentum space (Fig. 5.5,5.6). Selected cross-sections along the lines indicated by diagonal lines with numbers 1 and 2 are shown in Fig. 5.5. The 1s- and $3d_{xy}$-orbitals are observed along the line 1, while only the $3d_{xy}$-orbital is observed along the line 2. From the pump-power dependence of the observed energy-momentum dispersion curves, we extract two quantities: the energies and the 2D in-plane wave numbers of the individual orbital states. Along line 1, the distance of two prominent peaks ($3d_{xy}$-orbital states) corresponds to the diagonal length of the first BZ ($2\pi\sqrt{2}/a$), and the energy of these states are $E_{3d_{xy}}(M) \sim 1610.55$ meV near the threshold pump, $P_{th,d} = 7mW$ (fig. 5.6). The 1s ground state energy at $(k_{\parallel}^{x}, k_{\parallel}^{y}) =$

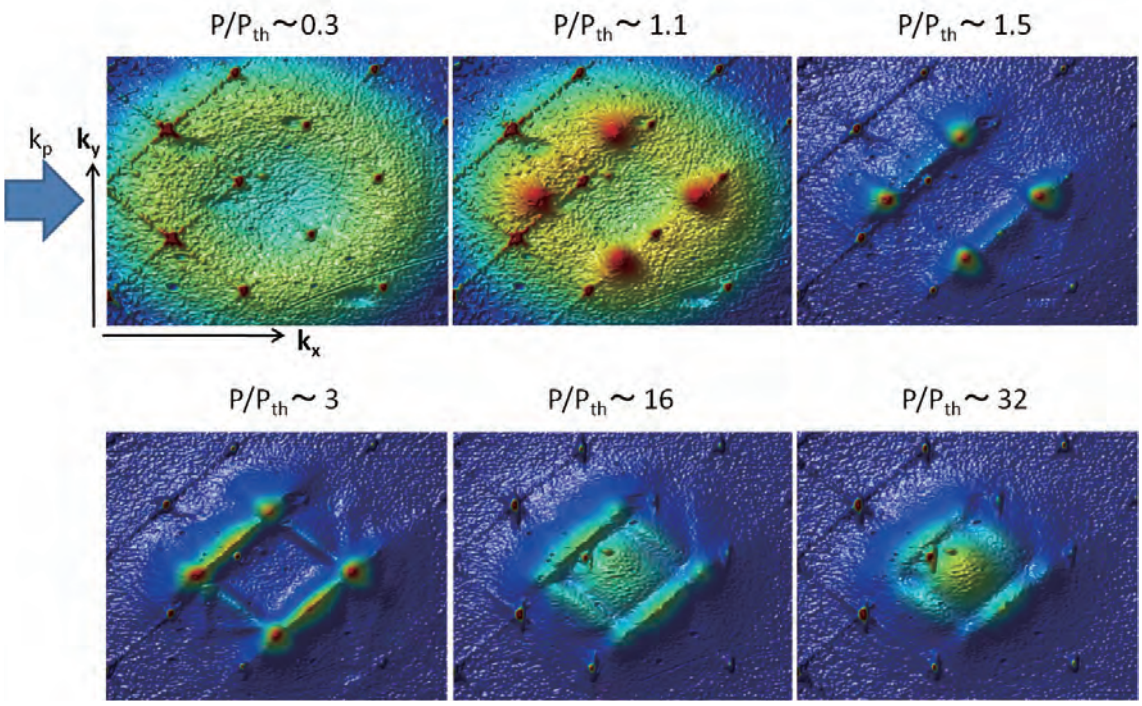

Figure 5.4: Measured far-field images from a 4μm period device. P_{th} is the threshold pump power which is about 6meV. This data is taken with the sample 45 degrees rotated against the configuration shown in fig. 5.1. The sharp peaks which is seen in all figures are the diffraction peaks of the reflected laser.

(0,0) is E(0) ~ 1608.93 meV below the condensation threshold, but this s-orbital state condenses at $E_s(0)$ ~ 1609.83 meV at $P_{th,s}$ = 10mW. The energy blue shift (~ 0.9 meV) is due to the repulsive polariton-polariton interactions. The $E_{3d_{xy}}$(M) at the line 2 is identical to that of the $3d_{xy}$ state along the line 1 (Fig. 5.6a) as expected. Near threshold pump power, the energy eigenvalues of the 1s-state at Γ point, $2p_x$-state at the X points, $3d_{xy}$-states at the M points are equally spaced by 0.36 meV, which is compatible to the theoretically expected energy spacing ~ 0.26 meV within experimental error. At higher pump powers, LPs in high-orbital states further condense into smaller $k_{||}$-valued states. Fig. 5.6b shows some representative data at P ~ 50 mW ~ 7 P_{th}.

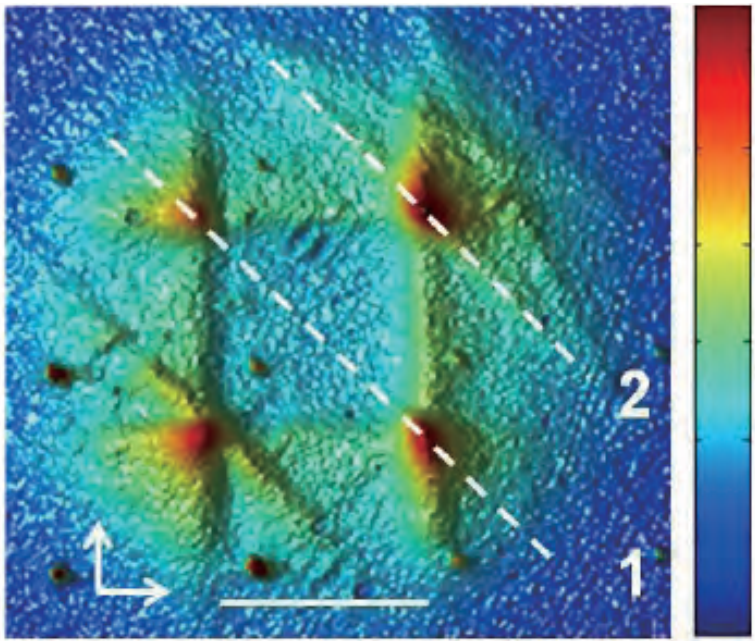

Figure 5.5: The emission from polaritons are input to the spectrometer along two slices (line 1, 2) as shown in the far-field spectrum.

5.2.3 Theoretical single particle wave functions

The FF interference patterns are manifestations of the relative phase between the real space Bloch wavefunctions of the orbital symmetry. We compute the real space wavefunctions (near-field (NF) images) configurations and the momentum distribution (FF images). Figure 5.7 a-c show the case of a strong parabolic trap potential in a 3-by-3 lattice site, where real-space wavefunctions are tightly localized at each site, which clearly show the near-field orbital symmetry. The 1s ground state is stable at the Γ point, the metastable $2p_x$-states appear at the X points, and the metastable $3d_{xy}$-states occur at the M points. The anti-phased $3d_{xy}$-orbital symmetry between nearest neighbour sites is the reason for the intensity peaks at M point in the momentum space as shown in Fig. 5.7c. Similarly, the anti-phased $2p_x$-states are responsible for the intensity peaks at the X points shown in Fig. 5.7b. On the other hand, the conventional in-phased 1s-orbital condensate produces an intensity peak at the Γ point as shown in Fig. 5.7a. In the experimental results shown in Fig. 5.4a, the interference patterns created by the 1s and $2p_x$-orbitals are broader in momentum space compared to that created by the $3d_{xy}$-orbitals. This feature implies that the 1s and $2p_x$-orbitals are less coherent that

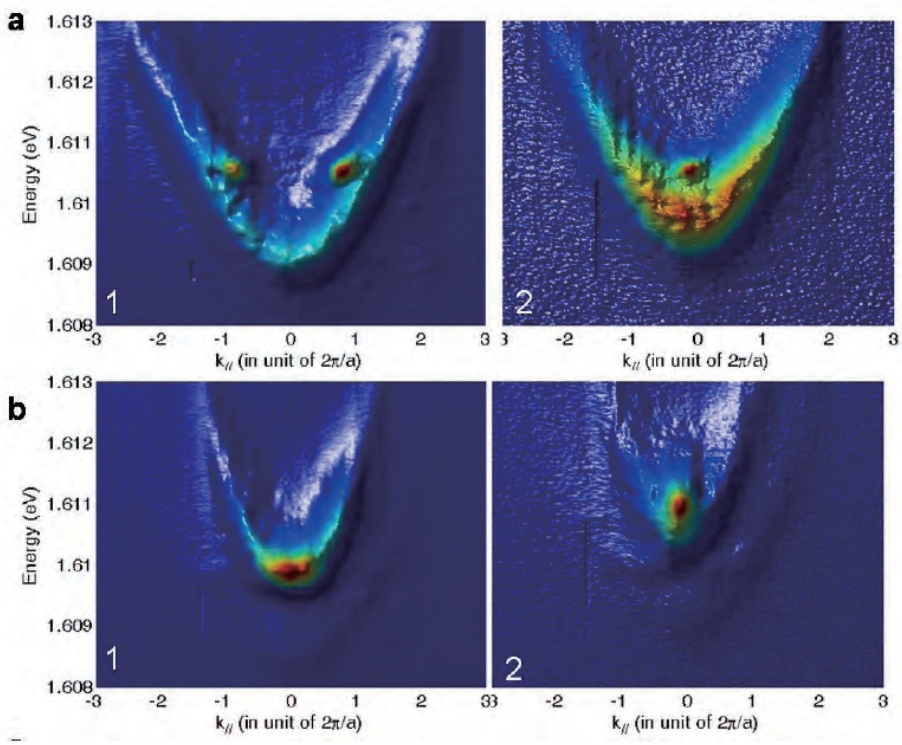

Figure 5.6: Measured polaritons dispersions are shown with different pump and along two lines (fig. 5.5). (a) just above the threshold pump power, (b) well above the threshold pump power.

the $3d_{xy}$-orbitals in real space. An explanation of this is due to the larger tunnelling coupling between sites for the $3d_{xy}$-state, giving a larger spatial coheernce.

Fig. 5.8 shows the calculated NF wave functions of the above three cases by the band structure calculation, using the plane wave approximation. We see the wavefunctions localized on a site same as in the above strong potentials case. On one site, the 1s-state at the Γ-point is completely symmetric. The $2p_x$-state at the X-point is symmetric with respect to the x-axis and anti-symmetric with respect to the y-axis. The $3d_{xy}$-state at the M-point is symmetric with respect to the lines along vectors (x,y)=(1,1) and (1,-1), and anti-symmetric with respect to x and y-axis.

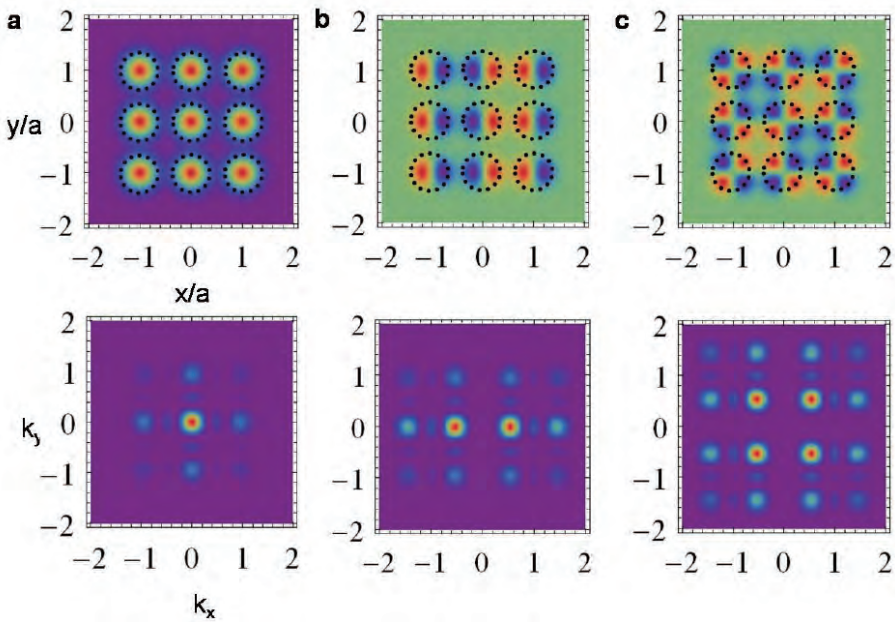

Figure 5.7: Calculated NF (upper row) and FF (lower row) images for strong confinement potentials. In NF images, colors display the phase of the wave function. Namely, 'red' shows the region with positive values of the wave function, while 'blue' does negative values. (a) 1*s*-orbital, (b) $2p_x$-orbital, and (c) $3d_{xy}$-orbital condensation.

5.3 Dynamical d-Wave Condensation of Exciton-Polaritons in a 2D Square Lattice Potential

As wee saw above, meta-stable condensation at the M-points on the boundary of the first BZ has single site symmetry like an atomic *d* state. This is the first demonstration of a *d*-wave orbital condensate of EPs. We explore their properties of that in this section.

5.3.1 Spatially resolved spectroscopy

As is shown above, the 1s-state and $3d_{xy}$ have different positions in their intensity peaks. We explore the spatial distribution of the $3d_{xy}$ state in comparison with the 1s-state. At $P/P_{th} \sim 3.6$, all three orbital condensates coexist with different emission intensity, but the $3d_{xy}$ -orbital and p-orbital condensates dominate (fig. 5.4). On the other hand, 1s -orbital condensate dominates for $P/P_{th} \sim 29$ (fig. 5.4). The positions

of the stronger emissions at $P/P_{th} \sim 3.6$ and at $P/P_{th} \sim 29$ differ by a half period of the lattice constant. Since both $2p_x$ (p_y) and $3d_{xy}$ - orbital emissions are more intense than the 1s -orbital emission at $P/P_{th} \sim 3.6$, nodes with minimum intensity are at the center of the aperture, while the opposite is true at $P/P_{th} \sim 29$. Fig. 5.9 (c-f) shows the spatially resolved spectroscopy at several pump powers. There we see regions where the $3d_{xy}$-state is dominant (fig. 5.9d) and regions where the 1s-state is dominant (fig. 5.9f). The cross-section along the red line in fig. 5.9 (a,b) at two energy (1s and $3d_{xy}$) show anti-correlated emission profile in real space (fig. 5.10), which is consistent with theoretical calculation (fig. 5.7, 5.8).

5.3.2 Coherence among four M-points

Phase coherence of the $3d_{xy}$-orbital condensate is further confirmed by a Michelson interferometry constructed in momentum space. We place a simple mirror and a right angle prism at each arm of the Michelson interferometer in order to fold the FF images with respect to the center line (fig. 4.4). Figure 5.11 shows that the interference fringes indeed exist at the M points near $P \sim P_{th}$. This result rules out the independent condensation at the four M points (condensate fragmentation in momentum space) but supports our previous discussion that the dynamic condensation takes place with anti-phased $3d_{xy}$-wave symmetry over many sites.

5.3.3 Rate equation analysis

We model this system by four coupled rate equations in the particle number in the pump reservoir n_p, for the condensates n_M at M-points, the condensates n_X at X-points, and the condensates n_Γ of the ground state. We assume LPs only decay into lower energy states, with a scattering rate Γ_{ij} when LPs decay from state 'i' to 'j'. LPs also decay out of the system with radiative decay rate Γ_i from state 'i'.

$$\begin{aligned}
\frac{dn_p(t)}{dt} &= -\Gamma_p n_p - \Gamma_{pM} n_p(n_M+1) - \Gamma_{pX} n_p(n_X+1) - \Gamma_{p\Gamma} n_p(n_\Gamma+1) \\
\frac{dn_M(t)}{dt} &= -\Gamma_M n_M + \Gamma_{pM} n_p(n_M+1) - \Gamma_{MX} n_M(n_X+1) - \Gamma_{M\Gamma} n_M(n_\Gamma+1) \\
\frac{dn_X(t)}{dt} &= -\Gamma_X n_X + \Gamma_{pX} n_p(n_X+1) + \Gamma_{MX} n_M(n_X+1) - \Gamma_{X\Gamma} n_X(n_\Gamma+1) \\
\frac{dn_\Gamma(t)}{dt} &= -\Gamma_\Gamma n_\Gamma + \Gamma_{p\Gamma} n_p(n_\Gamma+1) + \Gamma_{M\Gamma} n_M(n_\Gamma+1) + \Gamma_{X\Gamma} n_X(n_\Gamma+1) \qquad (5.1)
\end{aligned}$$

From the phenomenological behaviour measured in experiments, we choose the following numerical values for the decay rate and the transition rates: $\Gamma_p = 1/300(ps^{-1}), \Gamma_M = 1/10(ps^{-1}), \Gamma_X = 1/10(ps^{-1}), \Gamma_\Gamma = 1/5(ps^{-1}), \Gamma_{pM} = 1/20(ps^{-1}), \Gamma_{pX} = 1/100(ps^{-1}), \Gamma_{p\Gamma} = 1/100(ps^{-1}), \Gamma_{MX} = 1/20(ps^{-1}), \Gamma_{M\Gamma} = 1/100(ps^{-1}), and \Gamma_{X\Gamma} = 1/40(ps^{-1})$. Fig. 5.12 shows the mode competition against pump power evolution. The above rate equations follow the qualitative signature of the mode competition.

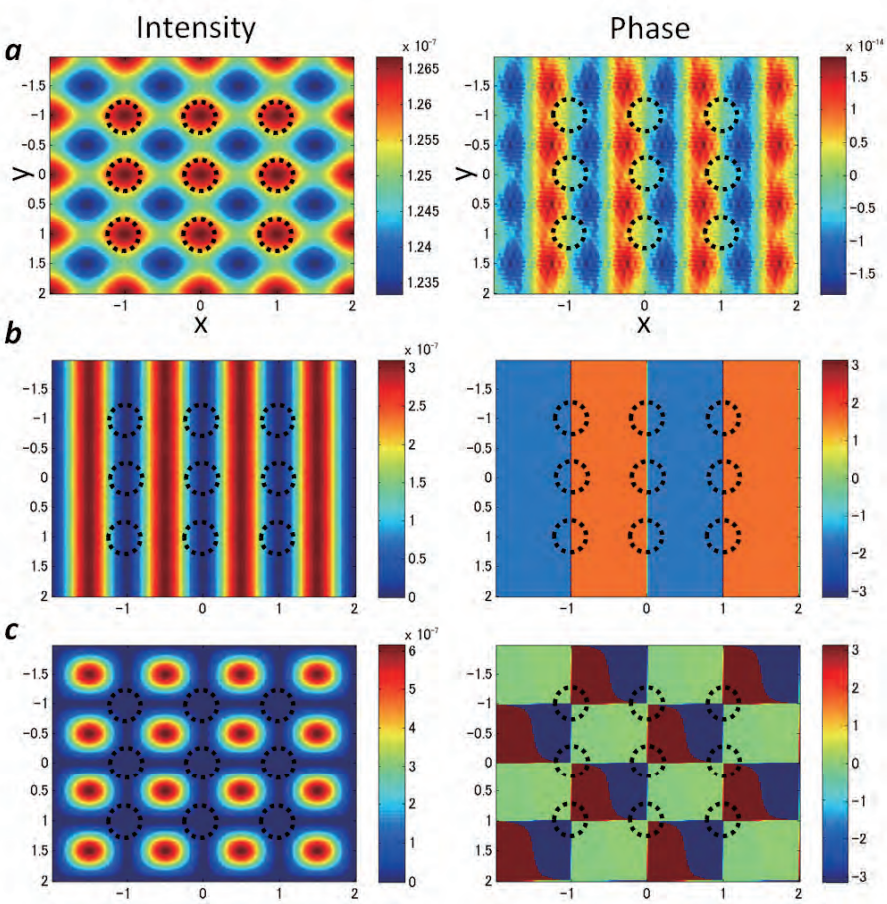

Figure 5.8: Calculated NF images by a band structure calculation, corresponding to weak potential case. Black circles indicate the potentials trap. (a) 1s-orbital, (b) 2p_x-orbital, and (c) 3d_{xy}-orbital condensation.

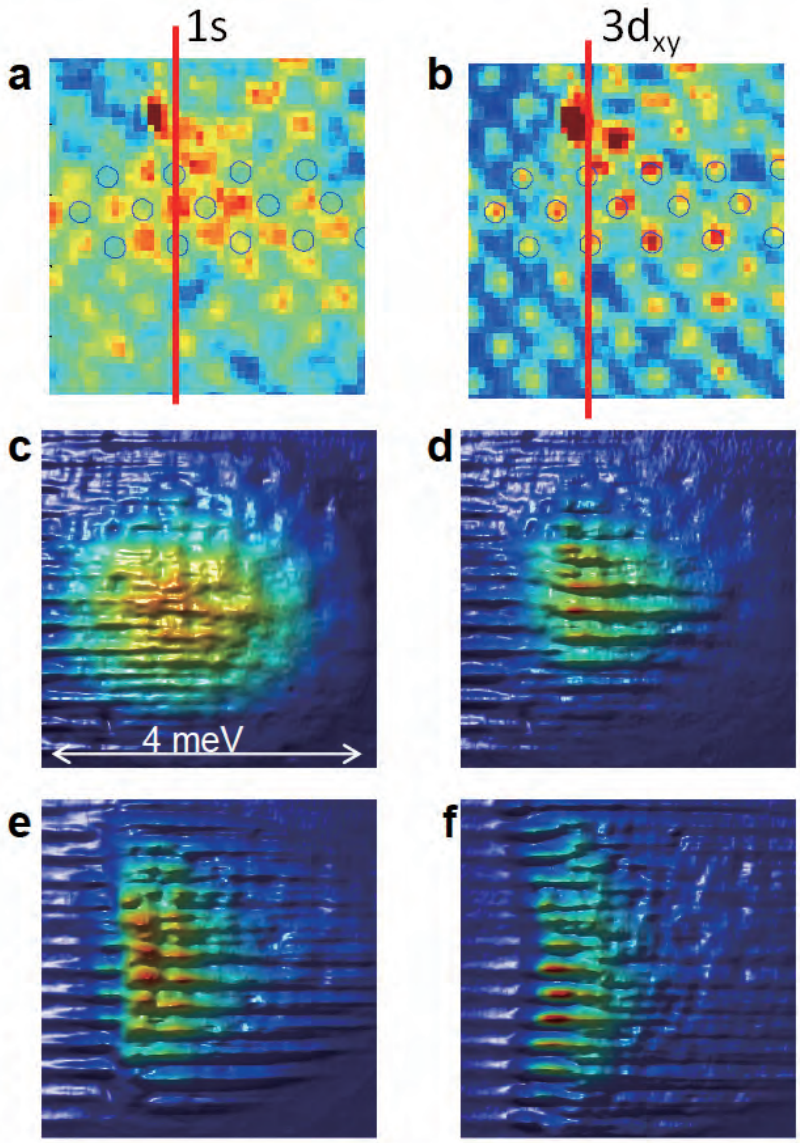

Figure 5.9: (a,b) Near-field Images at two pump rates, $P/P_{th} \sim 3.6$ (a) and ~29 (b). Both axes are real coordinate. The circles indicate the aperture locations at the metal film pattern. (c-f) Near-field spectroscopy along the red line in (a) or (b) at $P/P_{th} \sim 0.29$, 1, 2.9, and 14. The horizontal axis is energy of polaritons (righter is higher), and the vertical axis is the real coordinate.

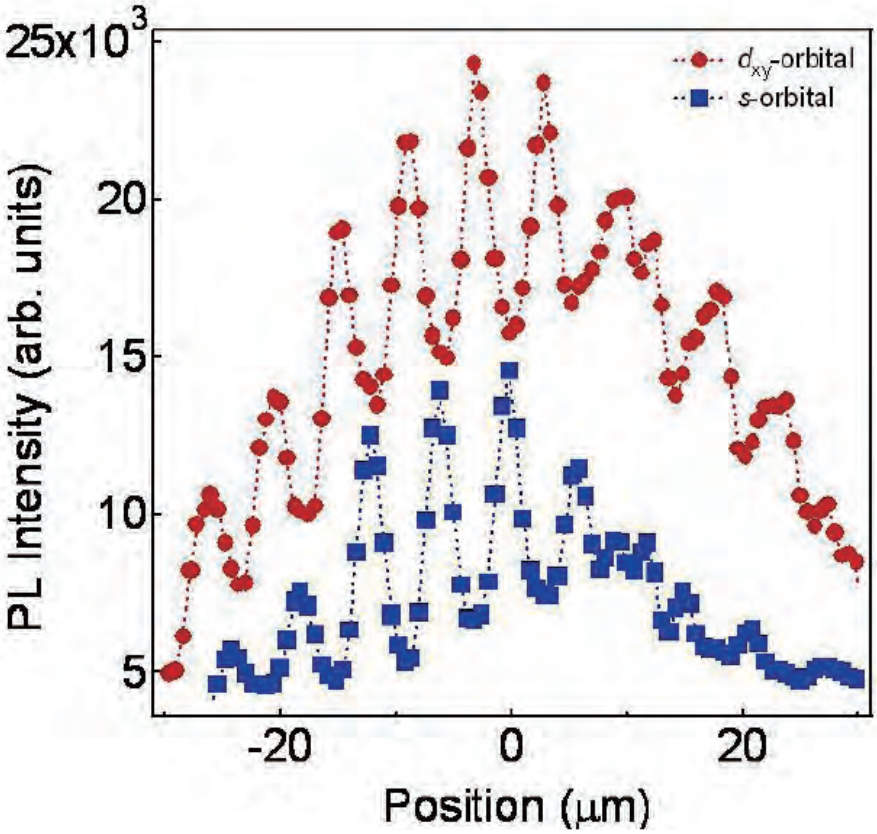

Figure 5.10: Near field emission of 1s and $3d_{xy}$ states.

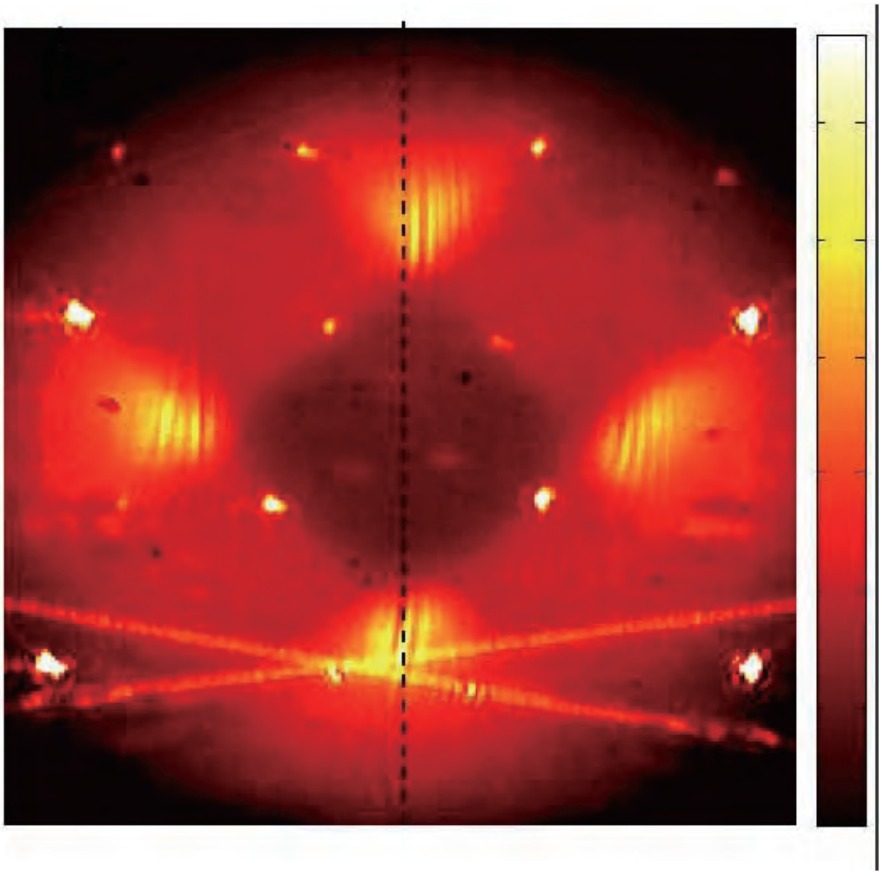

Figure 5.11: Coherence among the four M-points, taken by Michelson interferometry.

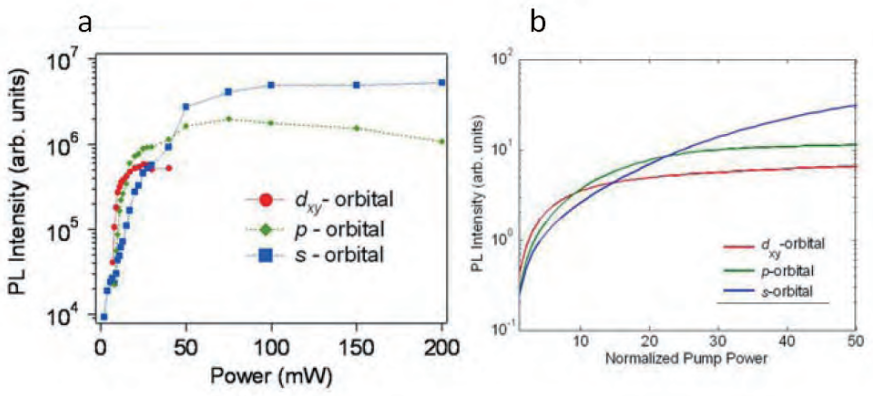

Figure 5.12: Mode competition between various orbital states. (a) measured, (b) calculated with the rate equation in eq. (5.1).

Chapter 6

Formation of A Metastable Vortex-antivortex Order in Honey-comb Lattice Potential

6.1 A honey-comb lattice

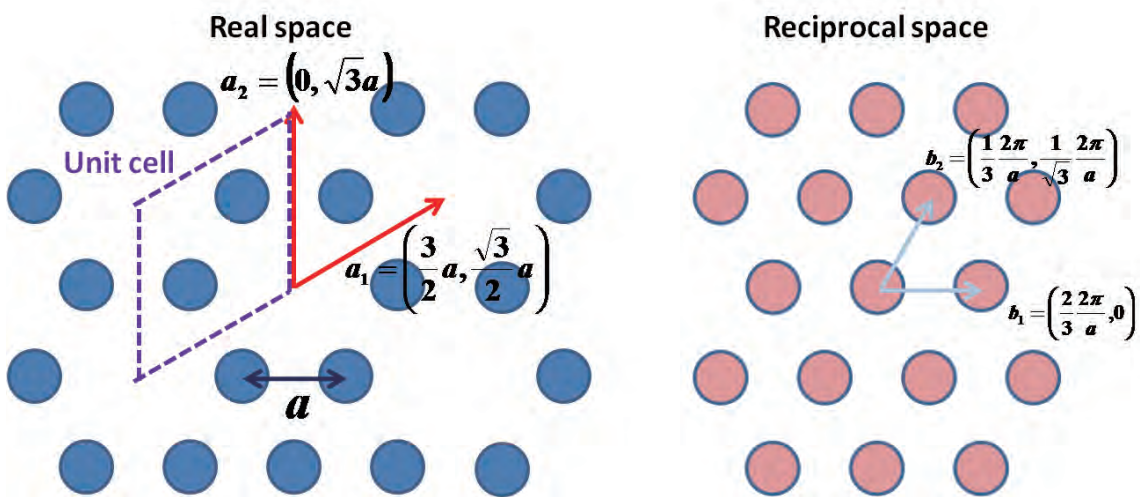

Figure 6.1: A schematic of a honey-comb lattice structure and its reciprocal lattice.

Fig. 6.1 shows a honey-comb lattice structure. This structure has recently gathered a

large amount of attention since this is the crystal structure graphene [52] [53]. Although the honey-comb lattice is also a kind of the triangular lattice, there are two lattice points in an unit cell indicated by purple dotted lines in fig. 6.1. It has a six-fold rotational symmetry, reflection symmetry, and translational symmetry. The two unit vectors of the honey-comb lattice with the period a can be written $\boldsymbol{a_1} = (\frac{3}{2}a, \frac{\sqrt{3}}{2}a)$ and $\boldsymbol{a_2} = (0, \sqrt{3}a)$. The reciprocal lattice is also a honey-comb lattice with period $\frac{2}{3}\frac{2\pi}{a}$. The unit vectors in the reciprocal lattice are $\boldsymbol{b_1} = (\frac{2}{3}\frac{2\pi}{a}, 0)$ and $\boldsymbol{b_2} = (\frac{1}{3}\frac{2\pi}{a}, \frac{1}{\sqrt{3}}\frac{2\pi}{a})$ (fig. 6.1). The resulting

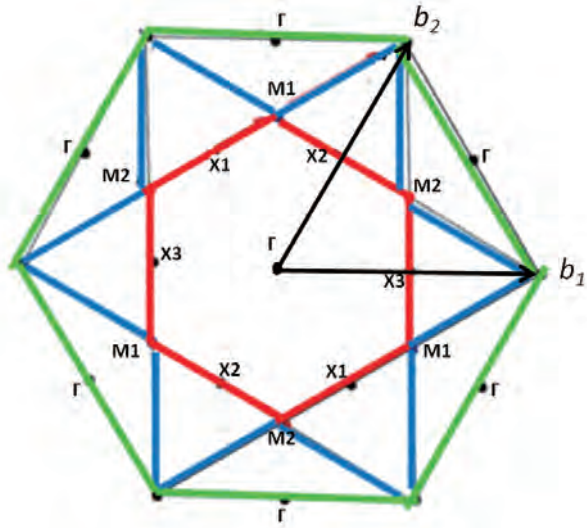

Figure 6.2: Theoretical Brillouin zones of the 2D honey-comb lattice. Red lines indicate the boundary of the first BZ, and blues do the boundary of the second while greens do that of the third BZ. The second Γs on the honey-comb corners of the green lines are connected to the center Γ by the unit vectors in the reciprocal space, as illustrated by $\boldsymbol{b_1}$ and $\boldsymbol{b_2}$.

Brillouin zones have the form shown in fig. 6.2, where inside the first BZ there are three kinds of symmetric points. The Γ-point lies at the center of the first BZ with a six-fold symmetry, the X-point has a two-fold symmetry, and the M-point has a three-fold symmetry.

6.1.1 Band structure

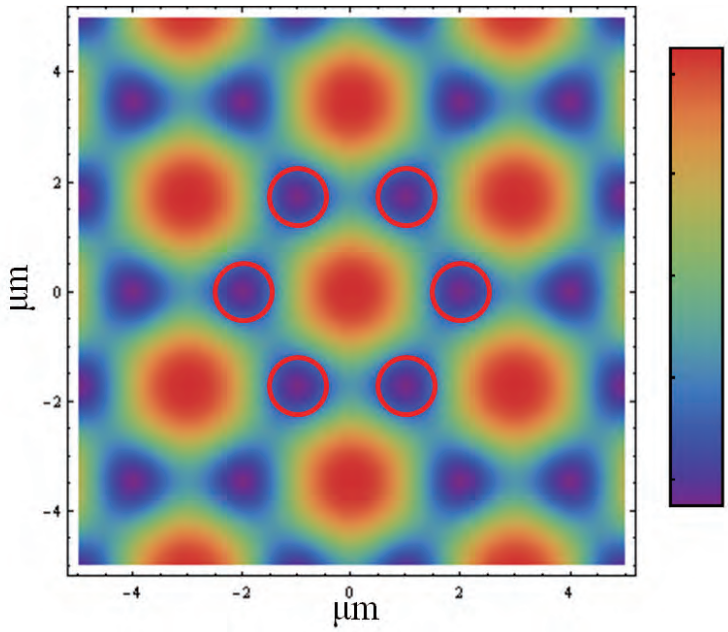

Figure 6.3: Approximate honey-comb lattice potentials for band calculation. Red circles indicates some trap positions.

To calculate the band structure, we approximate the honey-comb lattice potentials by $V(\mathbf{r}) = V_0\,(\cos(\mathbf{k_1}\cdot\mathbf{r}) + \cos(\mathbf{k_2}\cdot\mathbf{r}) + \cos(\mathbf{k_3}\cdot\mathbf{r})) + \frac{1}{4}V_0\,(\cos(\mathbf{l_1}\cdot\mathbf{r}) + \cos(\mathbf{l_2}\cdot\mathbf{r}) + \cos(\mathbf{l_3}\cdot\mathbf{r}))$ (fig. 6.3), where $\mathbf{k_1} = (\frac{2}{3}\frac{2\pi}{a}, 0)$, $\mathbf{k_2} = (-\frac{1}{3}\frac{2\pi}{a}, \frac{1}{\sqrt{3}}\frac{2\pi}{a})$, $\mathbf{k_3} = (-\frac{1}{3}\frac{2\pi}{a}, -\frac{1}{\sqrt{3}}\frac{2\pi}{a})$, $\mathbf{l_1} = (0, \frac{2}{\sqrt{3}}\frac{2\pi}{a})$, $\mathbf{l_2} = (1, -\frac{1}{\sqrt{3}}\frac{2\pi}{a})$, and $\mathbf{l_3} = (-1, -\frac{1}{\sqrt{3}}\frac{2\pi}{a})$. Such that 200$\mu$eV potential barriers are present between potential traps, we set $V_0 = 100\mu eV$. We set the grand state energy to be 0. Fig. 6.4 shows the calculated band structure for a weak honey-comb lattice potential. At the high symmetric points, the eigenstates can be classified according to their symmetry property of the rotation group. At the Γ-point, the lowest energy ground state exhibits a non-degenerate 1s-wave symmetry on each site. The X-point has a two-fold degeneracy, though there are not meta-stable states here (the energy of the second band at the X-points is higher than the energy at M-points.). We note that this energy relation depends not on the lattice symmetry but on the potential strength. At other potential strengths, ti is possible for meta-stability to occur at X-points. At the M-point, we see two degenerate states and one higher energy state at M-points. This is in contrast to the triangular lattice

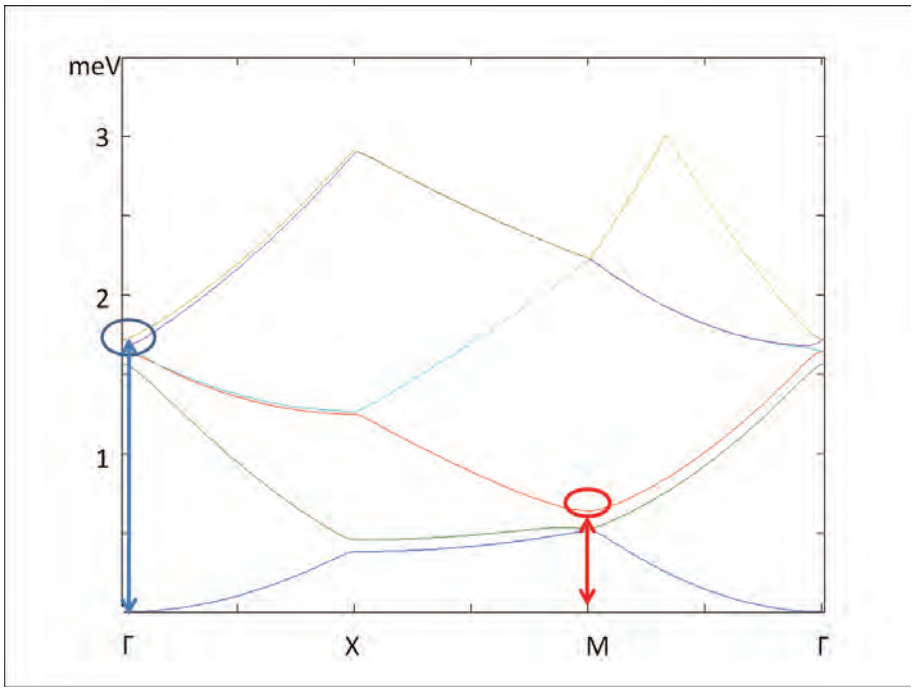

Figure 6.4: Calculated band structure for a honey-comb lattice by plane waves approximation. Here the potential depth is set to get $200\mu eV$ potential walls between potential traps.

case. This is reasonable because the approximate potential for the honey-comb lattice V_{HC} has the form of $V_{HC} = -V_{TR}$, where V_{TR} is the approximated potential for the triangular lattice potential. The higher band (the third band) at the M-point is meta-stable due to the band gap, and has a wavefunction of the form of a vortex-antivortex lattice (fig. 6.5). The meta-stable states at the M-points and the second Γ-points are marked by a red and a blue circle respectively (fig. 6.4). The relative energy of these state (compared to the ground state) are 0.8382 and $1.725meV$. The experimentally detected energy difference of three condensates are $E_{2nd\Gamma}(22mW) - E_{1st\Gamma}(200mW) \sim 2meV$ and $E_M(22mW) - E_{1st\Gamma}(200mW) \sim 1.4meV$. The difference between calculations and experiments are due to the energy blue shift by the repulsive interaction.

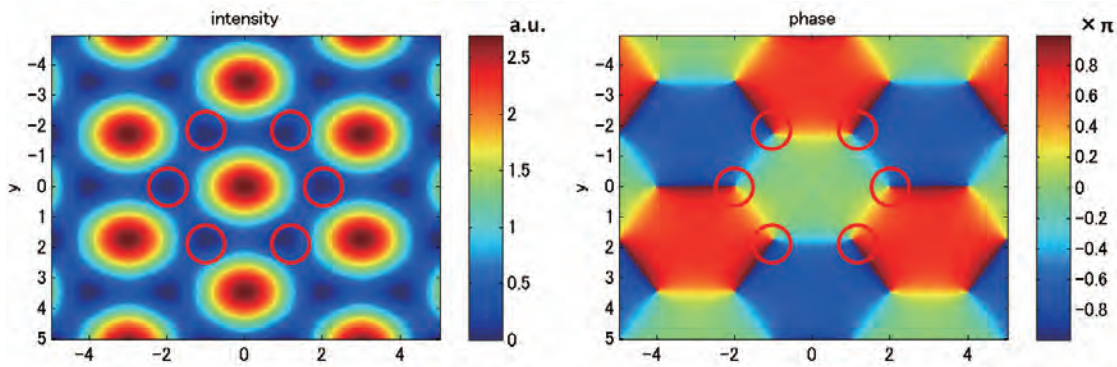

Figure 6.5: The calculated wavefunction of the meta-stable state at M-points, which has the form of the vortex-antivortex structure.

6.2 Results

Fig. 6.6 shows FF images of LPs for honey-comb lattice potentials. Below threshold, polaritons populate the bottle-neck region (fig. 6.6a). Here the hexagon at the boundary of the third BZ has almost the same size as the bottle neck region in momentum space. Therefore the meta-stable condensation at the second Γ-point first appears (fig. 6.6b). Increasing the pump power, LPs decay into lower energy states (fig. 6.6c) and meta-stable condensation occurs at the M-points next (fig. 6.6d) and finally at the central Γ point (fig. 6.6e,f). We take the LP dispersion along three lines shown in fig. 6.7, and to confirm the condensation. Along line '1', below threshold a usual particle like dispersion of LPs are seen (fig. 6.8a), while above threshold condensation at the M-points can be seen (fig. 6.8b). Well above threshold most of LPs collect in the Γ-points and condense (fig. 6.8c). Along line '1', M-points are located at $k_y = \pm\frac{2}{3\sqrt{3}}k_0 \sim 0.4k_0$. Because the meta-stable condensation occurs not at the top of the first BZ band but at the bottom of the higher BZ band, emission from M-point meta-stable condensation is located at $|k_y| \geq \frac{2}{3\sqrt{3}}k_0 \sim 0.4k_0$ region. Along line '2', below threshold a usual particle like dispersion of LPs is seen (fig. 6.8d), while above the threshold condensation at the second Γ-points (located at $k_y \sim \frac{1}{\sqrt{3}}k_0$) and at the M-points (at $k_y \sim \frac{1}{3\sqrt{3}}k_0$) can be seen (fig. 6.8e). A long line '3', the second Γ-point is located at $k_y = 0$ and above the threshold we see condensation occurs at that point. Fig. 6.9 shows the pump power dependence of the energy and the intensity for meta-stable condensation at the M-points and the second Γ-points. First we note that in both cases the typical behavior for condensation is seen, such as a nonlinear intensity jump and an energy blue shift at the threshold

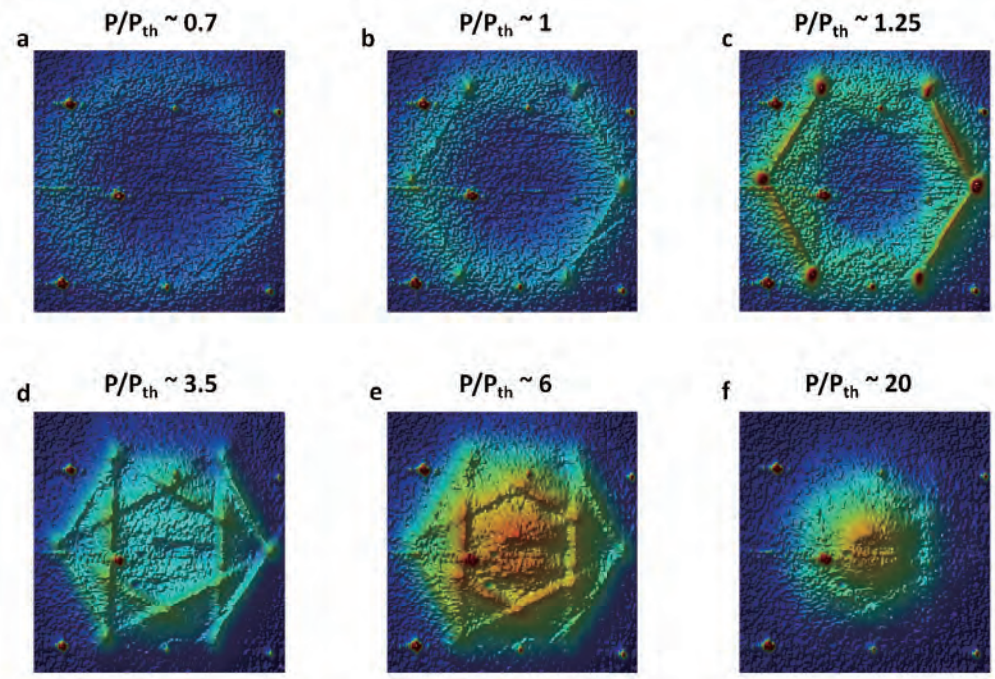

Figure 6.6: FF images of a $2\mu m$ device at several pump power. P_{th} is the threshold pump power.

pump power. A small difference in the intensity on (d) is due to imperfections of slicing to prior to the feed to the spectrometer. We also note that within the linewidth all M-points (all second Γ-points) have the same energy, and then they are degenerate.

6.3 Meta-stable condensation at the M-point

We focus on the meta-stable condensation at the M-point. According to the band calculation in fig. 6.4, at the M-point, the meta-stability only occurs at the third band. The wave function of this state also has a vortex-antivortex form as shown in fig. 6.5. This state can be written in the form:

$$|\Psi^M_{HC}\rangle = \frac{1}{\sqrt{3}}\left(|\Psi^M_A\rangle + |\Psi^M_B\rangle + |\Psi^M_C\rangle\right) \tag{6.1}$$

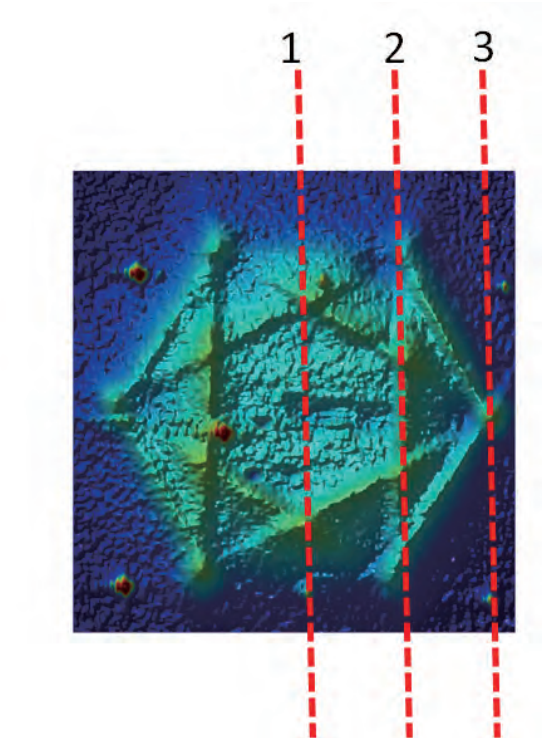

Figure 6.7: FF iamge showing direction of dispersion shown in fig. 6.8 of '1' includes the M-points, '2' includes the second Γ-points and the M-points, and '3' includes the second Γ.

with

$$
\begin{aligned}
|\Psi_A^M\rangle &= \frac{1}{\sqrt{V}}\exp(i\mathbf{k_{MA}}\cdot\mathbf{r}) \\
|\Psi_A^M\rangle &= \frac{1}{\sqrt{V}}\exp(i\mathbf{k_{MB}}\cdot\mathbf{r}) \\
|\Psi_A^M\rangle &= \frac{1}{\sqrt{V}}\exp(i\mathbf{k_{MC}}\cdot\mathbf{r}),
\end{aligned}
\tag{6.2}
$$

where $\mathbf{k_{MA}} = (0, \frac{2}{3\sqrt{3}}\frac{2\pi}{a})$, $\mathbf{k_{MB}} = (\frac{1}{3}\frac{2\pi}{a}, -\frac{1}{3\sqrt{3}}\frac{2\pi}{a})$, and $\mathbf{k_{MC}} = (-\frac{1}{3}\frac{2\pi}{a}, -\frac{1}{3\sqrt{3}}\frac{2\pi}{a})$, corresponding to the three M1-points. As is expected, we observe coherence between the M-points in the same group (in fig. (6.10)). This is because three M1-points are coherently connected to form the state of eq. (6.2).

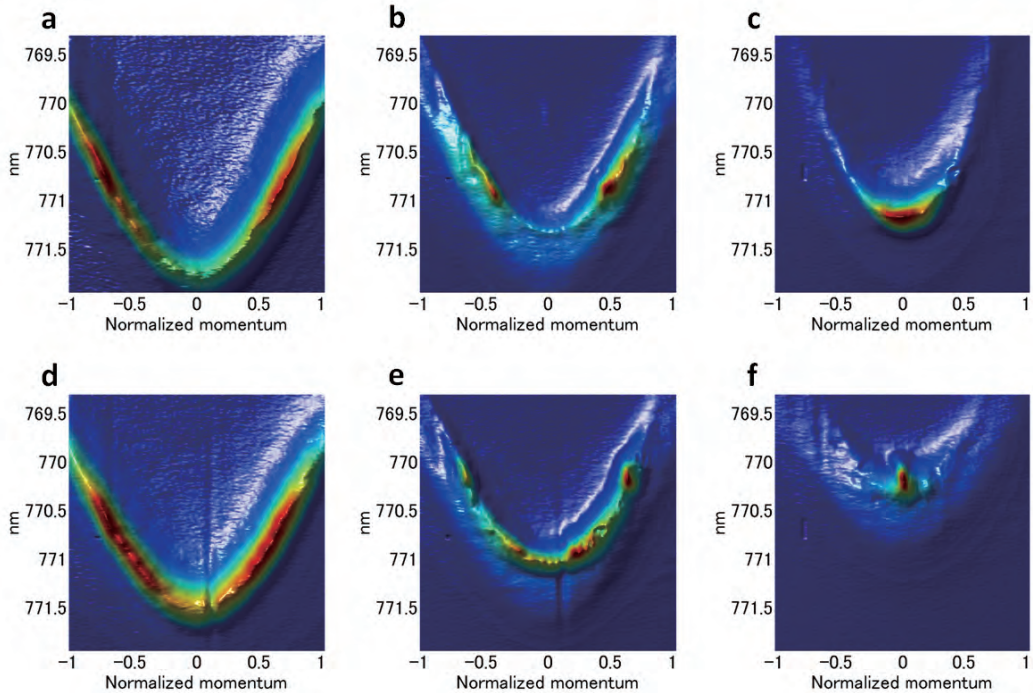

Figure 6.8: LP dispersions. Along line '1', (a) below threshold, (b) above threshold , and (c) well above threshold. Along line '2', (d) below threshold, and (e) above threshold (e). Along line '3', (f) above threshold. The horizontal axis is the in-plane momentum k_y normalized by $\frac{2\pi}{a}$, and the vertical axis is the LP energy represented by the wave length of the emitted photons.

6.4 Conclusion

In the honey-comb lattice potentials, we have observed the evidence for a vortex-antivortex lattice order. In this case, at the M-points, the meta-stability occurs at only the third band whose Bloch wave-function has a vortex-antivortex lattice order. We have confirmed that the three M-points in the M1 (M2) group are degenerate and coherently connected through the spectroscopy and Michelson interferometry.

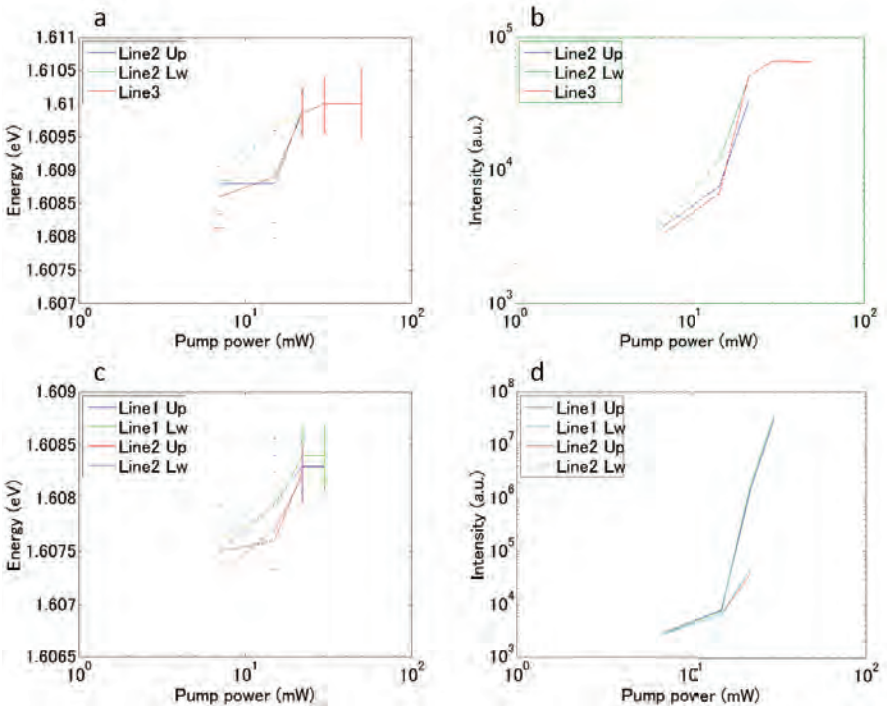

Figure 6.9: Comparison of the energy and the emission intensity of each M-point and second Γ-point. The finite linewidth of emission is shown as a error-bar. The upper two figures correspond to the second Γ-points, and the lower two do M-points. The notation in the figure says along line 'a' in fig. 6.7 and upper (Up) of lower (Aw) if there are two.

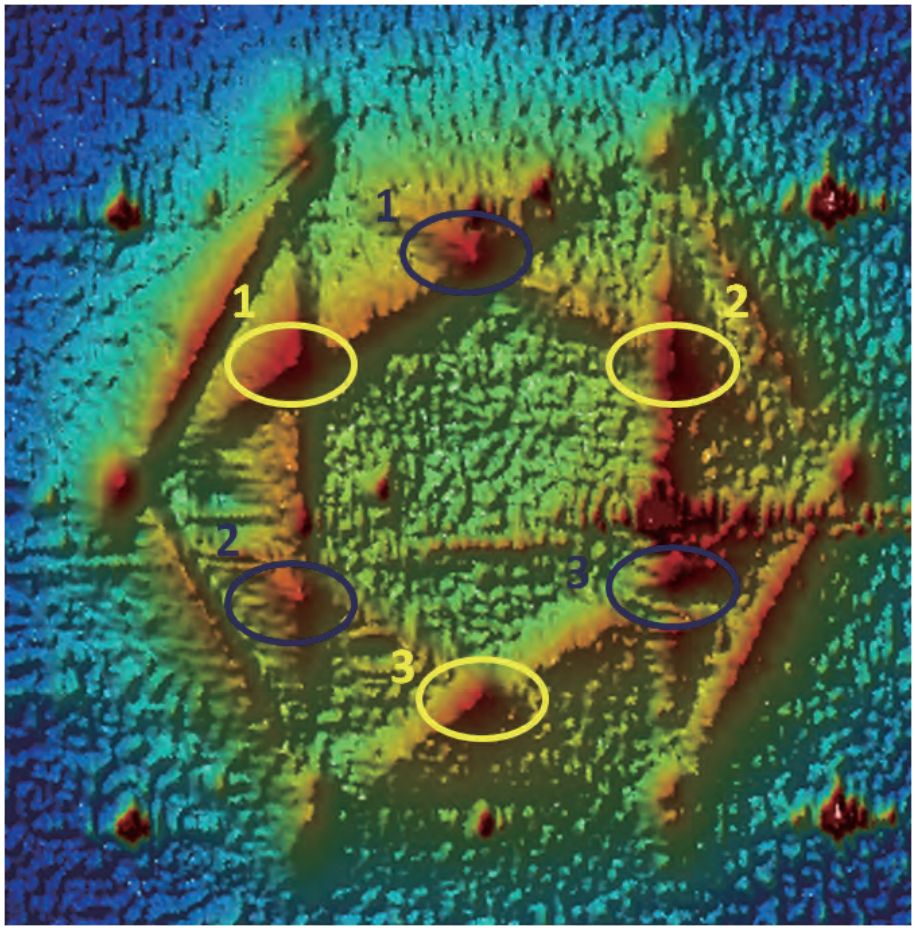

Figure 6.10: Two groups of M-points illustrated by Blue and yellow circles

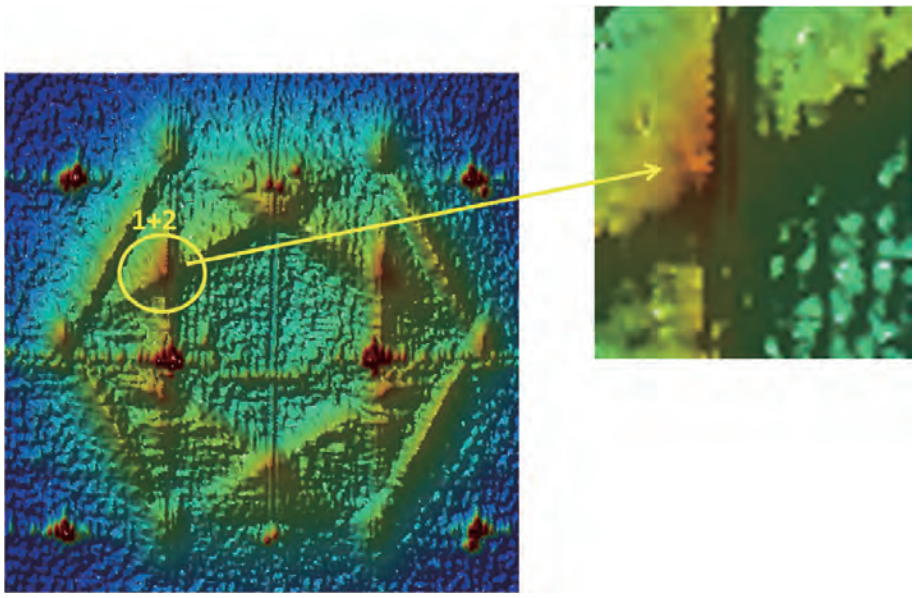

Figure 6.11: The presence of the coherence between M-points in the same group indicated by yellow circles in fig. (6.10).

Chapter 7

Meta-stable Condensation in Triangular Lattice Potentials

7.1 A triangular lattice

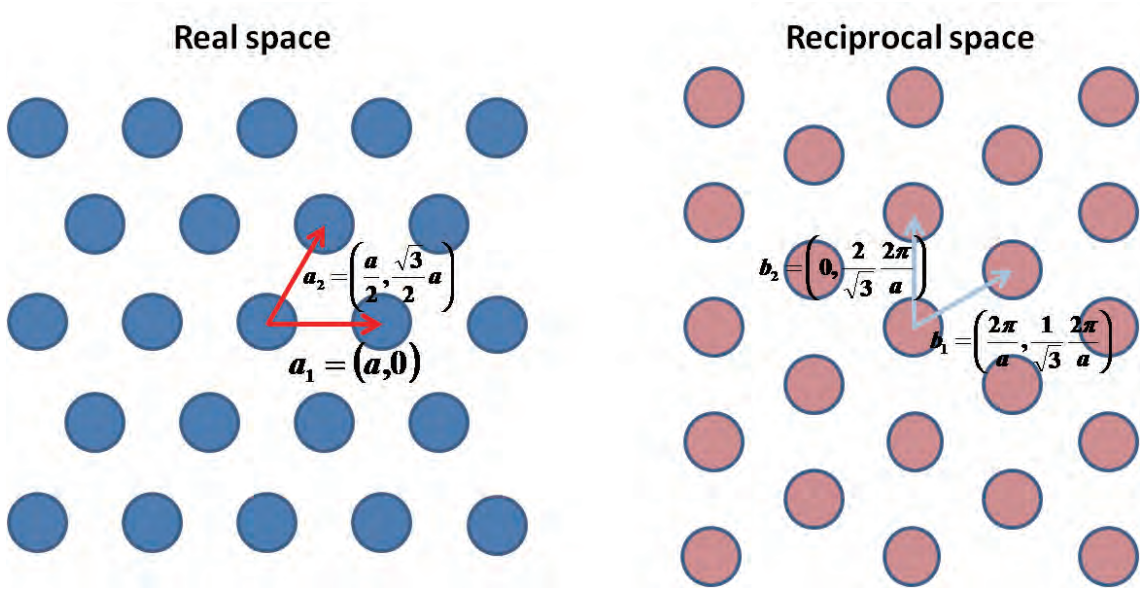

Figure 7.1: A schematic of a triangular lattice structure and its reciprocal lattice.

Fig. 7.1 shows a triangular lattice structure in real and reciprocal space. This

structure is interesting since it exhibits frustration for the classical Ising model. The triangular lattice has six-fold rotational symmetry, which is different from in the square lattice case only having four-fold symmetry. Two unit vectors of the triangular lattice with the period a can be written as $\boldsymbol{a_1} = (a, 0)$ and $\boldsymbol{a_2} = (\frac{a}{2}, \frac{\sqrt{3}a}{2})$. In addition to the six-fold rotational symmetry, a triangular lattice has also translational symmetry and reflection symmetry. The reciprocal lattice is also a triangular lattice pattern but it is rotated by 60 degrees and the period is $\frac{2}{\sqrt{3}}\frac{2\pi}{a}$. The unit vectors in the reciprocal lattice are $\boldsymbol{b_1}$ and $\boldsymbol{b_2}$ (fig. 7.1). The resulting Brillouin zones have the form shown in fig. 7.2,

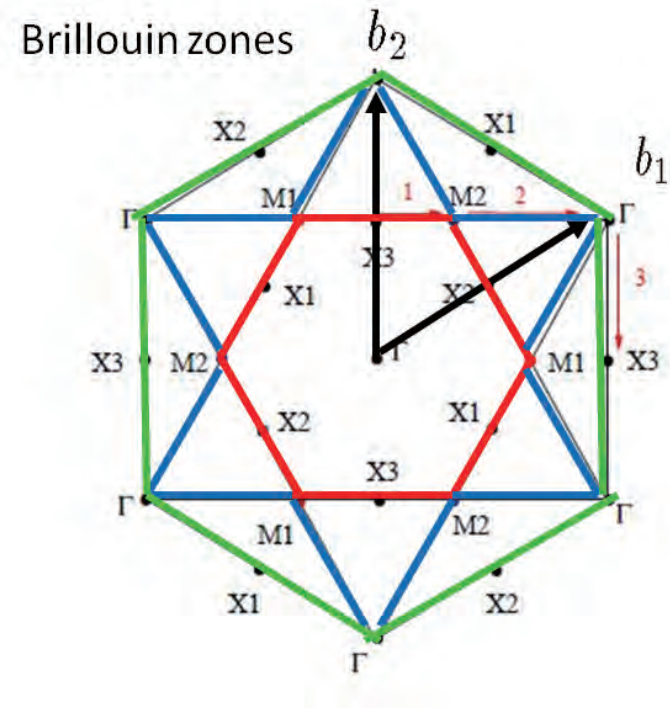

Figure 7.2: Theoretical Brillouin zones of the 2D triangular lattice. Red lines indicate the boundary of the first BZ, blue lines indicate the boundary of the second, and green lines indicate that of the third BZ. The second Γs on the hexagonal corners of the green lines are connected to the center Γ by the unit vectors in the reciprocal space, as illustrated by the $\boldsymbol{b_1}$ and $\boldsymbol{b_2}$ vectors as shown.

where inside the first BZ there are three kinds of symmetry points. The Γ-point lies in the center of the first BZ having six-fold symmetry, the X-point has two-fold symmetry, and the M-ponit has three-fold symmetry.

7.1.1 Band structure

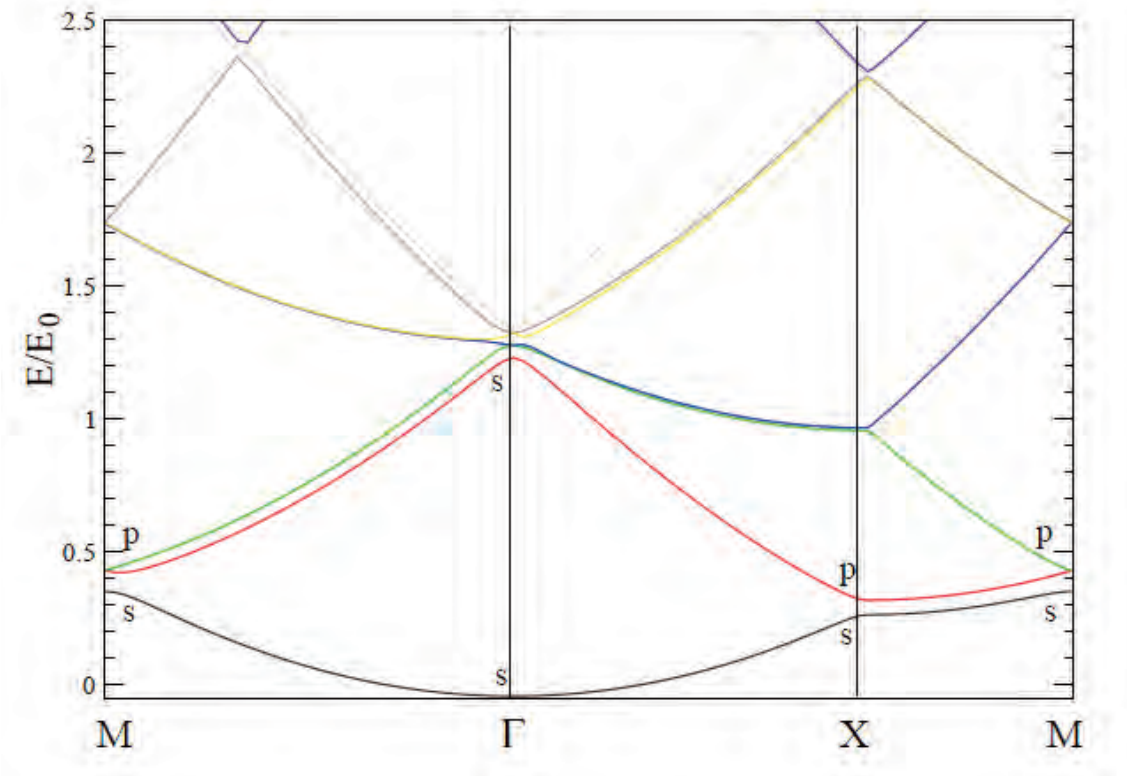

Figure 7.3: Calculated band structure for a triangular lattice in the non-interacting approximation. Here the potential amplitude $U = 0.2E_0$ is used, where $E_0 = \frac{\hbar^2}{2m}\left(\frac{2\pi}{a}\right)^2$

Fig. 7.3 shows the calculated band structure for a weak triangular lattice potential with the potential:

$$V(\mathbf{r}) = -U\left(\cos\left(i\mathbf{k_1}\cdot\mathbf{r}\right) + \cos\left(i\mathbf{k_2}\cdot\mathbf{r}\right) + \cos\left(i\mathbf{k_3}\cdot\mathbf{r}\right)\right), \tag{7.1}$$

with $\mathbf{k_1} = (0, \frac{2}{\sqrt{3}}\frac{2\pi}{a})$, $\mathbf{k_2} = (\frac{2\pi}{a}, \frac{1}{\sqrt{3}}\frac{2\pi}{a})$, and $\mathbf{k_3} = (\frac{2\pi}{a}, -\frac{1}{\sqrt{3}}\frac{2\pi}{a})$. At the symmetric points, the eigenstates can be classified according to the symmetry property of the rotation group. At the Γ-point, the lowest energy ground state exhibits non-degenerate 1s-wave symmetry on each site (fig. 7.4a). The X-point has two-fold degeneracy, resulting in three meta-stable states X1, X2 and X3. These three states are displayed in fig. 7.4(b-d), and these states have 2p-symmetry (antisymmetric along the lattice axes). At the M-points, there are three bands in a narrow energy window. The lowest has 1s-symmetry,

while the other two have 2p-symmetry with different axes of symmetry (fig. 7.5). For a weak potential, the three states can be written as

$$
\begin{aligned}
|\Psi_s^M\rangle &= \frac{1}{\sqrt{3}}\left(|\Psi_A^M\rangle + |\Psi_B^M\rangle + |\Psi_C^M\rangle\right) \\
|\Psi_{px}^M\rangle &= \frac{1}{\sqrt{6}}\left(2|\Psi_A^M\rangle - |\Psi_B^M\rangle - |\Psi_C^M\rangle\right) \\
|\Psi_{py}^M\rangle &= \frac{1}{\sqrt{2}}\left(|\Psi_B^M\rangle - |\Psi_C^M\rangle\right)
\end{aligned}
\tag{7.2}
$$

with

$$
\begin{aligned}
|\Psi_1^M\rangle &= \frac{1}{\sqrt{V}}\exp(i\mathbf{k_{MA}}\mathbf{r}) \\
|\Psi_2^M\rangle &= \frac{1}{\sqrt{V}}\exp(i\mathbf{k_{MB}}\mathbf{r}) \\
|\Psi_3^M\rangle &= \frac{1}{\sqrt{V}}\exp(i\mathbf{k_{MC}}\mathbf{r}),
\end{aligned}
\tag{7.3}
$$

where $\mathbf{k_{MA}} = (-\frac{2}{3}\frac{2\pi}{a}, 0)$, $\mathbf{k_{MB}} = (\frac{1}{\sqrt{3}}\frac{2\pi}{a}, \frac{1}{3}\frac{2\pi}{a})$ and $\mathbf{k_{MC}} = (\frac{1}{\sqrt{3}}\frac{2\pi}{a}, -\frac{1}{3}\frac{2\pi}{a})$. V is the volume of the system and r is a real coordinate vector.

7.2 Results

7.2.1 Dynamical meta-stable condensation in 2D triangular Lattice Potentials

We examine triangular lattice potentials with a period of $2\mu m$ and $4\mu m$ near zero-detuning. As we here already see in the square lattice case, the period of the lattice affects the relation between the scale of BZs of the lattice and the bottle-neck region where LPs collect below the threshold pump power. Fig. 7.6 shows the FF images at several different pump powers. In a $2\mu m$ device, the hexagon at the boundary of the first BZ has almost the same size as the bottle neck region in momentum space. At the threshold pump power, meta-stable condensation occurs at the M-points of the hexagonal vortices of the first BZ boundary. Increasing the pump power, LPs decay into lower energy states and meta-stable condensation occurs at the X-points, and then at the central the Γ-point at the highest pump power. In a $4\mu m$ device, the size of BZs is half of that of $2\mu m$ lattices. In this case, meta-stable condensation occurs first at the the second Γ points, which are located at the hexagonal corners of the boundary of the third (also second) BZ. Increasing pump power, the emission from the lower energy states, the M-points and the X-points at the boundary of the first BZ, become larger, and finally the emission from the ground state (Γ at the center) becomes dominant. Below we focus on M-point condensation.

7.2.2 Spectroscopy of the M-points condensates

Due to the periodic potential, the M-points are not independent and energetically identical. We measure the energy of M-point LPs by taking a slice including the M-point in FF and inputing this to the spectrometer (illustrated in fig. 7.7). Fig. 7.8 shows the pump power dependence of the energy of the M-points. We confirm that the energy of M-points condensates are same within the linewidth especially near the threshold pump power where the M-point condensates are dominant. This is consistent with the theory, and therefore we can treat the system to be homogeneous. In fig. 7.8, therefore the energy of all M-points in both the $2\mu m$ and $4\mu m$ cases display a nonlinear jump around $P_{th} \sim 10mW$. This is because of the mean field repulsive interaction of LPs which is enhanced when condensation occurs. Second, the linewidth of the LP emission suddenly decreases at the threshold pump power and then gradually increases. The first decrease is due to the formation of the condensate. Below the threshold pump

power, the linewidth is determined by the lifetime of LPs ~a few ps. Above threshold, the linewidth is determined by the coherence time of the LP condensates ~ 10ps. The sudden decrease of the linewidth is one evidence for condensation. The increase of the linewidth after the threshold is due to LP-LP interaction.

7.2.3 Coherence among M-points in FF

We also examine the coherence among the emission from the M-points by the Michelson Interferometry (MI). Because the M-points have three-fold rotational symmetry, we can separate six identical M-points into two groups which have three M-points respectively (illustrated in fig. 7.9 by red and yellow circles). Due to the triangular lattice potentials, three M-points in the same group are connected and form the states corresponding to eq. 7.3. The M-points in different groups are on the other hand not connected by the triangular lattice. Theoretically they are of the same energy, so that there is a possibility that other effects such as interaction may introduce the coherence between them. Fig. 7.10 shows the result of the interferometry between three M-points. Using the MI set-up, on the detection CCD M1 and M2 indicated by yellow circles (below we label these M1Y or M2Y, and others in the same manner), and M2Y and M3Y are overlapped. We see coherence for M-points in the same group as indicated by the formation of fringes. We confirm the M-points in the same group are actually coherently connected due to the triangular potential. Fig. 7.11 shows the absence of coherence between M-points in different groups, though the energy of those are same within the linewidth.

We have two options to explain this absence of coherence. First, because our image is integrated over a few tens ms, the interference fringes are averaged out with an energy difference more than the order of peV. This value is almost 0 in the real situation, so that by a small energy difference between M_{Yellow} and M_{Red} (even if it is within the linewidth) the coherence between M_{Yellow} and M_{Red} are averaged out. The other scenario is that the M-points state is formed in the M_{Yellow} or M_{Red} by shot-to-shot. Our pump is a pulsed laser, so that before the next laser pulse all LPs disappear due to the photonic leakage from the cavity. The image is the statistically averaged image of shot-to-shot experiments. So if the state in one of the two M-point groups is selected in the system by a shot-to-shot measurement, the absence of the coherence between the two M groups can be explained even if the energy of these two are completely same. To identify this reason we need time-resolved measurement using a streak camera.

7.2.4 Possible candidates for the M-points condensates

As we saw above, three M-points in the same group are coherently connecterd to form the state. We consider what the state is (or the states are). Our start of the discussion is one experimental result that the intensity of three M-points are almost same. Fig. 7.12 shows the intensity of each M-point against the pump power which is normalized by the intensity of one M-point. All intensities, especially around the threshold pump power, are almost the same within 70% error. According to fig. 7.5 and eq. 7.3, the s-state has a 1:1:1 ratio in the intensity at three M-points, while the two degenerate p-states have 0:1:1 and 4:1:1 ratios respectively. However, the two degenerate p-states, $|\Psi^M_{px}>$ and $|\Psi^M_{py}>$, are degenerate so that we may have linear superposition states of these two which have 1:1:1 ratio of the intensity at three M-points, which is

$$\begin{aligned} |\Psi^M_{px+ipy}\rangle &= \frac{1}{\sqrt{2}}\left(|\Psi^M_{px}\rangle + |\Psi^M_{px}\rangle\right) \\ |\Psi^M_{px-ipy}\rangle &= \frac{1}{\sqrt{2}}\left(|\Psi^M_{px}\rangle - |\Psi^M_{px}\rangle\right). \end{aligned} \tag{7.4}$$

Fig. 7.13 display the wave functions of these three states. All states have the same pattern of the wave function, with a difference only in their positions. The most interesting property of these three states is that they have phase chirality where the intensity goes to zero (This may be interpreted as a quantised vortex, according to ref. [41], [42]). Next to a clock-wise vortex, there are anticlock-wise vortices and they form hexagonal vortex-antivortex lattices, while intensity peaks form triangular lattices. This type of vortex-antivortex lattice has been also explored in nonlinear photonic lattices [49] [50] [51]. In the s-state, intensity peaks are on the traps and around traps vortices exist. On the other hand, in the two p-states, the vortices exsit on the traps.

One thing should be noted that any statistical mixture also has a 1:1:1 ratio of the intensity at three M-points in FF. But according to fig. 7.14, the NF image of statistical mixture of 50% px+ipy and 50% px-ipy has a different pattern to the NF images of s, px+ipy and px-ipy. Especially the intensity dips are patterned in a triangular lattice, while the intensity peaks are in s, px+ipy and px-ipy cases.

7.2.5 Near field imaging with the filter in the momentum space for the M-points condensates

We take NF images with the mask selecting only three M-points on the FF plane (fig. 7.15). The result is shown in fig. 7.16, and clearly show the peaks patterned in a triangular lattice. Although we do not know which vortex-antivortex lattice is the state we observe, the esult indicates the state at M-points is a vortex-antivortex lattice state (comparison with fig. 7.14).

7.3 LP-LP interaction effect on degenerate states

In a band calculations, the two p-states and every superposition of these have the same energy. But experiments says that a vortex-antivortex lattice is favored. Here we consider the repulsive interaction effect in a similar way described in [43]. Starting with the general form of the repulsive interaction energy,

$$E_{int} = \int\int d\mathbf{r}d\mathbf{r}'\hat{\Psi}^{\dagger}(\mathbf{r}')\hat{\Psi}^{\dagger}(\mathbf{r})\hat{U}\hat{\Psi}(\mathbf{r}')\hat{\Psi}(\mathbf{r}), \tag{7.5}$$

where $\hat{\Psi}$ is the field operator for LPs, $\hat{U}$ is the interaction operator. We here introduce the order parameter ψ and replace it with $\hat{\Psi}$ and, assume a delta-function like interaction to $\hat{U}$. Furthermore we assume only the two p-states at M-points, so that $\psi = \alpha\psi_{px} + \beta\psi_{py}$. ψ_{px} and ψ_{py} are the order parameters for $|\Psi^M_{px}>$ and $|\Psi^M_{px}>$ defined in eq. (7.3), and then we use the single particle wave functions described in eq. (7.3) and (7.4). Using the following integrals

$$\begin{aligned} \int d\mathbf{r}|\Psi_{px}|^4 &= \frac{3}{2} \\ \int d\mathbf{r}|\Psi_{py}|^4 &= \frac{3}{2} \\ \int d\mathbf{r}|\Psi_{px}|^2|\Psi_{py}|^2 &= \frac{5}{6} \\ \int d\mathbf{r}\Psi^{*2}_{px}\Psi^2_{py} &= -\frac{1}{2}, \end{aligned} \tag{7.6}$$

after some algebra we get the form of the interaction energy of

$$E_{int} \propto \frac{3}{2}|\alpha|^4 + \frac{3}{2}|\beta|^4 + \frac{10}{3}|\alpha|^2|\beta|^2 - \frac{1}{3}Re\left(\alpha^{*2}\beta^2\right). \tag{7.7}$$

Because $|\alpha|^2 + |\beta|^2 = 1$ we use the form of $\alpha = \cos(\theta)$ and $\beta = \exp(i\phi)\sin(\theta)$, and finally the energy is written as

$$\begin{aligned} E_{int} &\propto \frac{3}{2}\left(\cos^4(\theta) + \sin^4(\theta)\right) + \frac{10}{3}\cos^2(\theta)\sin^2(\theta) - \frac{1}{3}\cos^2(\theta)\sin^2(\theta)\cos^2(\phi) \quad (7.8) \\ &\propto \frac{3}{2} + \frac{1}{6}\sin^2(2\theta)\sin^2(\phi). \end{aligned}$$

Eq. (7.9) says that when $\theta = \frac{\pi}{4}, \frac{3\pi}{4}, \frac{5\pi}{4}, \frac{7\pi}{4}$ and $\phi = \frac{\pi}{2}, \frac{3\pi}{2}$, namely when the state is $|p_x + ip_y\rangle$ or $|p_x - ip_y\rangle$, the interaction energy takes its maximum. So then repulsive interaction lift the degeneracy up.

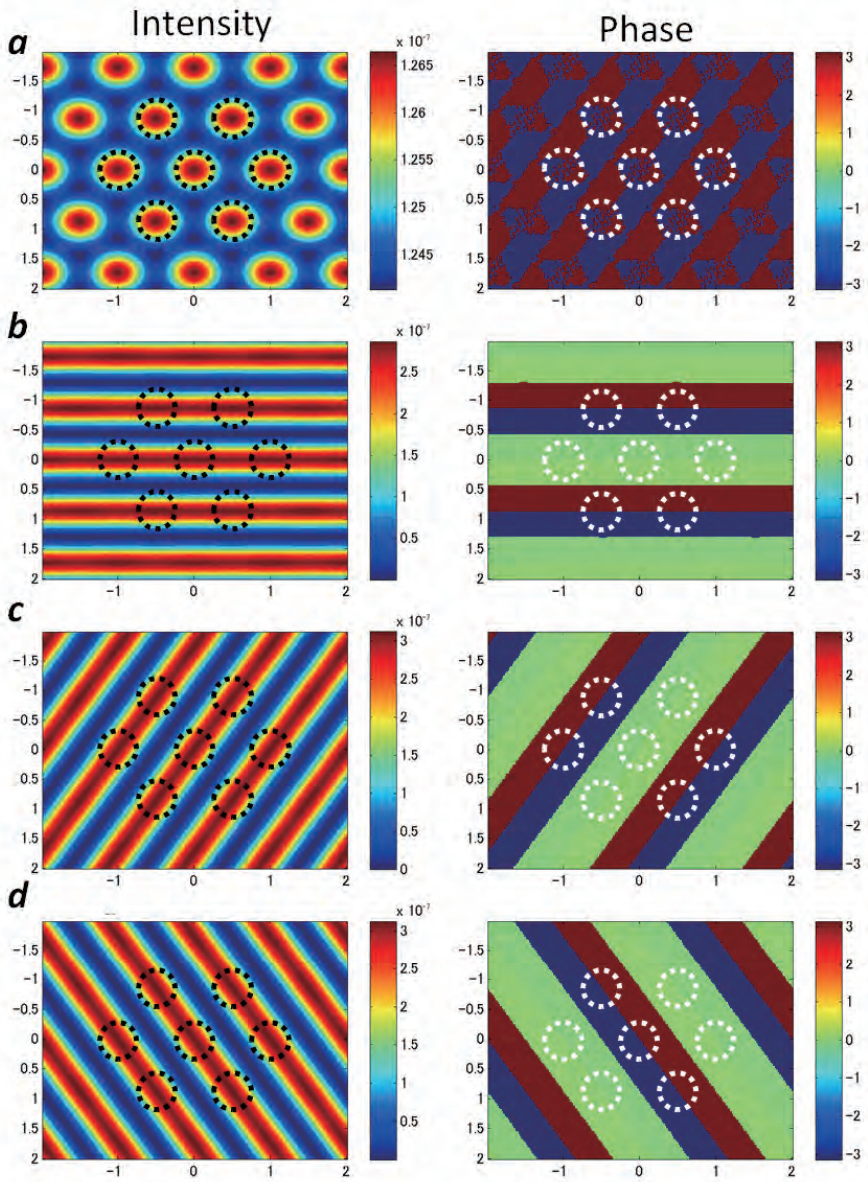

Figure 7.4: Single state wave functions of the ground state at Γ and meta-stable states at X points.

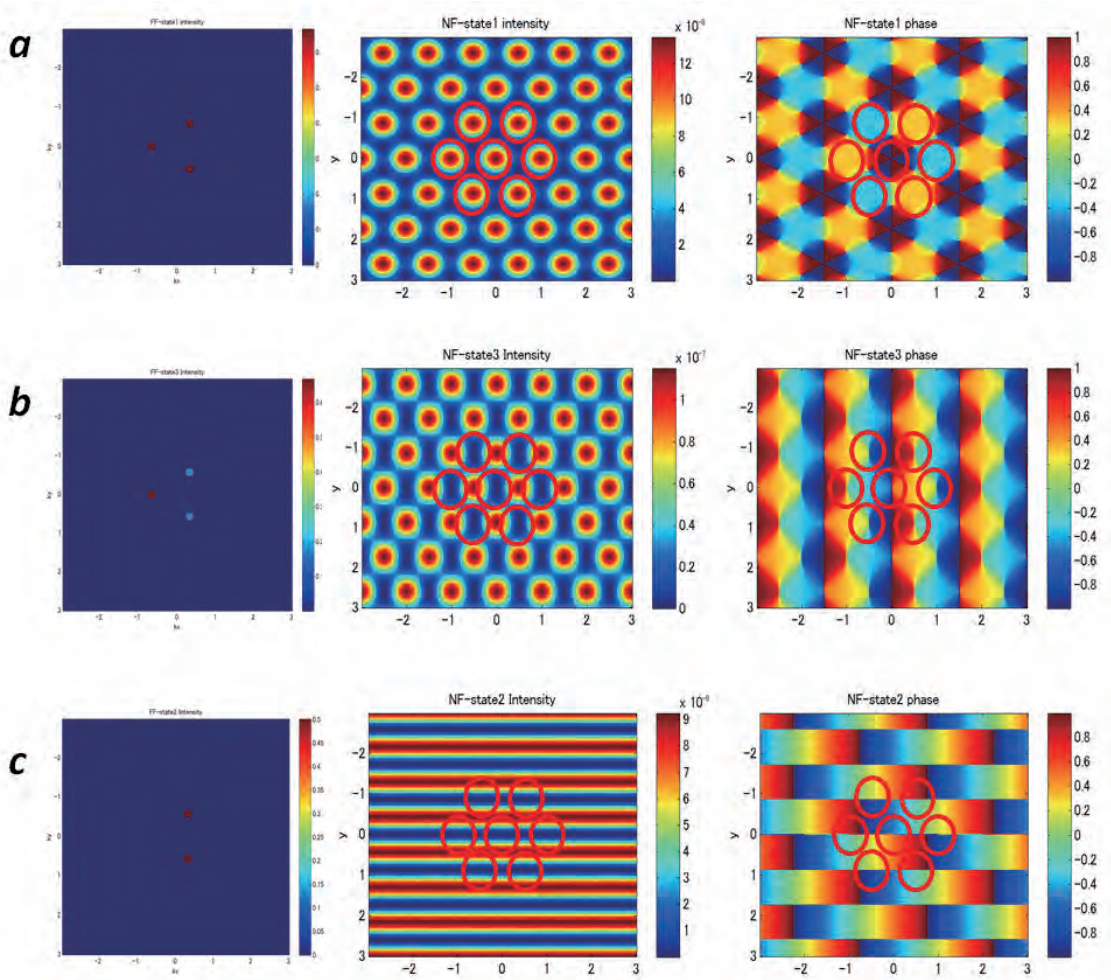

Figure 7.5: Single state wave functions of three lowest states at the M-points.

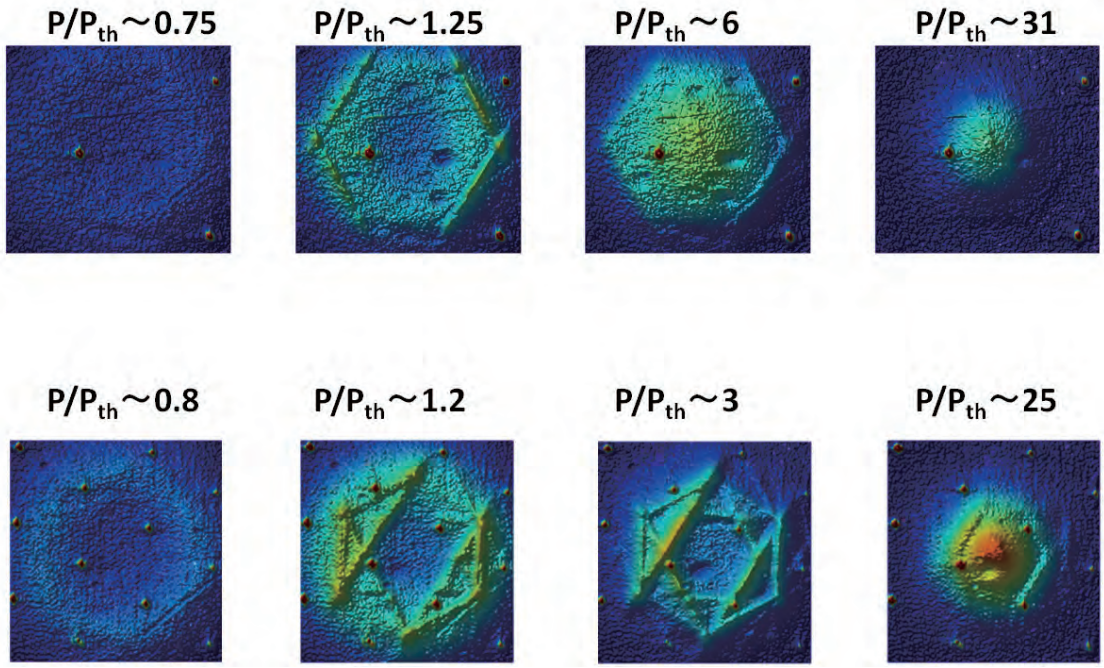

Figure 7.6: FF images with $a = 2\mu m$ (the top row) and $a = 4\mu m$ (bottom row). The laser diffraction peaks give the size of the reciprocal lattice experimentally.

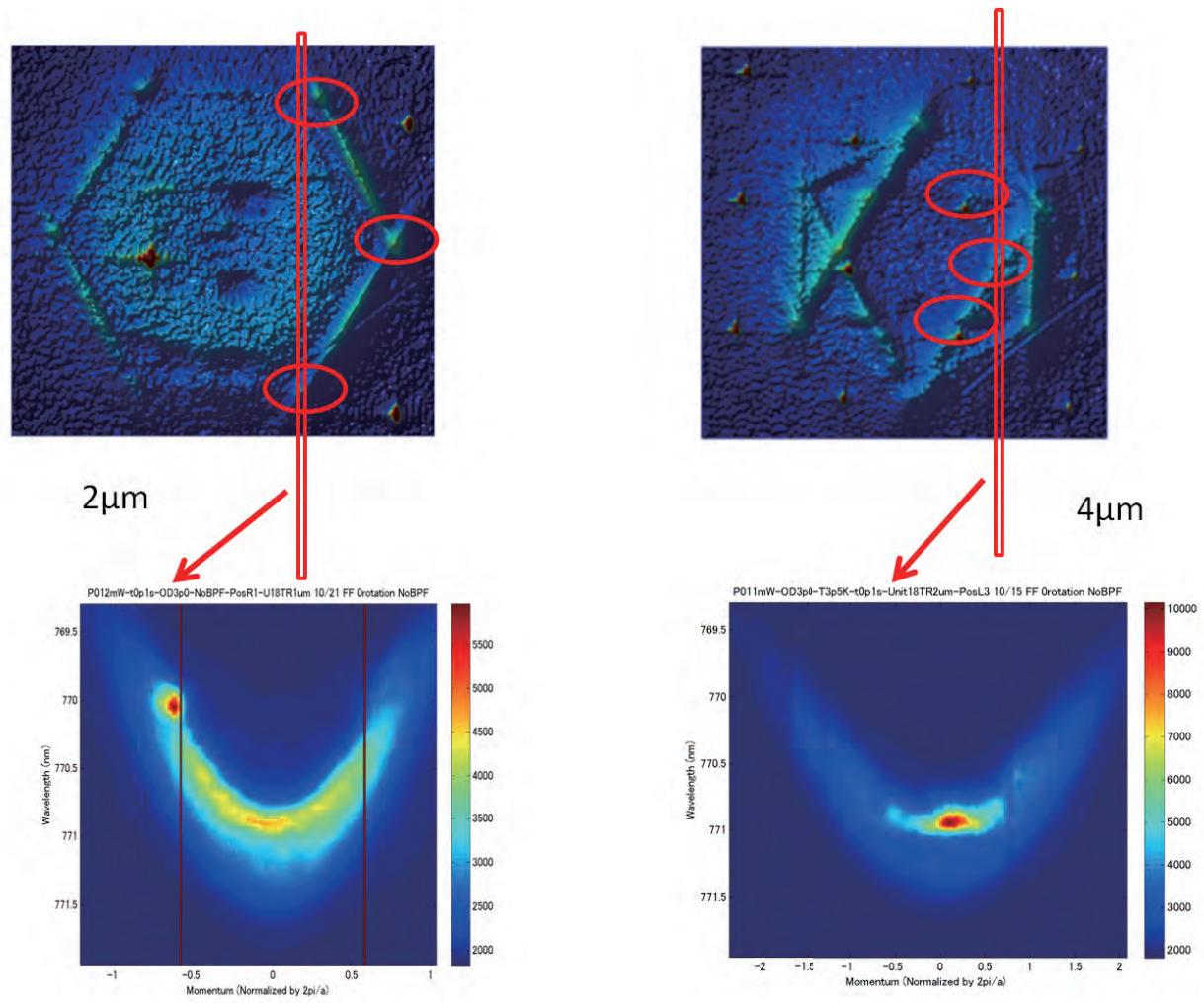

Figure 7.7: The dispersion of the M-point condensate. Slices along several positions including each M-point are shown.

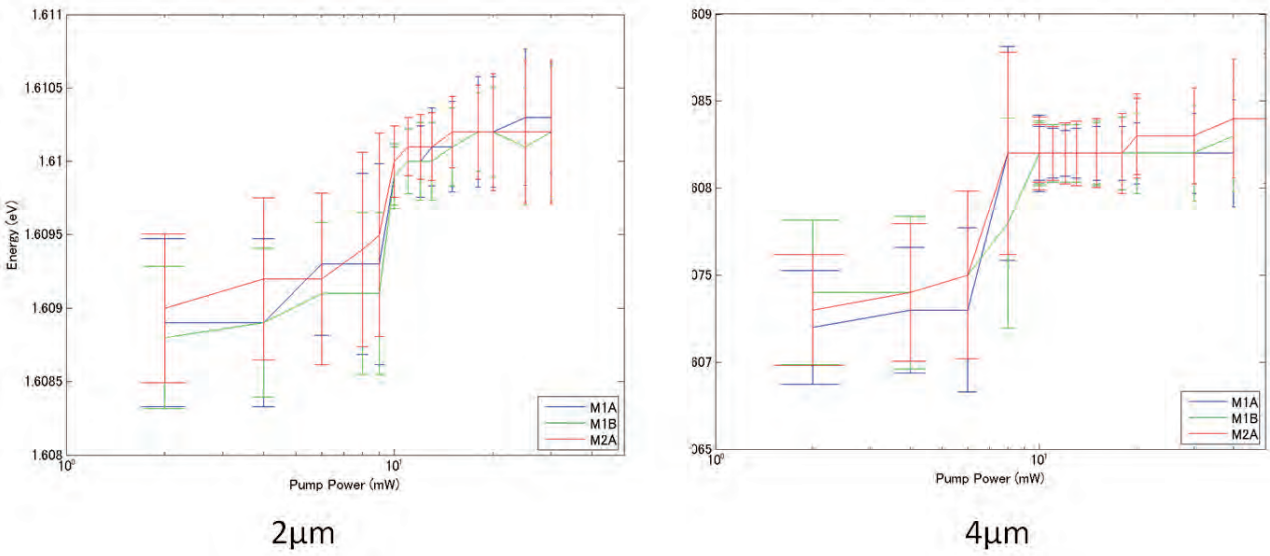

Figure 7.8: The energy of the three M-points versus pump powers. LP condensates have a finite lifetime due to photonic leakage from the cavity leading to a finite linewidth. The averaged linewidth of M-points emission are shown as error bars.

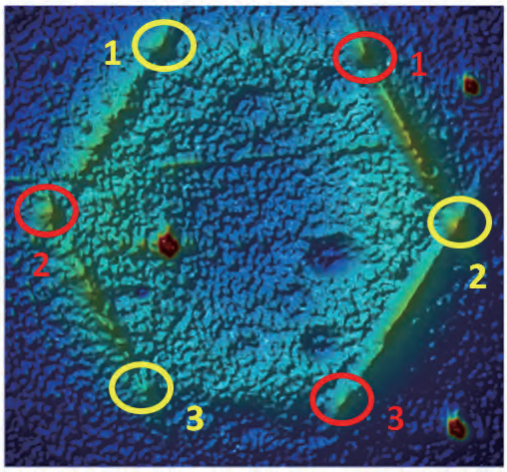

Figure 7.9: Two groups of M-points illustrated by red and yellow circles.

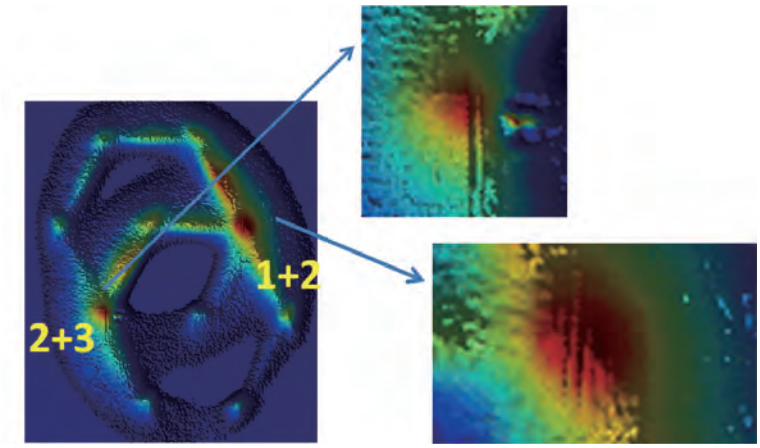

Figure 7.10: The presence of the coherence between M-points in the same group

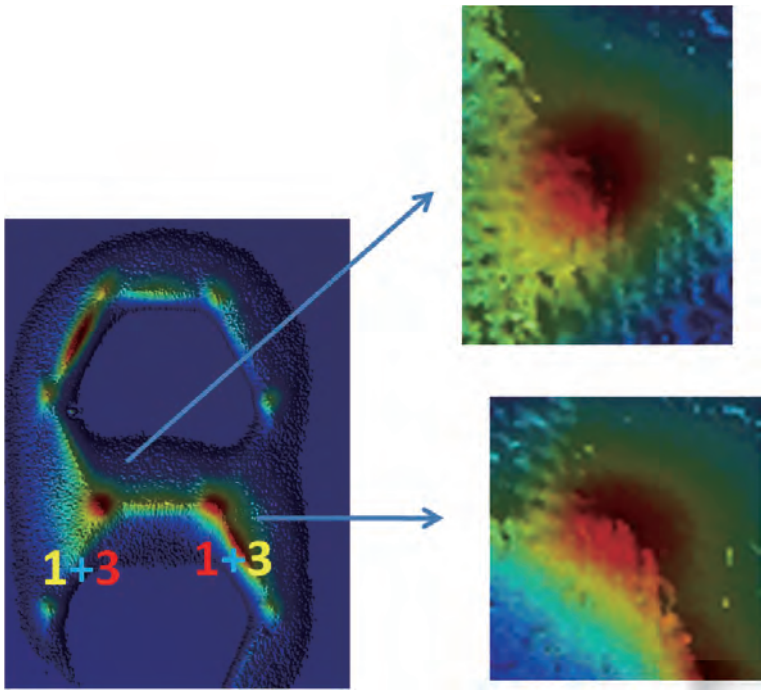

Figure 7.11: The absence of the coherence between M-points in different groups

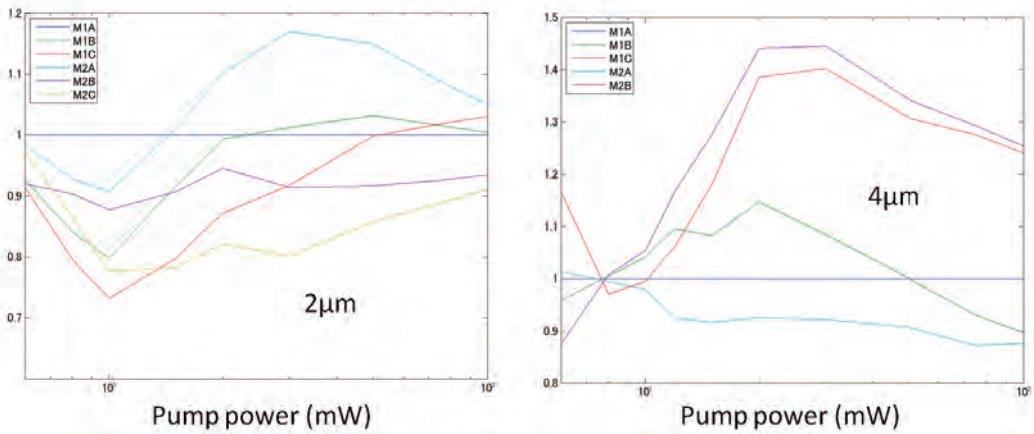

Figure 7.12: The intensity of M-points normalized by that of one M-point. In the $a = 4\mu m$ case, one M-point overlaps with the laser diffraction peak so that only five are shown.

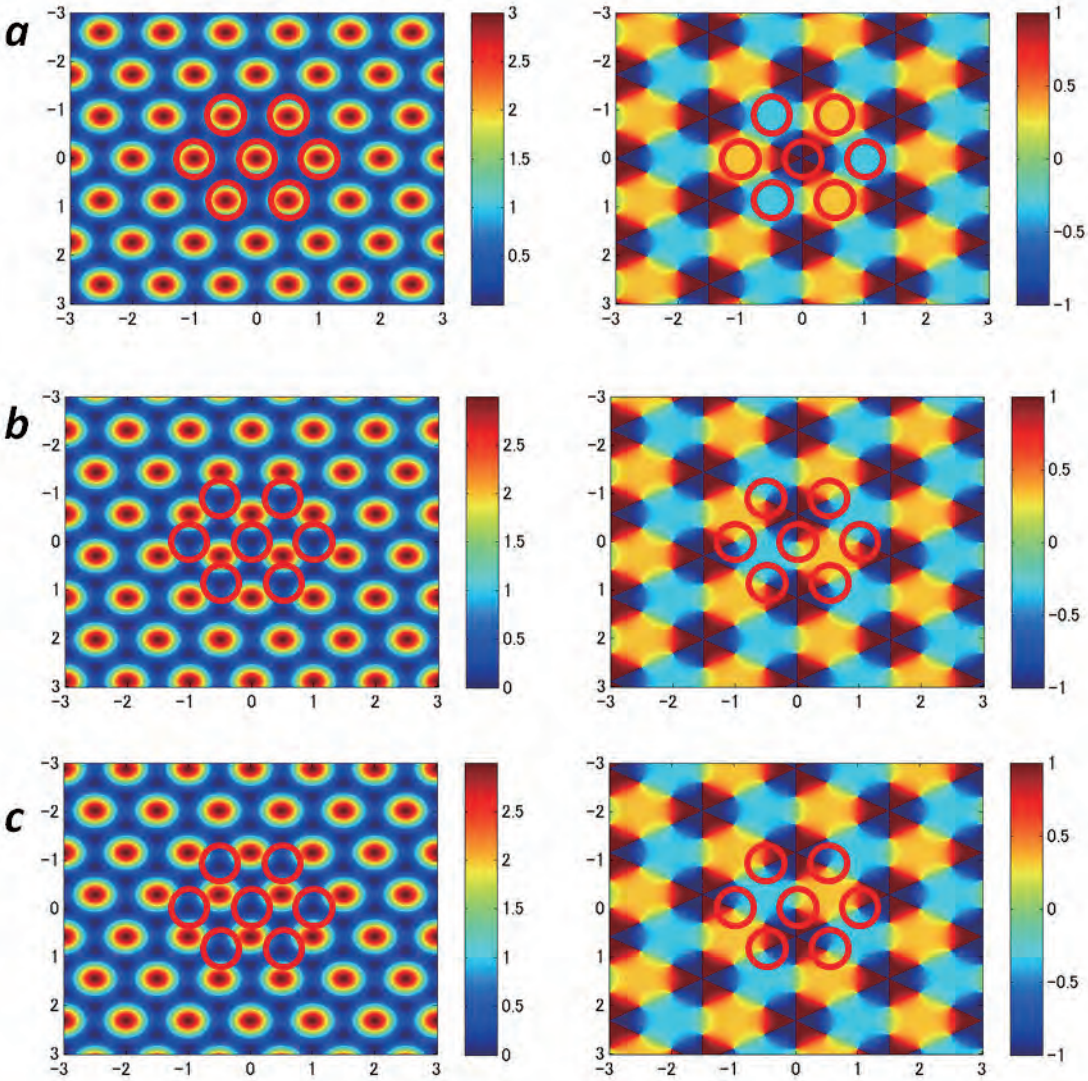

Figure 7.13: Wavefunctions of the s-state (a), px+ipy (b) and px-ipy (c) states at the M-points. At the left column shows the intensity, while at the right column shows the phase of the wavefunctions. Red circles indicate the trap position.

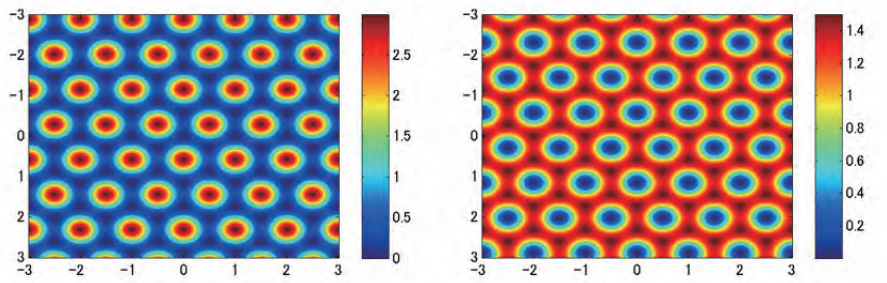

Figure 7.14: Comparison between px-ipy (left) and a statistical mixture of 50 percent px+ipy and 50 percent px-ipy (right).

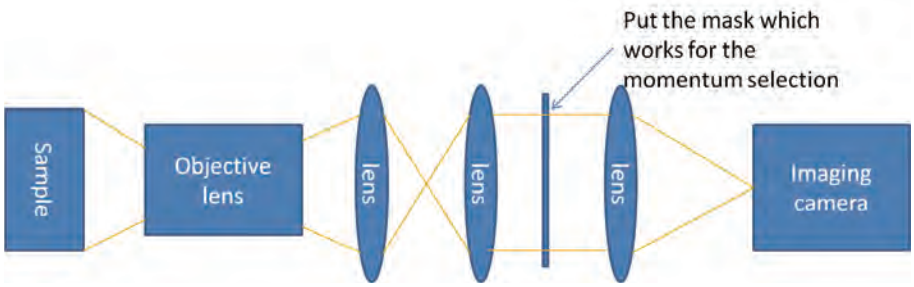

Figure 7.15: Schematic of the optics set-up for NF imaging with a mask

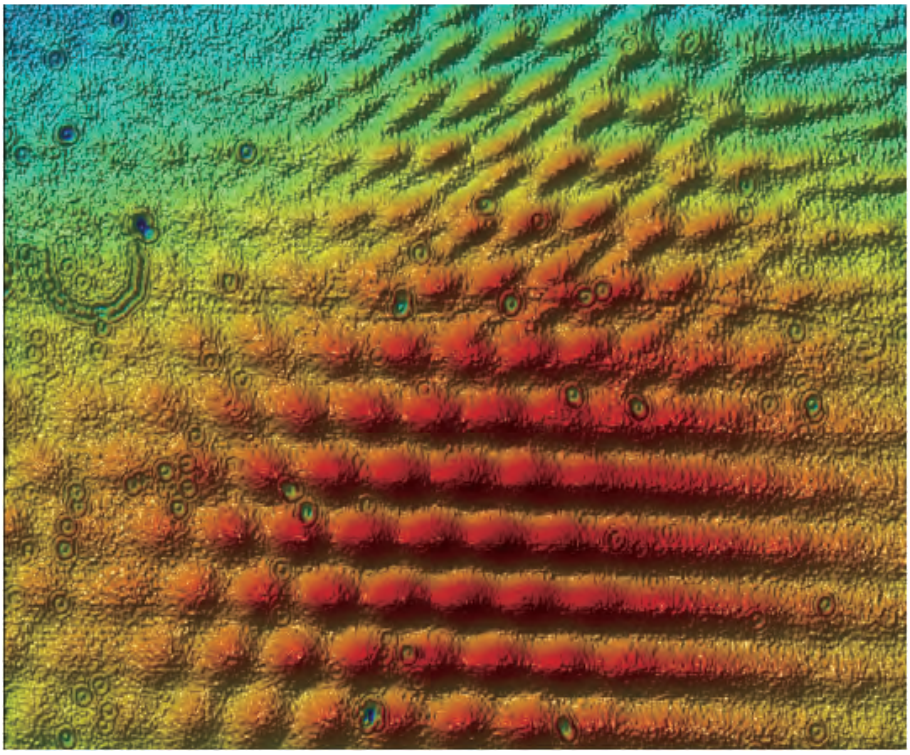

Figure 7.16: A observed NF image with the mask selecting only the three M-points on the FF plane.

Chapter 8

Summary and Future Prospect

Summary

In the square lattice potentials, we have observed meta-stable condensation of the d-wave symmetry state at the M-point. The d-wave symmetry originates from the symmetry of the Bloch state where condensation occurs. Meta-stability is formed where the state is the band bottom and seperated by the band gap from the lower band. Through FF interference pattens and spatially and spectrally resolved images, we have detected the NF and FF distribution of the d-wave condensates. These results are consistent with the band calculation with weak potentials. The mode competition between several condensates in square lattice potentials has been modeled with simple coupled rate equations,which shows consistency with the experimental result qualitatively.

In the honey-comb lattice potentials, we have observed the evidence for a vortex-antivortex lattice order. In this case, at the M-points, the meta-stability occurs at only the third band whose Bloch wave-function has a vortex-antivortex lattice order. We have confirmed that the three M-points in the M1 (M2) group are degenerate and coherently connected through the spectroscopy and Michelson interferometry. Compared to the observation in non-linear photonic lattices, where the vortex-antivortex order is given (ref. [41], [42]), in our scheme the formation of vortex-antivortex lattices are spontaneous due to the dynamic nature of LP condensates.

In the triangular lattice potentials, we have observed meta-stable condensates at the M-points. This topological property originates from the p-like symmetry of the Bloch state at the M-points. Through the spectroscopy and Michelson interferometry, it is

confirmed that the three M-points in the M1 (M2) group are degenerate and coherently connected. The band calculation, the 1:1:1 intensity ratio of the three M1(M2)-points in measured FF patterns, and the measured NF image of the M-point state which is selected in momentum space, indicates us the presence of a vortex-antivortex patterns.

Future prospect One direction to expand this work is to include the spin degree of freedom. Though ,in this work, we exclude the spin physics for simplicity by pumping with circularly polarized lasers, the spin physics should give rich physics. The controlability of not only the orbit but also the spin is a good remark of the next step. Because the spin-orbit interaction in higher orbital states is the key for colossal magnetism [57], the LP system may become a good system for simulation of colossal magnetism.

We also note that exploring the honey-comb lattice physics is also attractive. Dirac corns, where the band dispersion is linear against the center of corns, are proposed to exist in the p-band of the two-dimensional honey-comb lattice [58]. Particles with linear dispersion is considered to be relativistic and recently have been attracting many researchers due to the appearence of graphene. Exploring the particles with linear dispersion is also interesting direction.

References

[1] http://www.riken.go.jp/engn/r-world/info/release/press/2009/091002/image/091002.pdf

[2] Bose, S. N., "Plancks Gesetz und Lichtquantenhypothese", *Zeitschrift fur Physik* **26**, 178 (1924)

[3] Einstein, A., "Quantentheorie des einatomigen idealen Gases", *Sitzungsberichte der Preussischen Akademie der Wissenschaften* **1**, 3 (1925)

[4] M.H. Anderson, J.R. Ensher, M.R. Matthews, C.E. Wieman, and E.A. Cornell, "Observation of Bose-Einstein Condensation in a Dilute Atomic Vapor", *Science* **269** 198 (1995)

[5] K.B. Davis, M.-O. Mewes, M.R. Andrews, N.J. van Druten, D.S. Durfee, D.M. Kurn, and W. Ketterle, "Bose-Einstein condensation in a gas of sodium atoms", *Physical Review Letters* **75** 3969 (1995)

[6] M. R. Matthews, B. P. Anderson, P. C. Haljan, D. S. Hall, "Vortices in a Bose-Einstein Condensate", *Physical Review Letters* **83** 2498 (1999)

[7] C. Weisbuch, M. Nishioka, A. Ishikawa, and Y. Arakawa, "Observation of the coupled exciton-photon mode splitting in a semiconductor quantum microcavity", *Physical Review Letters* **69** 3314 (1992)

[8] A. Imamoglu, R. J. Ram, S. Pau and Y. Yamamoto, "Nonequilibrium condensates and lasers without inversion: Exciton-polariton lasers", *Physical Review A* **53** 4250 (1996)

[9] H. Deng, G.Weihs, C.Santori, J.Bloch, and Y.Yamamoto, "Condensation of Semiconductor Microcavity Exciton Polaritons", *Science* **298** 199 (2002)

[10] H. Deng, G. Weihs, D. Snoke, J. Bloch, and, Y. Yamamoto, "Polariton Lasing vs. Photon Lasing in a Semiconductor Microcavity", *PNAS* **100** 15318 (2003)

[11] J. Kasprzak, M. Richard, S. Kundermann, A. Baas, P. Jeambrun, J. M. J. Keeling, F. M. Marchetti, M. H. Szymaska, R. Andre, J. L. Staehli, V. Savona, P. B. Littlewood, B. Deveaud and Le Si Dang, "Bose?Einstein condensation of exciton polaritons", *Natuer* **443** 409 (2006)

[12] R.B. Balili, V. Hartwell, D. Snoke, L. Pfeiffer, and K. West, "Bose-Einstein Condensation of Microcavity Polaritons in a Trap", *Science* **316** 1007 (2007)

[13] H. Deng, D. Press, S. Goetzinger, G. S. Solomon, R. Hey, K.H. Ploog , and Y. Yamamoto, "Quantum Degenerate Exciton-Polaritons in Thermal Equilibrium", *Physical Review Letters* **97** 146402 (2006)

[14] T. Nikuni, M. Oshikawa, A. Oosawa, and H. Tanaka, "Bose-Einstein Condensation of Dilute Magnons in TlCuCl3", *Physical Review Letters* **84** 5868 (2000)

[15] S. O. Demokritov, V. E. Demidov, O. Dzyapko, G. A. Melkov, A. A. Serga, B. Hillebrands and A. N. Slavin, "Bose-Einstein condensation of quasi-equilibrium magnons at room temperature under pumping", *Nature* **443** 430 (2006)

[16] J. Klaers, J. Schmitt, F. Vewinger and M. Weitz, "Bose-Einstein condensation of photons in an optical microcavity", *Nature* **468** 545 (2010)

[17] I. Buluta and F. Nori, "Quantum Simulators", *Science* **326** 108 (2009)

[18] I. Bloch, J. Dalibard and W. Zwerger, "Many-body physics with ultracold gases", *Review of Modern Physics* **80** 885 (2008)

[19] M. P. A. Fisher, P. B. Weichman, G. Grinstein, and D. S. Fisher, "Boson localization and the superfluid-insulator transition", *Physical Review B* **40**, 546 (1989)

[20] M. Imada, A. Fujimori, and Y. Tokura, "Metal-insulator transitions", *Review of Modern Physics* **70**, 1039 (1998)

[21] N. E. Bickers, D. J. Scalapino, and S. R. White , "Conserving Approximations for Strongly Correlated Electron Systems: Bethe-Salpeter Equation and Dynamics for the Two-Dimensional Hubbard Model", *Physical Review Letters* **62**, 961 (1989)

[22] M. Imada, "Universality classes of metal-insulator transitions in strongly correlated electron systems and mechanism of high-temperature superconductivity", *Physical Review B* **72**, 075113 (2005)

[23] M. Greiner, O. Mandel, T. Esslinger, T.W. Hansch, and I. Bloch, "Quantum Phase Transition from a Superfluid to a Mott Insulator in a Gas of Ultracold Atoms", *Nature* **415** 39 (2002)

[24] R. Jordens, N. Strohmaier, K. Gunter, H. Moritz, T. Esslinger, "Metallic and Insulating Phases of Repulsively Interacting Fermions in a 3D Optical Lattice", *Nature* **455** 204 (2008)

[25] U. Schneider, L. Hackermuller, S. Will, Th. Best, I. Bloch, T. A. Costi, R. W. Helmes, D. Rasch, A. Rosch, "A Mott insulator of fermionic atoms in an optical lattice", *Science* **322** 1520 (2008)

[26] R. Fazio, H. van der Zantc, "Quantum phase transitions and vortex dynamics in superconducting networks", *Physics Reports* **355**, 235 (2001)

[27] R. Gerritsma, G. Kirchmair, F. Zahringer, E. Solano, R. Blatt and C. F. Roos, "Quantum simulation of the Dirac equation", *Nature* **463** 68 (2010)

[28] F. Zahringer, G. Kirchmair, R. Gerritsma, E. Solano, R. Blatt, and C. F. Roos, "Realization of a Quantum Walk with One and Two Trapped Ions", *Physical Review Letters* **104** 100503 (2010)

[29] E. Hanamura and H. Haug, "Condensation effects of excitons", *Physics Report* **33**, 209 (1977)

[30] V. Savona, C. Piermarocchi, A. Quattropani, P. Schwendimann, and F. Tassone, "Optical properties of microcavity polaritons", *Phase Transition* **68**, 169 (1999)

[31] N. Y. Kim, C. W. Lai, S. Utsunomiya, G. Roumpos, M. Fraser, H. Deng, T. Byrnes, P. Recher, N. Kumada, T. Fujisawa, and Y. Yamamoto, "GaAs microcavity exciton-polaritons in a trap", *physica status solidi (b)* **245** 1076 (2008)

[32] C. W. Lai, N. Y. Kim, S. Utsunomiya, G. Roumpos, H. Deng, M. D. Fraser, T. Byrnes, P. Recher, N. Kumada, T. Fujisawa and Y. Yamamoto, "Coherent zero-state and -state in an exciton?polariton condensate array", *Nature* **450** 529 (2007)

[33] G. Roumpos, Wolfgang H. Nitsche, Sven Hoefling, Alfred Forchel, Y. Yamamoto, "Gain-induced trapping of microcavity exciton polariton condensates", *Physical Review Letters* **104**, 126403 (2010)

[34] E. A. Cerda-Mendez, D. N. Krizhanovskii, M. Wouters, R. Bradley, K. Biermann, K. Guda, R. Hey, P. V. Santos, D. Sarkar, and M. S. Skolnick, "Polariton Condensation in Dynamic Acoustic Lattices" , *Physical Review Letters* **105**, 116402 (2010)

[35] O. E. Daif, A. Baas, T. Buillet, J. ?P. Brantut, R. I. Kaitouni, J. L. Staehli, F. MorierGenoud, and B. Deveaud, "Polariton quantum boxes in semiconductor microcavities", *Applied Physics Letters* **88**, 061105 (2006)

[36] R. Idrissi Kaitouni, O. El Daif, A. Baas, M. Richard, T. Paraiso, P. Lugan, T. Guillet, F. Morier-Genoud, J. D. Ganiere, J. L. Staehli, V. Savona, and B. Deveaud, "Engineering the spatial confinement of exciton polaritons in semiconductors", *Physical Review B* **74**, 155311 (2006)

[37] D. Bajoni, P. Senellart, E. Wertz, I. Sagnes, A. Miard, A. Lemaitre, and J. Bloch, "Polariton Laser Using Single Micropillar GaAs-GaAlAs Semiconductor Cavities", *Physical Review Letters* **100**, 047401 (2006)

[38] E. Wertz, L. Ferrier, D. D. Solnyshkov, R. Johne, D. Sanvitto, A. Lemaitre, I. Sagnes, R. Grousson, A. V. Kavokin, P. Senellart, G. Malpuech and J. Bloch, "Spontaneous formation and optical manipulation of extended polariton condensates", *Nature physics* **6**, 860 (2010)

[39] M. Wouters and I. Carusotto, "Excitations in a Nonequilibrium Bose-Einstein Condensate of Exciton Polaritons", *Physical Review Letters* **99**, 140402 (2007)

[40] M. G. Davis and R. F. O'Dowd, "A Transfer matrix Method Based Large-Signal Dynamic Model for Multielectrode DFB Laser", *IEEE Journal of Quantum Electronics* **30**, 2458 (1994)

[41] T. C. H. Liew, Yuri G. Rubo, and A. V. Kavokin ,"Generation and Dynamics of Vortex Lattices in Coherent Exciton-Polariton Fields", *Physical Review Letters* **101**, 187401 (2008)

[42] A. V. Gorbach, R. Hartley, and D. V. Skryabin ,"Vortex Lattices in Coherently Pumped Polariton Microcavities", *Physical Review Letters* **104**, 213903 (2010)

[43] W. Vincent Liu and Congjun Wu, "Atomic matter of nonzero-momentum Bose-Einstein condensation and orbital current order", *Physical Review A* **74**, 013607 (2006)

[44] L. Pitaevskii and S. Stringari, "Bose-Einstein Condensation", Clarendon Press Oxford (2003)

[45] S. Utsunomiya, L. Tian, G. Roumpos, C.W. Lai, N. Kumada, T. Fujisawa, M. Kuwata-Gonokami, A. Loefler, S. Hoeling, A. Forchel and Y. Yamamoto "Observation of Bogoliubov excitations in exciton-polariton condensates", *Nature Physics* **4**, 700- 705 (September, 2008)

[46] J. Keeling and N. G. Berloff, "Condensed-matter physics: Going with the flow", *Nature* **457**, 273 (2009)

[47] G. Wirth, M. Oelschlaeger, and A. Hemmerich, "Orbital superfluidity in the P-band of a bipartite optical square lattice", *Nature Physics*, doi:10.1038/nphys1857, Published online 12 December 2010

[48] T. Müller, S. Folling, A. Widera, and I. Bloch, "State Preparation and Dynamics of Ultracold Atoms in Higher Lattice Orbitals", *Physical Review Letters* **99**, 200405 (2007)

[49] Tristram J. Alexander, Anton S. Desyatnikov, and Yuri S. Kivshar, "Multivortex solitons in triangular photonic lattice", *Optics Letters* **32**, 1293 (2007)

[50] B. Terhalle, T. Richter, A. S. Desyatnikov, D. N. Neshev, W. Krolikowski, F. Kaiser, C. Denz, and Y. S. Kivshar, "Observation of Multivortex solitons in photonic lattices", *Physical Review Letters* **99**, 200405 (2007)

[51] A. S. Desyatnikov, N. Sagemerten, R. Fischer, B. Terhalle, D. Träger, D. N. Neshev, A. Dreischuh, C. Denz, W. Krolikowski, and Y. S. Kivshar, "Two-dimensional self trapped nonlinear photonic lattices", *Optics Express* **14**, 2851 (2007)

[52] H. Matsumura and T. Ando, "Effective-Mass Theory of Carbon Nanotube Junctions", *Journal of the Physical Society of Japan* **67**, 3542 (1998)

[53] T. Ando, "Theory of ElectronicStatesand Transport in Carbon Nanotubes", *Journal of the Physical Society of Japan* **74**, 777 (2005)

[54] C. Cohen-Tannoudji, J. Dupont-Roc, and G. Grynberg, "Photons and Atoms - Introduction to Quantum Electrodynamics",John Wiley & Sons (1989)

[55] A. V. Kavokin, J.J. Baumberg, G. Malpuech and F.P. Laussy, "Microcavities", Oxford University Press (2007)

[56] R. P. Feynman, R. B. Leighton and M. Sands, "The Feynman Lectures on Physics volume 3", Addison-Wesley (2nd edition, 2005)

[57] Y. Tokura and N. Nagaosa, "Orbital Physics in Transition-Metal Oxides", *Science* **288**, 462 (2000).

[58] C. Wu, D. Bergman, L. Balents, and S. Das Sarma, "Flat bands and Wigner crystallization in the honeycomb optical lattice", *Physical Review Letters* **99**, 70401 (2007).

Related Publications

International Conference Poster presentations

1. ”Exciton-Polariton Condensation in Triangular Lattice Potentials”, K. Kusudo, N. Y. Kim, M. Fraser, N.Masumoto, N. Kumada, S. Hoefling, Alfred Forchel and Yoshihisa Yamamoto, International Symposium on Quantum Nanophotonics and Nanoelectronics, Nov 18-20, 2009, Komaba Research Campus, the University of Tokyo, Tokyo, Japan.

2. ”Two energy-degenerate p-orbital condensates of Exciton-Polaritons in triangular lattice potentials”, K. Kusudo, N. Y. Kim, C. Wu, N. Kumada, S. Hoefling, Alfred Forchel and Yoshihisa Yamamoto, International Symposium on Physics of Quantum Technology, Apr 6-9, 2010, Hitotsubashi Memorial Hall, Tokyo, Japan.

3. (invited) ”The vortex-antivortex order in exciton-polariton condensation under triangular lattice potentials”, K. Kusudo, N. Y. Kim, C. Wu, A. Loffler, S. Hoefling, N. Kumada, L. Worschech, Alfred Forchel and Yoshihisa Yamamoto, Quantum Simulations Feb 28 - Mar 05, 2011, CENTRO DE CIENCIAS DE BENASQUE PEDRO PASCUAL, Benasque, Spain